Aus dem Institut für Zellbiochemie
(Prof Dr. rer. nat. P. Rehling)
[im Zentrum für molekulare Biowissenschaften]
der Medizinischen Fakultät der Universität Göttingen

Molecular Basis of Mitochondrial Diseases Exemplified by Mutation of the Translation Factor Cox14

INAUGURAL-DISSERTATION

zur Erlangung des Doktorgrades
der Medizinischen Fakultät der
Georg-August-Universität zu Göttingen

vorgelegt von

Steffen Witte

aus

Hannover

Göttingen 2022

Dekan:	Prof. Dr. med. W. Brück

Betreuungsausschuss

Betreuer*in:	Prof. Dr. rer. nat. P. Rehling
Ko-Betreuer*in:	Prof. Dr. med. D. Katschinski

Prüfungskommission

Referent*in:	Prof. Dr. rer. nat. P. Rehling
Ko-Referent*in:	Prof. Dr. med. D. Katschinski
Drittreferent*in:	Prof. Dr. U. Kornak

Datum der mündlichen Prüfung: 16.11.2023

Hiermit erkläre ich, die Dissertation mit dem Titel „Molecular Basis of Mitochondrial Diseases Exemplified by Mutation of the Translation Factor Cox14“ eigenständig angefertigt und keine anderen als die von mir angegebenen Quellen und Hilfsmittel verwendet zu haben.

Göttingen, den 23.11.23 ……

(Unterschrift)

Die Daten, auf denen die vorliegende Arbeit basiert, wurden teilweise publiziert:

Aich A, Boshnakovska A, **Witte S**, Gall T, Unthan-Fechner K, Yousefi R, Chowdhury A, Dahal D, Methi A, Kaufmann S, Silbern I, Lindovsky J, Nichtova Z, Zudova D, Koubkova G, Tröder S, Zevnik B, Riedel D, Michanski S, Möbius W, Ströbel P, Lüchtenborg C, Giavalisco P, Urlaub H, Fischer A, Brügger B, Jakobs S, Rehling P. Defective mitochondrial COX1 translation due to loss of COX14 function triggers ROS-induced inflammation in liver. *Nature Communications (Under Review)*

Witte S, Boshnakovska A, Özdemir M, Chowdhury A, Rehling P, Aich A. Defective COX1 expression in aging mice liver. *Biol Open*. 2023 Mar 15;12(3):bio059844.

Table of contents

Table of contents ..... **I**
List of Figures ..... **III**
List of Tables ..... **IV**
List of Abbreviations ..... **V**
1 Introduction **1**
1.1 The Mitochondrion – The Cellular Power Plant 1
1.2 The OXPHOS System 2
1.3 Structure and Assembly of Complex IV 4
1.4 The MITRAC Complex 4
1.5 Mitochondrial Diseases 6
1.6 Cox14 Dysfunction – a Complex IV Deficiency Syndrome 7
1.7 The Aims of this Work 8
2 Materials and Methods **9**
2.1 Materials 9
2.2 Methods 27
3 Results: Chapter One **42**
3.1 The Role of Cox14 in Cox1 Translation and MITRAC Complex Assembly 42
3.2 Effects of the Cox14 Mutation on the OXPHOS System 44
3.3 Phenotyping of COX14M19I 49
3.4 Triggers of the Inflammatory Response 58
3.5 Clinical Phenotype of COX14M19I 63
4 Results: Chapter Two **70**
4.1 Defective Cox1 Expression in Aging Mice Liver 70
5 Discussion **80**
5.1 The Role of Cox14 in Cox1 Translation and Complex IV Assembly 80
5.2 The Effects of Mutation in Cox14 on the OXPHOS System 80
5.3 Damage to Mitochondrial Membrane Structure in Hepatocytes 82
5.4 Antiviral Signaling 83
5.5 Lipid Metabolism 86
5.6 Mitochondrial Dysfunction - A Driver of Human Diseases? 88
6 Conclusion **90**
7 Appendix **92**
7.1 Effects of the Cox14 Mutation on OXPHOS Protein Complexes 92
7.2 The Inflammatory Pathway in COX14M19I 95

7.3 Lipid Metabolism 100
7.4 Phenotype of COX14M19I 100
8 Bibliography 103
Acknowledgements 114
Curriculum vitae 115

List of Figures

Figure 1.1: The structure of mitochondria. 2
Figure 1.2: The OXPHOS System. 3
Figure 1.3: The MITRAC Complex. 5
Figure 3.1: Cox14 Mutation Causes a Decrease in Cox1 Levels and MITRAC Complex Assembly. 43
Figure 3.2: OXPHOS Complexes and Protein Levels showed tissue-dependent differences. 45
Figure 3.3: OXPHOS system, Complex I and Complex IV activity varied in different tissues. 49
Figure 3.4: EM Analysis showed disrupted and discontinuous mitochondrial membranes in hepatocytes. 51
Figure 3.5: Transcriptome analysis revealed upregulation of interferon mediated antiviral immune response pathways. 52
Figure 3.6: Antiviral Signaling in COX14M19I. 55
Figure 3.7: Inflammatory Response in Liver. 57
Figure 3.8: Enriched Extramitochondrial Nucleic Acids in COX14M19I Liver. 60
Figure 3.9: Cytosolic DNA and RNA Sensors Expression in COX14M19I. 62
Figure 3.10: Elevated Cholesterol Levels Indicated Increased Cholesterol Metabolism in COX14M19I. 64
Figure 3.11: COX14M19I developed hepatic steatosis and inflammatory characteristics. 66
Figure 3.12: COX14M19I Phenotype. 68
Figure 3.13: Aged mitochondria show a decrease in membrane potential and increased oxidative stress. 71
Figure 3.14: Mitochondrial metabolism changes with age. 73
Figure 3.15: OXPHOS Complex IV decreases with age. 75
Figure 3.16: OXPHOS Complex IV decreases with age. 77
Figure 3.17: OXPHOS complex IV decreases with age 78
Figure 4.1: Intracellular Interferon Type I signaling. 85
Figure A.1: Cox1 Translation and Mitrac Complex assembly. 92
Figure A.2: OXPHOS Protein levels 93
Figure A.3: OXPHOS Complex Levels. 94
Figure A.4: Apoptotic proteins did not show significant changes in the liver. 95
Figure A.5: Transcriptome Analysis. 97
Figure A.6: ISGF3 Complex Activation. 97
Figure A.7: Inflammatory Cytokines. 98
Figure A.8: Inflammatory Response in Liver. 99
Figure A.9: Extramitochondrial mtDNA Levels. 99
Figure A.10: Fat Metabolism. 100
Figure A.11: Pulmonary function diagnostics showed indications of a restrictive pulmonary disease in COX14M19I. 102

List of Tables

Table 2.1: List of Chemicals....9
Table 2.2: Buffers....14
Table 2.3: Instruments....18
Table 2.4: Kits and Disposables....19
Table 2.5: Primary Antibodies....20
Table 2.6: Secondary Antibodies....22
Table 2.7: Primers and Primerpairs....22
Table 2.8: Software....26
Table A.1: Immunophenotype....100

List of Abbreviations

ADP	adenosine diphosphate
AMP	adenosine monophosphate
APS	ammonium persulfate
ATP	adenosine triphosphate
BCL	B-cell lymphoma
BME	beta mercaptoethanol
BN	blue native
BSA	bovine serum albumine
c	cyclic
cGas	cyclic GMP-AMP synthase
Cl	chloride
Coa3	cytochrome C oxidase assembly factor 3
COX	cytochrome C oxidase
Cox14	cytochrome C oxidase assembly factor 14
Cys	cysteine
DAMP	damage-associated molecular pattern
DDM	4,4'-diaminodiphenylmethan
DNA	desoxyribonucleic acid
dsRNA	double stranded RNA
DTT	dithiothreitol
ECG	electrocardiogram
ECL	enhanced chemiluminescence
EDTA	ethylenediaminetetraacetate
EEG	electroencephalography
EGTA	ethylenglycoltetraacetic acid
EM	electron microscopy
FACS	fluorescence-activated cell sorting
$FADH_2$	flavin adenine dinucleotide hydrogen
FCCP	carbonyl cyanide-4 (trifluoromethoxy)phenylhydrazone
FITC	fluorescein isothiocyanate

GAPDH	glycerinaldehyde-3-phosphate dehydrogenase
GMP	guanosine monophosphate
GTP	guanosine triphosphate
H	hydrogene
HEPES	4-(2-hydroxyethyl)-1-piperazineethanesulfonic acid
IFI	interferon-induced protein
IgG	immunoglobulin G
IMM	inner mitochondrial membrane
IMS	inter membrane space
IRF	interferon regulatory factor
ISG	interferon-stimulated gene
KCN	potassium cyanide
kDA	kilodalton
Mito/mt	mitochondrial
MITRAC	mitochondrial translation regulation assembly intermediate of cytochrome c oxidase complex
MOPS	3-(N-morpholino)propanesulfonic acid
mRNA	messenger RNA
NADH	nicotinamide adenine dinucleotide
NK-cell	natural killer cell
NKT-cell	natural killer T cell
OCR	oxygen consumption rate
OMM	outer mitochondrial membrane
OXA	oxidase assembly protein
Page	polyacrylamide gel electrophoresis
PBS	phosphate-buffered saline
PK	proteinase K
PMSF	phenylmethylsulfonyl fluoride
PRR	pattern recognition receptor
PVDF	polyvinylidene fluoride
RNA	ribonucleic acid
ROS	reactive oxygen species
Rpm	revolutions per minute
RSC	respiratory super complex
S	sulfur

SDHA	succinate dehydrogenase A
SDS	sodium dodecyl sulfate
SEM	standard error of the mean
SLE	systemic lupus erythematosus
Smim	small integral membrane protein
STAT	signal transducer and activator of transcrption
TBS	tris-buffered saline
TEMED	N,N,N',N'-tetramethylethane-1,2-diamine
TIM	presequence translocase of the inner membrane
TOM	translocase of the outer membrane
Tris	tris(hydroxymethyl)aminomethane
USP	ubiquitin specific peptidase
UV	ultraviolet
WT	wild-type

1 Introduction

1.1 The Mitochondrion – The Cellular Power Plant

Many cellular pathways localize to mitochondria. Among others, mitochondria play a key role in energy metabolism by regenerating ATP utilizing the oxidative phosphorylation (OXPHOS) system (Lill et al. 2012; Friedman and Nunnari 2014). Therefore, the mitochondrion is often referred to as „the powerhouse of the cell ".

Due to its endosymbiotic origin, mitochondria represent a genetically semiautonomous organelle of the cell, containing own genetic material and a dedicated replication system. Mitochondria are circumscribed by a double membrane (de Duve 2007). They are separated from the cytosol by the outer membrane (OMM), which incorporates pore forming proteins for metabolite transport. The inner membrane of mitochondria (IMM) forms cristae, that house the five protein complexes of the OXPHOS system along with a multitude of other proteins (Vogel et al. 2006).

Since a large fraction of the mitochondrial genome has been transferred to the nucleus, today the circular mitochondrial DNA of human cells code for only 13 proteins, 2 rRNAs and 22 tRNAs (Gray 1999; Taanman 1999). The mitochondrial genome is equipped with a minimal coding capacity and 99% of mitochondrial proteome is imported by dedicated translocation machineries. Also, the majority of the structural subunits of the OXPHOS complexes are nuclear-encoded and imported from the cytosol.

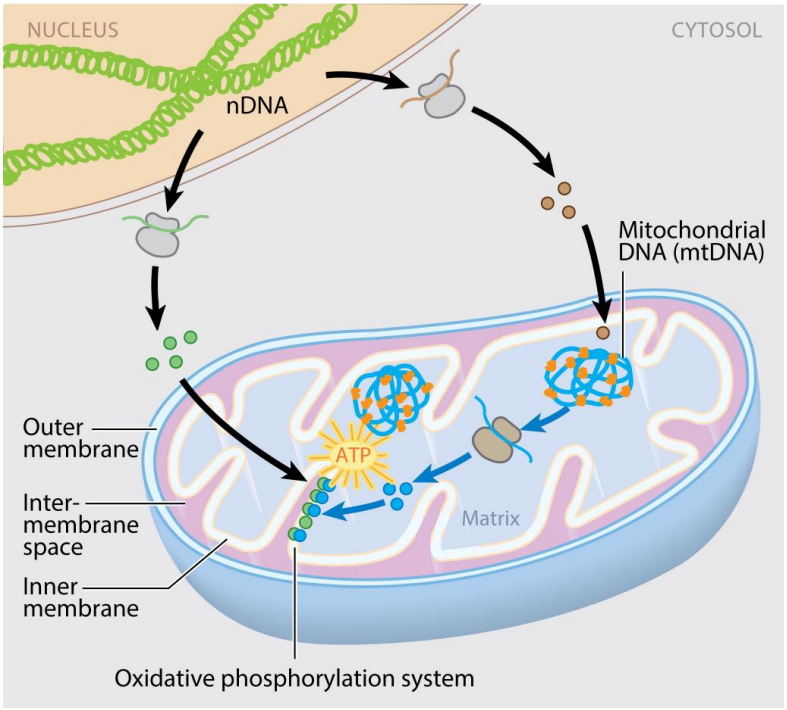

Figure 1.1: The structure of mitochondria.

Mitochondria are genetically semiautonomous organelles, containing own genetic material and are delimited by a double membrane from the cytosol. Proteins of the OXPHOS system are located in the cristae to regenerate ATP. From (Gustafsson et al. 2016). Courtesy of Annual reviews, Order License ID1255724-1, ISSN 1545-4509.

After import across the OMM, nuclear-encoded subunits associate with mitochondrial translation products forming the enzyme complexes (Fernandez-Vizarra et al. 2009; Soto et al. 2012; Dennerlein and Rehling 2015).

All 13 mitochondrial encoded proteins are core subunits of the OXHPOS complexes (Chacinska et al. 2009; Ott and Herrmann 2010; Hällberg and Larsson 2014). Mitochondrial encoded proteins are translated by membrane-bound ribosomes and inserted co-translationally into the IMM by the nuclear encoded membrane insertase OXA1L (Hell et al. 2001; Ott and Herrmann 2010; Thompson et al. 2018).

1.2 The OXPHOS System

Mitochondria are key players in regenerating the central energy carrier ATP. Regeneration of ATP is facilitated by the five protein complexes of the OXPHOS system.

Electrons, derived from NADH or $FADH_2$, are fed into the OXPHOS system via Complex I (NADH dehydrogenase) or Complex II (succinate dehydrogenase) respectively and then transported along the four complexes. Complex III (cytochrome C reductase) passes electrons on Complex IV (cytochrome c oxidase), which catalyzes the transfer of electrons to molecular oxygen.

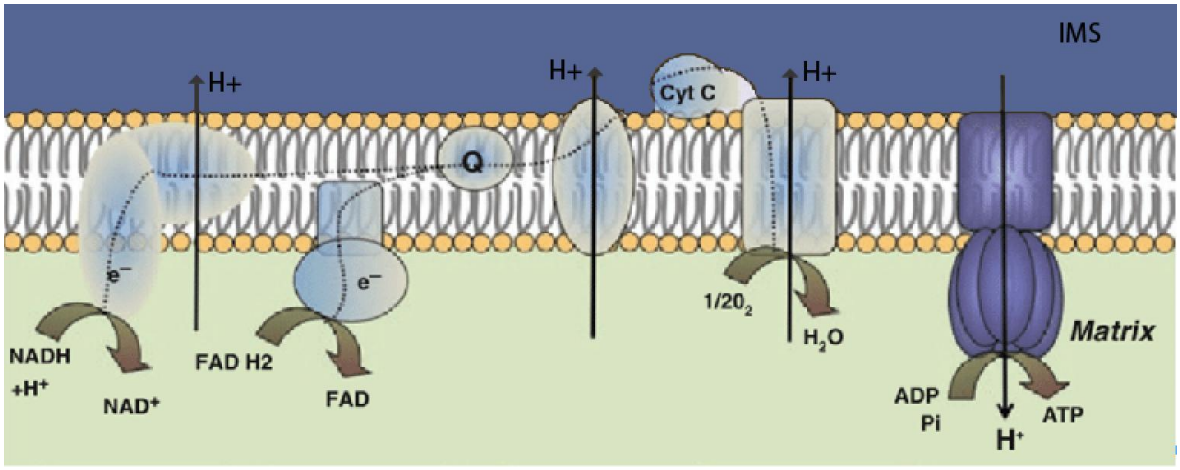

Figure 1.2: The OXPHOS System.

Electrons, generated from reduction of NADH and $FADH_2$, are fed into Complex I and Complex II. They are passed amongst the Complexes to finally reduce oxygen, catalyzed by Complex IV. The redox energy is converted to build a membrane potential, translocating protons into the intermembrane space. Complex V regenerates ATP utilizing the back flux of proteins into the matrix. Based on Benard et al, 2011 – Mitochondrial Dynamics and Neurodegeneration (pp. 47-68) and (Larsson 2010). Courtesy of Annual reviews, Order License ID 1255750-1, ISSN 1545-4509.

This concatenation of redox reactions catalyzed by complexes I, II, III, and IV is referred to as the electron transport chain or respiratory chain (Fernandez-Vizarra et al. 2009; Winge 2012). The energy of the redox reactions is converted to build a membrane potential by translocating protons from the matrix across the complexes into the intermembrane space.

The membrane potential is utilized by Complex V (ATP synthase) to regenerate ATP, driven by the back flux of protons into the matrix (Ballmoos et al. 2008).

Components of the respiratory chain have been found to form super complexes to maximize the efficiency of the OXPHOS system by optimizing electron flux through substrate channeling, thereby stabilizing the Complexes and reducing ROS production (Schägger and Pfeiffer 2000; Winge 2012; Guo et al. 2018).

1.3 Structure and Assembly of Complex IV

Complex IV (COX, also referred to as cytochrome c oxidase) forms the terminal protein complex of the respiratory chain. Since all electrons pass through Complex IV, it represents a central factor necessary for the development of a membrane potential and regeneration of ATP by the OXPHOS system (Fernandez-Vizarra et al. 2009; Guo et al. 2018; Zong et al. 2018).

14 different protein subunits of dual genetic origin have to assemble to form the final complex. Only the three core proteins in the center of the complex (Cox1, Cox2 and Cox3) are encoded and translated in the mitochondria (Soto et al. 2012). In Complex IV maturation, each of the three mitochondrial core proteins Cox1, Cox2 and Cox3 forms one independent assembly intermediate (Vidoni et al. 2017). Only after the three assembly intermediates are saturated with their cytosolic components, the subunits finally engage to form the mature Complex IV.

Since the majority of subunits are nuclear-encoded and translated in the cytosol, a plethora of factors are required to coordinate the assembly and translation of all 14 subunits into a functioning Complex IV (Timón-Gómez et al. 2018).

1.4 The MITRAC Complex

In contrast to yeast, human mitochondrial mRNAs lack significant 5'UTR regions and therefore, Cox1 translation is primarily co- and post-translationally regulated (Temperley et al. 2010; Mick et al. 2012; Szklarczyk et al. 2012; Weraarpachai et al. 2012a; Clemente et al. 2013).

Cox1 translation and its insertion into the IMM constitutes the beginning of the assembly process. Because Cox1 acts as a cornerstone for the assembly of other subunits, this marks a critical step in the early formation of Complex IV. Since this process also involves addition of cofactors heme and copper, it is coordinated and regulated by a variety of assembly factors (Mick et al. 2012; Weraarpachai et al. 2012a; Clemente et al. 2013; Dennerlein et al. 2015; Ostergaard et al. 2015).

The newly synthesized Cox1 is bound by Cox14, which is the mouse orthologue of human C12orf62. Together with several other factors, they form the core components of the MITRAC complex (mitochondrial translation regulation assembly intermediate of cytochrome c oxidase).

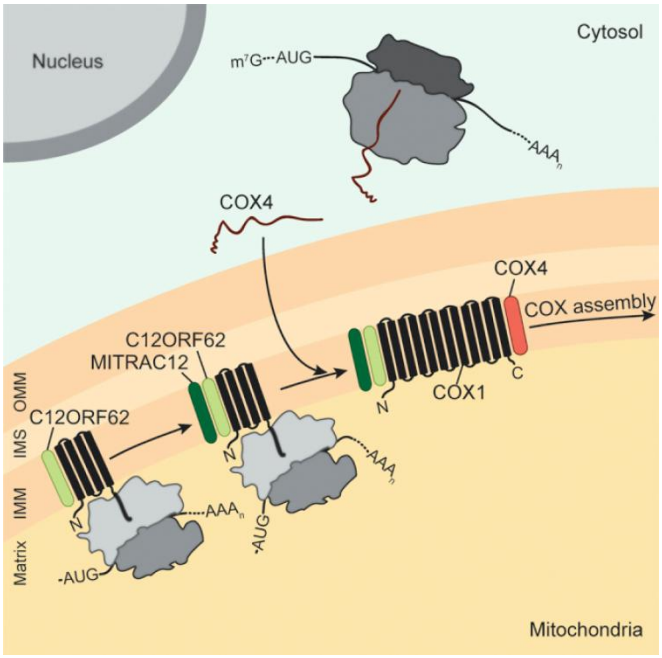

Figure 1.3: The MITRAC Complex.

Newly translated Cox1 is bound by Cox14 (human C12orf62) and inserted into the IMM. Associating with Coa3 (human MITRAC12) the MITRAC Complex begins to form in early assembly intermediate of Complex IV. From Richter-Dennerlein et al. 2016. With greatest thanks to Sven Dennerlein, Ricarda Richter-Dennerlein and Cell Press/Elsevier for providing the illustration.

Cytosolic components are transported by the translocase of the outer membrane (TOM) into the IM, where they assemble into the MITRAC complex, coordinated by TIM21. TIM21 acts as a „transport shuttle“ for the imported proteins between the translocase of the inner membrane (Tim) and the Cox1 protein (Mick et al. 2012).

During the assembly process, the protein composition of the MITRAC Complex undergoes constant changes, depending on the maturation state of Cox1 (Richter-Dennerlein et al. 2016). While the above-mentioned factor Cox14 associates with Coa3 as early components of the MITRAC complex, the small integral membrane protein 20 (Smim20, human MITRAC7) acts at a late stage in the assembly process. It interacts with Coa3 in the IMM after Cox4-1, a

nuclear-encoded subunit of Complex IV, is introduced in the MITRAC complex (Dennerlein et al. 2015).

1.5 Mitochondrial Diseases

Mitochondrial diseases can be distinguished between primary and secondary mitochondrial diseases. Primary mitochondrial diseases are defined by mutations that directly affect the OXPHOS system.

The prevalence of primary mitochondrial diseases is about 9.2 of 100000 (Schaefer et al. 2008). They show a wide spectrum of symptoms (for example myopathies, neuromuscular dysfunction, growth and developmental disorders, as well as cardiac, renal, and hepatic failure) and can affect almost any organ. Often, primary mitochondrial diseases result in a severe phenotype causing high childhood mortality and developmental disorders (Robinson 2000; Shoubridge 2001; Nunnari and Suomalainen 2012).

Mostly, the mutations are inherited autosomal recessively, however mutations of the mtDNA have a maternal inheritance (Vu et al. 2002).

A number of mechanisms are found to maintain the quality of mitochondria. In addition, mitochondria are highly dynamic organelles, which can adapt to changing metabolic conditions (Eisner et al. 2018). Malfunctioning mitochondria, for example those with mutations in the mitochondrial genome, are eliminated, thus sustaining organelle homeostasis (Ng et al. 2021).

Dysfunctions in quality control or adaptation mechanisms of mitochondria could cause the accumulation of malfunctioning organelles and mutations in the mitochondrial genome. This appears to ultimately promote the development of several common diseases. For example, Diabetes, cancer, cardiovascular-, autoimmune- and neurodegenerative diseases are associated with mitochondrial pathologies (Yoon et al. 2011; Boland et al. 2013; Ong et al. 2013).

However, since mitochondrial dysfunction is one of many factors in the multifactorial pathogenesis of these common diseases, they are also called mitochondrial associated- or secondary mitochondrial diseases (Niyazov et al. 2016).

1.6 Cox14 Dysfunction – a Complex IV Deficiency Syndrome

As reported in previous publications, C12orf62 plays a key role in Complex IV assembly, bridging the translation processes to maturation of Cox1 in the IMM by assembly of the MITRAC complex (Richter-Dennerlein et al. 2016). A loss of C12orf62 results in lower translation of Cox1 and an isolated Complex IV deficiency (Weraarpachai et al. 2012a).

The dysfunction of C12orf62 is associated with the phenotype of a fatal neonatal lactic acidosis, resulting in death of the newborn within 24h after birth. Pathologies affected multiple organs, such as brain, liver, heart and kidneys. This makes the loss of functional C12orf62 a textbook example for a primary mitochondrial disease, defined by mutations directly affecting function of the OXPHOS system (Weraarpachai et al. 2012b).

1.7 The Aims of this Work

Mitochondrial diseases have severe clinical consequences with very limited therapeutic options. In addition, mitochondrial dysfunction has been observed to occur in association with many common diseases and was often attributed to the aging process. However, the actual impact of mitochondrial dysfunction on the diseases themselves is under current debate and requires further investigation.

This work aims to investigate the molecular mechanisms underlying mitochondrial disorders by placing the biochemical pathomechanisms in a clinical context. To this end, a COX14M19I mouse line with a homozygous point mutation in *Cox14* was generated (Aich et al., unpublished). The role of Cox14 in Cox1 translation and Complex IV assembly in a tissue context should be examined to extend previous results of analyses of the factor C12orf62 in human cells (Weraarpachai et al. 2012b). Complex stability, translation, and protein association assays should assess the effects of the Cox14 mutation on Cox1 translation and MITRAC assembly. An important aspect of mitochondrial disorders is why genetic defects show different phenotypes in different tissues. Therefore, differences and similarities in heart, liver, muscle and brain should be compared. Thus, the resulting phenotype and tissue-specific responses were to be analyzed in detail to bridge the biochemical analysis and clinical consequences of mitochondrial dysfunction.

In a second section, this study will also address mitochondrial changes during aging. A transcriptome analysis of the mitochondrial genome of young and aged mouse liver samples should be used to investigate genetic adaptation processes of aging. The results should be backed up by measurement of OXPHOS protein levels. In addition, mitochondrial functional parameters such as membrane potential and ROS levels should assess the physiology of aged mitochondria.

The goal of this study was to provide new insights into the facets and effects of mitochondrial dysfunction, which could lead to new treatment perspectives for major common diseases.

2 Materials and Methods

2.1 Materials

2.1.1 Chemicals

The following chemicals (Table 2.1) were used in analytical grade purity for the execution of the experiments.

Table 2.1: List of Chemicals

Chemical	**Producer**
2-Keto glutarate	Sigma-Aldrich
^{35}S-L-methionine	Hartmann Analytic
4-Nitro blue tetrazolium chloride	Roth
6-Aminocaproic acid	Sigma-Aldrich
Acetic acid	Roth
Acetone	Roth
Acetyl Co-A	Sigma-Aldrich
Acrylamide (Bis)	Roth
ADP	Sigma-Aldrich
Agarose	Roth
Alanine	NovaBiochem
Ammonium persulfate	Roth
Ammoniumperoxodissulfate (APS)	Roth
Ampicillin	AppliChem
Antimycin	Sigma-Aldrich
Arginine	NovaBiochem
Ascorbate	Roth

Asparagine	NovaBiochem
Aspartate	NovaBiochem
ATP	Roche
Beta mercaptoethanol (BME)	Sigma-Aldrich
Bio-Rad protein assay	Bio-Rad
Bis-Acrylamide	Roth
Bis-Tris	AppliChem
Bovine serum albumin (BSA)	Sigma-Aldrich
Bromophenol blue	Merck
Carbonyl cyanide-4 (trifluoromethoxy)phenylhydrazone (FCCP)	Sigma-Aldrich
Cardiolipin	Avanti
Chloroform	Roth
Coomassie brilliant blue G-250	Roth
Coomassie brilliant blue R-250	Roth
Copper(II)sulfate pentahydrate	Merck
Creatine kinase	Roche
Creatine phosphate	Roche
Cyclohexamide	Sigma-Aldrich
Cysteine	NovaBiochem
Cytochrome C	Calbiochem
4,4'-Diaminodiphenylmethan (DDM)	Calbiochem
Digitonin	Calbiochem
Dipotassium phosphate	Roth
Disodium phosphate	Roth
Dimethylphthalat (DMP)	Sigma-Aldrich

DMSO (dimethylsulfoxide)	Applichem
DSG (disuccinimidyl glutarate)	Thermo Scientific
DSS (disuccinimidyl suberate)	Thermo Scientific
DTNB (5,5'-dithiobis-(2-nitrobenzoic acid))	Merck
DTT (Dithiothreitol)	Roth
EDTA (Ethylenediaminetetraacetic acid)	Roth
EGTA (Ethylene Glycol Tetraacetic Acid)	Roth
Emetine	Abcam
Ethanol 100%	Roth
Ethidium bromide (0.025%)	Roth
Galactose, D(+)	Roth
Glucose, D(+)	Roth
Glutamate	NovaBiochem
Glutamine	NovaBiochem
Glycerol	Sigma-Aldrich
Glycine	Roth
GTP	Sigma-Aldrich
Guanidine hydrochloride	Thermo Scientific
HEPES	Roth
Histidine	NovaBiochem
Hydrochloric acid (37%)	Roth
Hydrogen peroxide	Sigma-Aldrich
Imidazole	Sigma-Aldrich
IPTG (Isopropyl β- d-1-thiogalactopyranoside)	Sigma-Aldrich
Isoflurane	Abbvie

Isoleucine	NovaBiochem
Isopropanol	Roth
L-Glutathione reduced	Sigma Aldrich
Leucine	NovaBiochem
Luminol	Thermo Scientific
Lysine	NovaBiochem
Magnesium acetate	Merck
Magnesium chloride	Merck
Magnesium sulfate	Applichem
Malate	Roth
Mannitol	Roth
Methanol	Roth
Methionine	NovaBiochem
Milk powder	Frema, Heirler Cevonis GmbH
MOPS	Roth
NADH	Roche
NP-40	Thermo Scientific
Oligomycin	Sigma-Aldrich
Opti-Mem	Life Technologies
OrangeG	Sigma-Aldrich
Oxaloacetic acid	Sigma-Aldrich
PBS (Phosphate-buffered saline)	Lonza
Penicillin streptomycin	Life Technologies
Phenol	Roth
Phenylalanine	NovaBiochem
PMSF	Roth

Potassium chloride	Roth
Potassium cyanide (KCN)	Sigma-Aldrich
Potassium hydrogen phosphate	Merck
Potassium phosphate	Roth
Proline	NovaBiochem
Protease inhibitor mix	Roche
Protein-A sepharose	GE-Healthcare
Proteinase K	Roche
Pyruvate	Roth
RNAse A	Thermo Scientific
Rotenone	Sigma-Aldrich
Roti-Quant® reagent	Roth
SDS (sodium dodecyl sulfate)	Serva
SDS marker	Biorad
Serine	NovaBiochem
Sodium azide	Merck
Sodium borate	Sigma-Aldrich
Sodium chloride	Roth
Sodium hydroxide	AppliChem
Sodium pyruvate	Sigma-Aldrich
Sodium succinate	Sigma-Aldrich
Sorbitol	Roth
Succinate	Sigma-Aldrich
Sucrose	Roth
Tetramethylethylendamine (TEMED)	Roth
Threonine	NovaBiochem

Tissue protein extraction reagent (T-PER)	Thermo Scientific
TMPD (tetramethyl-p-phenylenediamine)	Sigma-Aldrich
Tricine	Roth
Tris (Tris(hydroxymethyl)aminomethane)	Roth
Triton X-100	Merck
Trizol	Ambion
Tryptophan	NovaBiochem
Tween-20	Roth
Tyrosine	NovaBiochem
Valine	NovaBiochem
William's E medium	Thermo Scientific
Xylene cyanol	Sigma-Aldrich

2.1.2 Buffers

All buffers, which were diluted in autoclaved, deionized water, are listed in Table 2.2 (in a 1x concentration).

Table 2.2: Buffers

Buffer	**Composition**
DNA loading dye	5% Glycerol, 0.025% Bromophenol blue, 0.025% Xylene cyanol, 2.5 mM EDTA
Blotting buffer	150 mM Glycine, 20 mM Tris, 0.02% SDS, 20% methanol
BN anode buffer	50 mM Bis Tris/HCl (pH 7.0)
BN cathode buffer (optionally with Coomassie)	50 mM Tricin, 15 mM Bis-Tris (pH 7.0) (with 0.02% Coomassie brilliant blue G-250)
BN gel buffer	66.67 mM 6-Aminocapronacid, 50 mM

	Bis-Tris/HCl (pH 7.0)
BN sample buffer	0.5% Coomassie brilliant blue G-250, 50 mM 6-aminocaproic acid, 10 mM Bis-Tris (pH 7.0)
BN solubilization buffer	20% Digitonin or 20 %/36 % DDM, 0.1 mM EDTA, 20 mM Tris/HCl (pH 7.4), 50 mM NaCl, 10 % glycerol
Buffer AL (mtDNA Isolation)	5 mM $CaCl_2$, 2% SDS, 4 M GuHCl
Coomassie destaining solution	40% Ethanol, 10% acetic acid
Coomassie staining solution	2.5 g/L Coomassie brilliant blue R-250, 40% ethanol, 10% acetic acid
Digestion buffer heart/muscle	0.05% Trypsin, 1 M PBS, 10 mM EDTA
In vivo translation amino acid mix	All amino acids (except Methionine) in 1 M concentration
Isolation buffer 1 and 2 liver	10 mM Tris-MOPS, 1 mM EGTA/Tris, 200 mM sucrose
Isolation buffer 1 brain	20 mM HEPES (pH 7.6), 220 mM mannitol, 1 mM EDTA, 70 mM mannitol
Isolation buffer 1 heart/muscle	67 mM sucrose, 50 mM Tris/HCl (pH 7.4), 50 mM KCl, 1 mM EDTA, 0.2% BSA
Isolation buffer 2 brain	0.1% BSA, 20 mM HEPES (pH 7.6), 220 mM mannitol, 1 mM EDTA, 70 mM mannitol
Isolation buffer 2 heart/muscle	0.2 M Sucrose, 3 mM EGTA/Tris, 10 mM Tris/HCl (pH 7.4)
Lysis buffer	T-PER Protein reagant, 1x Proteasis inhibitor cocktail, 1x PhosSTOP
MAS buffer (Seahorse)	70 mM sucrose, 210 mM mannitol, 5 mM HEPES, 1 mM EGTA, 0.5% fatty acid free BSA, 10 mM KH_2PO_4, 5 mM $MgCl_2$

PBS (phosphate-buffered saline)	137 mM NaCl, 2.7 mM KCl, 10 mM Na_2HPO_4, 1.8 mM KH_2PO_4
Perfusion solution	1.42 M NaCl, 67 mM KCl, 100 mM HEPES
Pyruvate mix (Seahorse)	0.1 M Pyruvate, 40 mM malate, 40 mM ADP
Resolving gel (BN Page)	4-10% Acrylamide/Bisacrylamide (49,5%/3%), 1x BN Gel buffer, 2-30% glycerol
Resolving gel (Göhrlich SDS-PAGE)	12%/16% Acrylamide, 0.75 M Tris/HCl (pH 8.8), 0.1 M sucrose, 0.01% SDS, 2.5% glycerol
Resolving gel Tricine-SDS-Page	1x Tris-Tricine gelbuffer, 10-18% Acrylamide/Bisacrylamide (49.5%/3%), 0-13% glycerol
SDS Running buffer	25 mM Tris, 192 mM glycine, 0.1% SDS
SDS Sample buffer	2% SDS, 10% Glycerol, 0.01% bromphenolblue, 60 mM Tris/HCl pH 6.8, 1% Beta mercaptoethanol (BME)
SEM Buffer	250 mM sucrose, 1 mM EDTA, 10 mM EDTA (pH 7.2)
Solubization buffer (Immunoprecipitation)	50 mM Tris/HCl, 50 mM NaCl, 10% glycerol, 5 mM EGTA, 1 % digitonin, 200 µM PMSF
Stacking gel (BN-PAGE)	2% Acrylamide/Bisacrylamide (49.5%/3%), 1x BN gel buffer
Stacking gel (Tris-Tricine-SDS-PAGE)	1x Tris-Tricine-Gelbuffer, 4% Acrylamide/Bisacrylamide (49.5%/ 3%)
Stacking gel (Göhrlich SDS-PAGE)	4% acrylamide, 0.01M Tris/HCL (pH 6.8), 0.1% SDS

Stripping buffer	6 M guanidine hydrochloride, 0.2% NP-40, 20 mM Tris-HCl (pH 7.4), 1.5% DTT
Succinate mix (Seahorse)	0.2 M succinate, 40 mM ADP
TAE buffer	40 mM Tris/acetate (pH 8.0), 2 mM EDTA
TBS-T	20 mM Tris/HCl (pH 7.5), 125 mM NaCl, 0.1% Tween-20
TBS (Tris buffered Saline)	20 mM Tris/HCl (pH 7.5), 125 mM NaCl
Translation buffer (in vivo translation)	25 mM sucrose, 100 mM mannitol, 80 mM KCl, 5 mM $MgCl_2$, 1 mM Kpi (pH7.4), 25 mM HEPES-KOH (pH 7.4), 6 mM ATP in H_2O (pH 7.2) KOH, 0.75 mM GTP I H_2O (pH 7.2) KOH, 12 mM creatine phosphate, 10 mM Na-succinate, 0.625 mg/ml creatine kinase, 9 mM 2-ketoglutarate, 0.15 mM amino acid mix, 100 ug/ml emetine, 100 µg/ml cyclohexamide, 2.5 mM malate, 1 mg/ml BSA, 1x PI
Tris-Tricine gel buffer	1 M Tris, 0.1% SDS (pH 8.45)
Tris-Tricine anode buffer	0.2 M Tris (pH 8.9)
Tris-Tricine cathode buffer	0.1 M Tris, 0.1 M Tricine, 0.1% SDS (pH 8.25)
Washing buffer (immunoprecipitation)	50 mM Tris/HCl, 50 mM NaCl, 10% glycerol, 5 mM EGTA, 0.3% digitonin, 200 µM PMSF

2.1.3 Instruments

All instruments used are listed in Table 2.3.

Table 2.3: Instruments

Instrument	**Supplier**
15 ml Potter S (Dounce homogenizer)	Sartorius
5415 R (centrifuge)	Eppendorf
5417 R (centrifuge)	Eppendorf
5424 (centrifuge)	Eppendorf
5804 R (centrifuge)	Eppendorf
Cary 50 Bio UV-Visible Spectrophotometer	Varian
Dounce homogenizer (glass-glass, BBI-8540705)	Sartorius
EPS 601 power supply	GE Healthcare
Flow Cytometer FACS CantoTM II BD	Biosciences
Gel Casting apparatus for Agarose Gels	Bio Rad
Image Quant 800	Amersham
iMark Microplate Reader	Bio Rad
Labcycler	Sensquest
Mini BN Page Combs	BioRad
Mini BN Page Plates	BioRad
Nanodrop ONE	Thermo Scientific
Power supply 1	BioRad
Semi Dry Blotting Chamber	PEQLAB Biotechnologie
Storage Phosphor screen	GE Healthcare
Stratagene Mx3000P	Agilene Technologies
Synergy Microplate Reader	BioTek

Terflon douce homogenizer	Schuett Biotec
Thermomixer	Eppendorf
Typhoon FLA 9500 Phosphoimager	GE Healthcare
Vaccubrand® 2C Gel pump	Scie-Plas
VortexGenie2	Scientific Industries
XFe96 Extracellular Flux Analyzer	Agilent

2.1.4 Kits

The following kits (Table 2.4) were used according to manufacturer's specifications.

Table 2.4: Kits and Disposables

Product	**Producer**
1.5 ml and 2 ml Reaction tube	Sarstedt
384 PCR Plate	Thermo Scientific
96 Well Platte	Sigma
Anti-Mitochondrial Antibody (AMA) Assay	Euroimmun
Antinuclear Antibody (ANA) Assay	Aesku Diagnostics
Blotting Papier	Heinemann Labortechnik
Cannula	Braun
Complex I Enzyme Activity Microplate Assay Kit (Colorimetric)	abcam
Complex II Enzyme Activity Microplate Assay Kit (Colorimetric)	abcam
Complex IV Rodent Enzyme Activity Microplate Assay Kit (Colorimetric)	abcam
DNase I, RNase free Kit	Thermo Scientific

EDTA Blood Tubes	Sarstedt
Filter Tips	Sarstedt
First strand cDNA Synthesis Kit	Thermo Scientific
GeneRuler DNA Ladder Mix	Thermo Scientific
Interferon LEGENDplex™ Assay	Biolegend
Pipette Tips 10 µl, 100 µl, 1 ml	Sarstedt
Precision Plus Protein Standard All Blue	BioRad
PVDF membrane (Immobilon-P)	Merck
QIAamp DNA Blood Mini Kit	Qiagen
RNA Clean and Concentrator Kit	Zymo Research
Seahorse XF Cell Mito Stress Test Kit	Agilent
Sensimix SYBR Lo-ROX Kit	Bioline
X-ray films	Foma Bohemia (Hradec Kralove, Czech Republic)

2.1.5 Antibodies and Primers

For the immunodetection of the proteins, monoclonal/polyclonal primary antibodies, raised in rabbits and mice, were used in a concentration of 1:250, 1:500, 1:1000, 1:2000 and 1:5000 (Table 2.5). The secondary antibodies used in 1:1000, 1:2000 and 1:5000 concentration, coupled to horseradish peroxidase, were raised in goat against rabbit or mouse immunoglobulin (Table 2.6).

Table 2.5: Primary Antibodies

Antibody	**Supplier**
Mouse polyclonal Anti-CASP3	Cell Signaling Technology
Mouse polyclonal Anti-CASP9	Cell Signaling Technology
Mouse polyclonal Anti-SDHA	Home-made
Mouse polyclonal Anti-ZBP1	Cell Signaling Technology

Mouse polyclonal Anti-ISG15	Cell Signaling Technology
Mouse polyclonal Anti-STAT2	Cell Signaling Technology
Mouse polyclonal Anti-LSDP5	Cell Signaling Technology
Mouse polyclonal Anti-MFN1	Cell Signaling Technology
Mouse polyclonal Anti-NRF1	Cell Signaling Technology
Mouse polyclonal Anti-DRP1	Cell Signaling Technology
Mouse polyclonal Anti-IRF7	Cell Signaling Technology
Mouse polyclonal Anti-PGC1a	Cell Signaling Technology
Rabbit polyclonal Anti-ATP5B	Home-made
Rabbit polyclonal Anti-BAX	Cell Signaling Technology
Rabbit polyclonal Anti-COX1	Home-made
Rabbit polyclonal Anti-COX14	Home-made
Rabbit polyclonal Anti-COX2	Home-made
Rabbit polyclonal Anti-COX4I	Home-made
Rabbit polyclonal Anti-COX5A	Home-made
Rabbit polyclonal Anti-COX6A	Home-made
Rabbit polyclonal Anti-IRF3	Cell Signaling Technology
Rabbit polyclonal Anti-Mitrac 7	Home-made
Rabbit polyclonal Anti-Mitrac12	Home-made
Rabbit polyclonal Anti-NDUFA9	Home-made
Rabbit polyclonal Anti-NDUFB8	Home-made
Rabbit polyclonal Anti-PARP	Cell Signaling Technology
Rabbit polyclonal Anti-pIRF3	Cell Signaling Technology
Rabbit polyclonal Anti-pTBK1	Cell Signaling Technology
Rabbit polyclonal Anti-RIESKE	Home-made
Rabbit polyclonal Anti-SDHC	Home-made

Rabbit polyclonal Anti-STING	Cell Signaling Technology
Rabbit polyclonal Anti-TBK1	Cell Signaling Technology
Rabbit polyclonal Anti-TIM21	Home-made
Rabbit polyclonal Anti-VDAC	Home-made
Rabbit polyclonal Anti-Parp1	Cell Signaling Technology
Rabbit polyclonal Anti-PLIN1	Cell Signaling Technology
Rabbit polyclonal Anti-NFKB	Cell Signaling Technology
Rabbit polyclonal Anti-NLRP3	Cell Signaling Technology
Rabbit polyclonal Anti-Mitofusin 1	Cell Signaling Technology
Rabbit polyclonal Anti-pIRF7	Cell Signaling Technology
Rabbit polyclonal Anti-RIG1	Cell Signaling Technology

Table 2.6: Secondary Antibodies

Antibody	**Supplier**
Goat α Rabbit IR880	LI-COR
Goat α Rabbit IR680	LI-COR
FITC α Mouse	Thermo Scientific

2.1.6 Primers

All Primers were ordered from Microsynth SeqLab and are listed in Table 2.7.

Table 2.7: Primers and Primerpairs

Primer	Sequence
RT_mCOA3_FP	AATGCTAAGAATGGAAATGCTCC
RT_mCOA3_RP	GGTGTAACCATAAATAGCTAACAC
RT_mS12_FP	GAAGCTGCCAAGGCCTTAGA

RT_mS12_RP	AACTGCAACCAACCACCTTC
RT_mCLPP_FP	TGGTGGAGCAGACGGGTCGAG
RT_mCLPP_RP	CACCACCTGGGCTGTTGATATAC
RT_mDNM1L_FP	GACAAATGAAATGGTGCATAACTTAG
RT_mDNM1L_RP	CTGCAGATGGGACCTTGTCCCG
RT_mER29_FP	GTCACTTTCTACAAGGTCATTCCC
RT_mER29_RP	AGCTTGTCGCCATAGTCTGAGATC
RT_mGAPDH_FP	TGTGAACGGATTTGGCCGTATTG
RT_mGAPDH_RP	CGTTGATGACAAGCTTCCCATTC
RT_mHPRT_FP	CTGATTATGGACAGGACTGAAAGAC
RT_mHPRT_RP	GATCATTACAGTAGCTCTTCAGTCTG
RT_mHSP60_FP	ATTAACACATCAAAAGGTCAAAAG
RT_mHSP60_RP	CCTGAAGACCAACTTTTAGCCTGTTC
RT_mMFN2_FP	TTTGGCCGGACGAGCAATGGGAAG
RT_mMFN2_RP	AGTTGGTTCACAGTCTTGACACTC
RT_mNRF1_FP	TTGGAGAATGTGGTGCGAAAG
RT_mNRF1_RP	GCTGAGCCTGGGTCATTTTGTC
RT_mp53_FP	AAGACTCCAGTGGGAACCTTCTG
RT_mp53_RP	AGGTGGGCAGCGCTCTCTTTG
RT_mPGC1a_FP	AGCCGTCTCTACTTAAGAAGC
RT_mPGC1a_RP	GCTCTTCGCTTTATTGCTCC
RT_mYME1L_FP	ACAGAAGACCAATGATTCCTTAAGGC
RT_mYME1L_RP	CTTCCTCCACCCCTTTAACATG
RT_mTFRC_FP	GACACCATCAAGCAGCTGAGC
RT_mTFRC_RP	TTGACCAATGCTGCTTTTCACTTG
RT_mCOX14_FP	ATGCCATCTGCCAAGCAGCTAG

RT_mCOX14_RP	CTGAGGTCTTCTGCTCTTCTGC
RT_mACTB_FP	AGATGACCCAGATCATGTTTG
RT_mACTB_RP	GAGCATAGCCCTCGTAGATG
RT_mEif4e3_FP	ACCACTTTGGGAGGAGGAGAG
RT_mEif4e3_RP	CACTCACGCTGACTCCGATG
RT_mGbp3_FP	TGGTGATGTAGAAAAGGGTGAC
RT_mGbp3_RP	CTCACTGGAGTCCTTCACTTTG
RT_mIfi27_FP	CAGTCTCTGGCACCATTCTA
RT_mIfi27_RP	CAAAGCAGGTTCCTCTCCAATG
RT_mIfit1_FP	ATGGGAGAGAATGCTGATGGTG
RT_mIfit1_RP	AACTGGACCTGCTCTGAGATTC
RT_mIfit3_FP	GGACATAGAAGGTCTCAGTGTG
RT_mIfit3_RP	CGCCATCTAGGTGCTTTATGTAG
RT_mIl2rb1_FP	GATCCTGCCAAGATGGTGAC
RT_mIl2rb1_RP	AGGCGTTACCCCCAAAGTAG
RT_mIrf7_FP	TGAGCGAAGAGAGCGAAGAG
RT_mIrf7_RP	GCCCACAGTAGATCCAAGC
RT_mIsg15_FP	AAGCAGATTGCCCAGAAGATTG
RT_mIsg15_RP	CTGTACCACTAGCATCACTGTG
RT_mOasl1_FP	CAGCAGACCCCACCAACAAT
RT_mOasl1_RP	GTGCTCTCTTCACCCTCCAG
RT_mPlekhb1_FP	ATTGGTTCGCTCTGTGGTTGG
RT_mPlekhb1_RP	CACATCCTGACACTCTTGGC
RT_mSerpine2_FP	GGTCCTACCCAAGTTCACAG
RT_mSerpine2_RP	TGGTTCCATCTTCACTGACTTC
RT_mUsp18_FP	TCGGTGATACCAAGGAACAGT

RT_mUsp18_RP	ATCCTTCCAGGTGACCCAAC
RT_mZbtb16_FP	TGGAGCAGCACAGGAAAC
RT_mZbtb16_RP	GAACTGGGCACCGCATTG
RT_mCYTB_FP	TTCATGTCGGACGAGGCTTA
RT_mCYTB_RP	ATGGGATGGCTGATAGGAGGT
RT_mATP6_FP	ACAGGCTTCCGACACAAACTA
RT_mATP6_RP	AGTAGCTCCTCCGATTAGGTGT
RT_mATP8_FP	CATCACAAACATTCCCACTGGC
RT_mATP8_RP	TGAGGCAAATAGATTTTCGTTCATT
RT_mCOX1_FP	ATGAGCAAAAGCCCACTTCG
RT_mCOX1_RP	GGTAGTCTGAGTAGCGTCGTG
RT_mCOX2_FP	AGACGAAATCAACAACCCCG
RT_mCOX2_RP	GGCAGAACGACTCGGTTATCA
RT_mCOX3_FP	TGCAGGATTCTTCTGAGCGT
RT_mCOX3_RP	AGTAGTGGGACTTCTAGAGGGTT
RT_m12S_FP	CGATAAACCCCGCTCTACCTC
RT_m12S_RP	GGCTACACCTTGACCTAACG
RT_m16S_FP	CGGCTAAACGAGGGTCCAAC
RT_m16S_RP	TATTCTCCGAGGTCACCCCAA
RT_mND1_FP	TCCCCTACCAATACCACACCC
RT_mND1_RP	GCTACGGCTCGTAAAGCTCC
RT_mND2_FP	ATAGGGGCATGAGGAGGACT
RT_mND2_RP	TGAGTAGAGTGAGGGATGGGTT
RT_mND3_FP	GCGGATTCGACCCTACAAGC
RT_mND3_RP	ATGGTAGTGGAAGTAGAAGAGCA
RT_mND4_FP	ACCCGATGAGGGAACCAAAC

RT_mND4_RP	AGCGTCTAAGGTGTGTGTTGT
RT_mND4L_FP	TATCCACATTACTATGCCTGGAAG
RT_mND4L_RP	TGATGGGGATTGGTATGGAGC
RT_mND5_FP	ACACATCTGTACCCACGCAT
RT_mND5_RP	GGCGAGGCTTCCGATTACTA
RT_mND6_FP	GGGTTTGGTGGATCGTTTTTAGG
RT_mND6_RP	TCCCCAAGTCTCTGGATATTCCT

Primerpair	**Primers**
Primerpair 1	mND6 RP + mCYTB RP
Primerpair 2	mCOX2FP + mATP6 RP
Primerpair 3	mRT16SFP + ND1 RP1

2.1.7 Software

All software, used for documentation and analysis is listed in Table 2.8.

Table 2.8: Software

Software	**Producer**
Word	Microsoft
Excel	Microsoft
ImageJ	Open Source
GraphPad Prism	Graph Pad
Adobe Illustrator	Adobe
Adobe Photoshop	Adobe
Image Quant TL	GE Healthcare
LEGENDplex™ data analysis software	Biolegend

2.2 Methods

2.2.1 Mouse Model

2.2.1.1 Maintenance of Mice

Maintenance of all mice and the study on them were performed according to the guidelines from the German Animal Welfare Act and approved by the Landesamt für Verbraucherschutz und Lebensmittelsicherheit, Niedersachsen, Germany (AZ: 33.9-42502-04-14/1720). The line $Cox14^{emAA1(M19I)Preh}$ used for this study was generated using CRISPR CAS mediated editing of *Cox14* allele to introduce missense mutation resulting in M19I change. The animals were kept either in high barrier (SPF-specified pathogen free) areas in IVC (individually ventilated caging) on standard rodent chow to WT C57BL/6N mice, with restricted access for animal care staff only. The genotype of the pups was assessed by PACE-PCR technology (3CR Bioscience, UK).

2.2.1.2 Phenotype Analysis

The Czech Centre for Phenogenomics (CCP) was commissioned to analyze the phenotype of COX14M19I in detail. The analysis included clinical diagnostics, such as blood parameters, histopathological examinations of various organs and fluorescence activated cell sorting (FACS) immunophenotyping, among many other factors.

Standard diagnostic tests, such as electrocardiography (ECG), echocardiography, pulmonary function screening, and electroencephalography analysis (EEG), were performed to describe the phenotype in detail.

2.2.1.3 Isolation of Mitochondria from Different Tissues

Immediately after the mice were sacrificed, the tissue samples were comminuted using glass potters (Table 2.3) in 15 ml of the tissue specific Isolation Buffers 1 (Table 2.2). Samples from Heart and Muscle were firstly prepared by incubation for 30 min at 24°C in 5 ml of Trypsin Digestion buffer under mild rotation (Table 2.2). The lysates were washed by centrifugation (600 g Heart and Muscle/ 700 g Liver and Brain, 10 min, 4°C) and the supernatant was saved.

Two centrifugation steps (7000 g Heart and Muscle/ 8000 g Liver and Brain, 10 min, 4°C) were executed, to separate the mitochondria from the cytosolic supernatant and wash them from excess tissue components, by adding fresh 5 ml of tissue specific Isolation Buffer 2

(Table 2.2) to the pellet. The isolated, pelleted mitochondria were diluted in 500 µl of the Isolation Buffer 2 and their protein concentration was estimated using bradford assay. All steps were done at 4°C, to prevent degradation processes.

2.2.1.4 Tissue Lysate Preparation

To prepare tissue lysates, tissue samples were comminuted with a hand homogenizer and plastic pestles in 1x Lysis Buffer (Table 2.2), working on ice. After determination of the protein concentrations using bradford assay, equal amounts were diluted in 1x Loading Dye (Table 2.2).

Isolated Mitochondria were centrifugated (8000 g, 15 min) and resuspended in 1x Loading Dye. All steps were performed at 4°C.

2.2.1.5 Electron Microscopy (EM) Analysis

Hepatocytes were isolated from mice liver using percoll purification, following the reported protocols with collagenase P (Horner et al. 2016).

After the tissue was rinsed with perfusion solution containing EGTA (Table 2.2), the liver was perfused with recirculating perfusion solution containing collagenase P (1 g/L). The resulting cell suspension was centrifuged (5 min, 50 g, 4°C) to remove cellular debris.

The isolated hepatocytes were cultured in William E medium (Table 2.1) for a week before fixation for EM analysis. The processing and imaging were performed by Dietmar Riedel at the Electron Microscopy facility of the Department of Structural Dynamics, Max Planck Institute for Biophysical Chemistry.

2.2.1.6 Mitochondrial Sucrose-Gradient Purification

To remove extramitochondrial nucleic acids from the isolated mitochondria, samples were first treated with 50 U Benzonase for 30 min, at 4°. Centrifugation (2x, 14000 g, 10 min, 4°C) and resuspension in IB (composition as described in mitochondrial isolation, containing 2.5 mM EDTA) stopped the Benzonase activity. A sucrose gradient was prepared by placing one volume of isolation buffer containing 1.7 M sucrose into a centrifuge tube and overlaying this with two volumes of isolation buffer containing 1 M sucrose. Mitochondria were finally resuspended in 1 M sucrose isolation buffer and carefully loaded onto the gradient. After

centrifugation for 25 min, 25.000 rpm (SW41Ti, Beckman Coulter) at 4°C, mitochondria were isolated from the interphase.

2.2.2 Molecular Biology Techniques

2.2.2.1 RNA Isolation and Purification

The tissue samples were comminuted in 1000 µl trizol. In order to isolate RNA from the Cytosol samples, 500 µl Cytosol solution was mixed thoroughly 1:1 with 500 µl of trizol. To separate the RNA, 200 µl chloroform was added to the lysates and by spinning (15 min, 12000 g), the nucleic acids were extracted and separated from the tissue. To wash and concentrate the RNA sample, isopropanol and ethanol were added successively and the samples were centrifuged (10 min. at 12000 g at 4°C and 5 min. at 7500 g, 4°C) at any one time. Ethanol was removed by drying the sample at 37°C. The RNA pellet was resuspended in 50 µl of RNAse free Water and resolved by heating the sample for 10 min at 60°C.

To purify the RNA, the samples were treated with DNase I, using the Thermo Scientific DNase I, RNase free Kit (Table 2.4) following the required protocol. For purification of the sample, the Zymo Research RNA Clean and Concentrator Kit (Table 2.4) was used to have highest RNA purification standards, following the manufacturer's instructions. The RNA quality and concentration were measured using Nanodrop 2000.

2.2.2.2 First strand cDNA Synthesis

In order to prepare the cDNA from isolated mRNA, instructions were operated according to Thermo Scientific First Strand cDNA Synthesis Kit (Table 2.4) using reverse transcriptase. The mRNA was diluted 50 µg/ml and 25 µg/ml.

A Sensequest labcycler (Table 2.3) was used for preparing the default reaction conditions (25°C, 5 min; 37°C, 1 h; 70°C , 5 min; 4°C, ∞).

2.2.2.3 Real Time quantitative Polymerase Chain Reaction (PCR)

For amplification and quantification of DNA fragments, primers were designed according to the aimed gene sequences (Table 2.7). The Primers were added in 1:100 concentration, diluted in Sensimix (Table 2.4).

The cDNA samples were diluted 1:100/1:50 or 1:25 in Water, to achieve a final concentration of 500 ng/ml in the sample-primer mix. Samples from isolated mtDNA were loaded in a concentration of 2 ug/ml. Stratagene Mx3000P and iMark Microplatereader (Table 2.3) was used to amplify and measure the Cycle Threshold (CT) value. The PCR conditions were 10min at 95°C followed by 40 cycles of 95°C (30sec), annealing for 20 sec at 58°C and 30 sec at 72°C for elongation.

2.2.2.4 Polymerase Chain Reaction (PCR) with Mitochondrial DNA (mtDNA)

Following the mtDNA Isolation from the cytosol or the isolated mitochondria, a PCR was performed to amplify mtDNA fragments. Three different primer pairs (Table 2.7) were selected representing different parts of the mtDNA and in order to cover as much of the mtDNA as possible, specifically amplifying mtDNA segments. The primers were diluted 1:100 in Water and 10ng of the mtDNA samples was added. The real time PCR was performed using Taq Polymerase from KOD Hot Start DNA Polymerase kit, following the manufacturer's instructions.

The PCR conditions were 3 min at 95°C, followed by 35 cycles of 95°C (30 sec), annealing for 30 sec at 58°C and 90 sec at 68°C for elongation.

2.2.2.5 Isolation of Mitochondrial DNA from the Cytosol/ from the Mitochondria

The QIAamp® DNA Blood Mini Kit was used to isolate mitochondrial DNA from the Cytosol or from the mitochondria.

For isolation of mtDNA from mitochondria, the isolated mitochondria following the mitochondria isolation protocols (see above) were diluted 1:50 in the provided sample buffer and the manufacturer's protocol was executed.

For isolation of mtDNA from the Cytosol of the tissue cells, the tissue samples were comminuted, mixed and washed in mitochondrial isolation buffer, following the protocol for the isolation of mitochondria from tissue samples in first place until the first high-spin centrifugation step (see above). In order to separate the cytosol from the mitochondria in the sample, the lysed tissue samples were centrifuged (7000 g/ 8000 g, 10 min, 4°C) to pellet the mitochondria. The upper cytosolic fraction was stored.

The cytosol sample was treated with 0.2 mg/ml RNAse A for 15 min at 4°C, to purify the DNA. The sample was diluted 1:1 in Buffer AL (Table 2.2) and then treated with 0.2 mg/ml

Proteinase K (Table 2.1), incubating at 56°C for 10 min. 33% Ethanol was added and a QIAamp Spin Column was used to isolate the DNA from the sample by centrifugation (6000 g, 1 min). Buffer AW2 (provided in the Kit) was added and the column was centrifuged at full speed for 3 min to wash the column. Distilled water was used to elute the mtDNA by two final centrifugation steps (6000 g, 1 min, 4°C).

2.2.2.6 Isolation of Mitochondrial RNA from the Cytosol

For isolation of mtRNA from the Cytosol of the tissue cells, the tissue samples were comminuted, mixed and washed in mitochondrial isolation buffer, following the protocol for the isolation of mitochondria from tissue samples in first place until the first high-spin centrifugation step (see above). In order to separate the cytosol from the mitochondria in the sample, the lysed tissue samples were centrifuged (7000 g/8000 g, 10 min, 4°C) to pellet the mitochondria. The upper cytosolic fraction was stored.

In order to isolate RNA from the Cytosol samples, 500 µl Cytosol solution was mixed thoroughly 1:1 with 500 µl of trizol. To separate the RNA, 200 µl chloroform was added to the lysates and by spinning (15 min, 12000 g), the nucleic acids were extracted and separated from the tissue. The RNA was diluted in 100% Ethanol and the Zymo Research RNA Clean and Concentrator Kit (Table 2.4) was used to have highest RNA purification standards, following the manufacturer's instructions. The RNA quality and concentration were measured using Nanodrop 2000.

2.2.2.7 Agarose Gel Electrophoresis

Agarose gel electrophoresis was performed to confirm the presence of a specific PCR

product and to compare the amounts of amplified DNA fragments. The separation of DNA was conducted in a 1% agarose gel. Therefore, dry agarose was dissolved in 1x TAE buffer (Table 2.2) and ethidium bromide (1 ug/ml) was added.

After casting the agarose gel in the gel casting apparatus (Table 2.3), DNA loading dye, containing glycerol (Table 2.2) was added to the PCR reaction products. 10 ul of the samples and the DNA ladder mix (Table 2.4) were loaded into the slots of the gel. The gel was run for 20 min at 120 V. UV-light was used to visualize the DNA fragments.

2.2.2.8 RNA Sequencing

NGS-Serviceeinrichtung für Integrative Genomik (NIG) was commissioned to analyze the isolated mRNA samples using RNA sequencing. The services included statistical analyzation of the results.

2.2.2.9 Library Preparation

Total mitochondrial RNA was purified and concentrated on an RNA Clean Concentrator™-5 column (Zymo Research, Irvine, CA, USA). cDNA libraries were prepared from a mix of 50 ng RNA and 0.5 ng Spike-in RNA Variant Control Mix E2 (Lexogen) according to the Oxford Nanopore Technologies (Oxford Nanopore Technologies Ltd, Oxford, UK) protocol "DNA-PCR Sequencing" with a 14 cycles PCR (8 min for elongation time). ONT adapters were ligated to 650 ng of cDNA.

2.2.2.10 Nanopore Sequencing and Analysis

Nanopore libraries were sequenced using a MinION Mk1b with R9.4.1 flowcells. The data were generated and basedcalled using MinKNOW (Version 21.11.9). The fastq files were then uploaded to and analyzed using the Epi2Me Labs (Version 1.1) Differential Gene Expression workflow. Transcript counts obtained were processed for heatmap and volcano plot generation using Prism 9 software (GraphPad Software, San Diego, CA).

2.2.3 Protein and Protein Complex Analysis

2.2.3.1 Determination of Protein Concentration using Bradford assay

The concentration of proteins from isolated mitochondria was determined using ROTI®Quant reagent (Table 2.1). After isolation, the solution was diluted in distilled water in concentrations of 1:100, 1:200 and 1:400. A standard curve was determined by different concentrations of bovine serum albumin (BSA) (1 µg, 0.5 µg, 0.25 µg and 0.125 µg per 100 µl water). After addition of fivefold diluted ROTI®Quant reagent the optical density of the solution was measured at a wavelength of 595 nm using a Cary 50 Bio UV-visible spectrophotometer. The protein concentrations were calculated from the optical density of the solution using the BSA standard curve.

2.2.3.2 Tricine- SDS- PAGE

The special SDS-Page is designed for better separation of smaller proteins below 15 kDa. For this purpose, a polyacrylamide gel was prepared from Tris-Tricine with a gradient of 10-18%. The 10% gel contained 0.1% SDS, 1 MTris/HCl (pH 8.45) 49.5%/3% acrylamide/bis-acrylamide solution. An additional 13% glycerol was added to the 18% gel. APS and TEMED triggered the gel polymerization. The gradient gel was poured using a home-made gel mixer. A "stacking gel" was prepared from 0.1% SDS, 4% acrylamide and 1 M Tris/HCl (pH 8.45). It was poured on the 10% gel side. SDS sample buffers (Table 2.2) were added to the samples as colorants before loading and heated for 20 min at 37 °C. The chambers were then loaded with a volume of 10 µl/ 20 µl/ 30 µl. SDS sample buffers (Table 2.2) were added to the samples as colorants before loading and heated for 20 min at 37°C. Electrophoresis was performed overnight with 80 V, 25 mA and 100 W.

2.2.3.3 Blue- Native- PAGE

A homemade mini-Blue-Native-multi-Gel-apparatus was used to cast 4%-13% polyacrylamide Blue Native Gels (Table 2.2) and a BN stacking gel (Table 2.2), which was placed in top of the 4% gradient, in order to separate protein complexes. APS and TEMED triggered the gel polymerization. All following steps were done at 4°C. The isolated mitochondria were solubilized using BN Solubization Buffer containing either 20% Digitonin or 20%/36% DDM (Table 2.2). After incubation (20 min, 4°C) and centrifugation (top speed, 10 min, 4°C), the protein complexes were diluted in BN loading Buffer (Table 2.2) and 40 ug were loaded. Precooled Running Buffer and Cathode Buffer containing Coomassie Brilliant Blue G-250 was added and the gel was run at 15 mA/ 100 V. After 1,30 h the Cathode Buffer was replaced with Coomassie-free Cathode Buffer and the gel was run for additional 3 h. The complexes were transferred on a PVDF membrane and detected following the Western Blot and Immunodetection protocols.

2.2.3.4 Göhrlich-SDS Page

A Göhrlich-SDS Page was used for the separation of bigger proteins over 15 kDa. The 12% or 16% polyacrylamide gel contained 0.75 M Tris/HCl (pH 8.8), 0.1 M Sucrose, 0.01% SDS and 2.5% Glycerol. A 4% acrylamide “stacking gel” was prepared from 0.01 M Tris/HCL

(pH 6.8) and 0.1% SDS. APS and TEMED triggered the gel polymerization. Samples were loaded (10 µl/ 20 µl/ 30 µl) after adding SDS Buffer (Table 2.2) and heating 20 min at 37°C. The electrophoresis was performed for 2.30 h with 80 V, 25 mA and 100 W.

2.2.3.5 Coomassie Brilliant Blue Staining

The PDVF membrane was stained with Coomassie Brilliant Blue staining solution (Table 2.2) for a few seconds. Destaining solution (Table 2.2) replaced Coomassie Solution to visualize the separated protein bands. Finally, the membrane was washed in methanol to remove all rests of the staining solution.

2.2.3.6 Western Blot and Immunodetection

Immunodetection after Western blot was applied to detect the separated proteins and to determine their exact concentration in the samples using monoclonal antibodies (Table 2.5). For the Western Blot, chambers of PEQLAB and PVDF membranes from Merck were used.

The PVDF membrane was first activated in methanol. It was then placed between the filter papers (Heinemann Labortechnik) and the electrophoresis gel. Prior to this, the filter papers and the gel were soaked in blot buffer (Table 2.2). To transfer the proteins of the gel to the membrane, the chamber was connected to a voltage source with 25 V, 250 mA and 100 W for two and a half hours (for SDS Page). For BN Page a voltage of 25 V, 300 mA and 100 W was used for three hours.

After transfer of the proteins, the protein bands were visualized using the Coomassie staining method and cut into individual strips according to the protein size that would later be investigated by immunodetection.

After activation of the membrane in methanol it was washed in TBS-T (Table 2.2). The membrane strips were then blocked with 5% milk (BN Pages were blocked in 10% milk) for one hour at room temperature under slight agitation. The membranes were then incubated overnight with light agitation with the homemade or commercial primary antibodies (Table 2.5). The strips were then washed three times with TBS-T and incubated with the secondary antibodies (Table 2.6) in the appropriate dilutions of TBS-T for one hour at room temperature with gentle agitation. In the end, the membranes were washed three more times in TBS-T. Finally, the membranes were incubated with Western Blotting Luminol Solution (Table 2.1) and the bands were analyzed using Image Quant 800 (Amersham).

2.2.3.7 Stripping of Western Blots

In order to disrupt the binding of the primary/secondary antibody to the proteins on the PVDF membrane, which developed during immunodetection from a prior experiment, the used membranes were firstly washed in TBST (2x, 10min). After activation of the membrane in methanol (10 min) and another washing step in TBST (1x, 10 min), the membranes were incubated twice for five minutes in Stripping Buffer (Table 2.2) under mild agitations. To control the methods efficiency, freshly stripped membranes were incubated again with secondary Antibody. According to Immunodetection protocol, Luminol solution and Image Quant 800 (Amersham) were used to detect the previous immunocomplexes.

Only after successful disruption of the Antibody binding, the membrane was used again for another experiment.

2.2.3.8 Autoradiography

To visualize radioactively labelled proteins, digital autoradiography was used. Radioactive samples were separated via electrophoresis and western blot was performed according to the protocol.

The membrane was destained and dried using a hairdryer. The molecular weight marker was marked with radioactive ink.

Radioactive signals were exposed to storage phosphor screens (GE Healthcare) for 1 day -1 week. A Typhoon FLA 9500 Phosphoimager was used to visualize the radioactive signals, which were quantified by ImageJ software.

2.2.3.9 Second Dimension

The second-dimension experiments aim to determine the composition of the protein complexes. First, BN Page (see above) was used to separate the complexes in the samples after performing an In Vivo S^{35} methionine radiolabeling experiment. The protein complexes separated in the BN gel were then resolved by Tris Tricine electrophoresis. For this purpose, a Tris Tricine gradient gel was cast and the BN gel strips containing the complexes were placed horizontally on top of the SDS gel. The 4% Stacking gel was added surrounding the BN Gel

Strips, avoiding the formation of air bubbles inside of the gel. Electrophoresis was performed according to the protocol to separate the protein subunits of the complexes.

The proteins in the SDS gel were then transferred to a PDVF membrane and finally detected using the autoradiography protocol.

2.2.4 Enzyme Activity

2.2.4.1 Oxygen Consumption Rate (Seahorse)

The Oxygen Consumption Rate (OCR) was measured to assess the functionality and effectivity of the respiratory chain. Following the isolation of mitochondria, the samples were resuspended in (2 μg/μl) MAS Buffer (Table 2.2). 20 μl were added to the Seahorse plate (Table 2.4) and the plate was incubated by spinning at 2000 g, 4°C for 20 min. Another 160 μl MAS Buffer was added (for Succinate consumption, 2 μM Rotenone was added) and the plate was inserted into the XF96 Extracellular Flux Analyzer (Table 2.3).

Pyruvate mix and succinate mix (Table 2.2) were added as a substrate for the respiratory chain. Successively, oligomycin, FCCP and KCN were added and the Oxygen Consumption Rate was measured.

2.2.4.2 Complex Activity Measurements

The Complex I Enzyme Activity Microplate Assay Kit (Table 2.4), was used to assess the activity of the NADH dehydrogenase. The assay was executed as to the corresponding protocol. The activity of the Complex I is determined by following the oxidation of NADH to NAD+ and the simultaneous reduction of a dye, which is measured due to its change in absorbance using a synergy microplate reader (Table 2.3).

The Complex II Enzyme Activity Microplate Assay Kit (Table 2.4), was used to assess the activity of the succinate dehydrogenase. The assay was executed as to the corresponding protocol. A synergy microplate reader was used to measure the color change of DCPIP, which turns colorless due to its reduction by ubiquinol.

The Complex IV Rodent Enzyme Activity Microplate Assay Kit (Table 2.4), was used to assess the activity of the Cytochrome C Oxidases. The assay was executed as to the corresponding protocol. A synergy microplate reader was used to measure the absorbance of Cytochrome C, which turns colorless due to its oxidation.

2.2.4.3 Mitochondrial Membrane Potential Measurement

Membrane potential measurement was conducted on isolated liver mitochondria (as described above) using a Flow Cytometer (FACSCanto, BD Biosciences). The mitochondria were resuspended in freshly prepared Analysis buffer (pH 7.0; 250 mM Sucrose, 20 mM Tris-MOPS, 100 µM Pi(K), 0.5 mM $MgCl_2$, 5 mM Succinate, 2 µM Rotenone). 100 µM Tetramethylrhodamin-methylester-perchlorat, TMRM (Life Tech; T668) was added to all samples except the unstained control and the samples were incubated for ten minutes at room temperature, protected from light. The measurement was done at Ex488/Em590 nm.

2.2.4.4 NAD/NADH Measurement

Quantification of NAD^+/NADH ratio in mouse liver tissue samples was done using a NAD^+/NADH Quantification Kit (Sigma-Aldrich; MAK037). The protocol provided by the supplier was followed. NAD_{total} as well as NADH were detected measuring absorbance at 450 nm on a microplate reader (Synergy H1; BioTek; 8041000) following mechanical lysis and deproteination of the lysates. In order to measure NADH separately from the NAD_{total}, NAD^+ was thermally decomposed by a 30 min incubation at 60°C.

2.2.4.5 ATP Measurement

Measurement of total tissue ATP content was done using the ATP Assay Kit (Colorimetric/Fluorometric) (Abcam; ab83355) and as specified by the protocol from the supplier. In order to determine total ATP mouse liver tissue was lysed mechanically and deproteinized. Samples were incubated for 30 min at room temperature with the reaction mix in triplicates. The phosphorylation of glycerol resulting in a product detectable at 570 nm was measured using a microplate reader (Synergy H1; BioTek; 8041000).

2.2.4.6 Lactate Measurement

L-Lactate Assay Kit (Colorimetric/Fluorometric) (Abcam; ab65330) was used in order to detect lactate in mouse liver tissue lysate. The experiment was performed as instructed in the protocol provided by the supplier. Following mechanical lysis, the samples were deproteinized and assayed for 30 min. Lactate was detected calorimetrically at 570 nm. The measurement was done in triplicate and visualized using a microplate reader (Synergy H1; BioTek; 8041000).

2.2.5 Clinical Diagnostics

2.2.5.1 Serum Blood sample preparation

Directly after sacrificing a mouse, the blood was taken from the Vena Porta Hepatis and kept in an EDTA tube. The blood was centrifuged (4°C, 2000 g, 20 min) and the upper serum layer was either stored at -20°C or freshly used for the assays.

2.2.5.2 Autoantibody Diagnostics

AESKU.DIAGNOSTICS Kit (Table 2.4) for Autoantibody Analysis was used for Antinuclear Antibody (ANA) Measurements, following the manufactures instructions. Human HEP 2 cells were incubated with different Serum Concentrations (1:10, 1:20, 1:40, 1:80, 1:160), diluted in the provided sample buffer. The autoantibodies were visualized using different FITC-anti mouse antibody concentrations (1:16, 1:32, 1:64, 1:128) and diagnosed in fluorescence microscopy.

The indirect immunofluorescence test (Table 2.4) was used for detection of antimitochondrial antibodies (AMAs), following the manufactures instructions. Mouse kidney samples were incubated with different serum concentrations (1:10, 1:20). The autoantibodies were visualized using different FITC-anti mouse antibody concentrations (1:8, 1:16) and diagnosed in fluorescence microscopy.

2.2.5.3 Blood Value Measurements

In order to get more insights into tissue specific pathological mechanisms, the Universitätsmedizin Göttingen (UMG) - Routine laboratory was commissioned to analyze the blood samples using the standardized clinical test methods for selected blood parameters.

2.2.5.4 Immune Response Assay

The bead-based immunoassay (Table 2.4) using flowcytometry to quantify different proteins involved in the antiviral immune response in the blood system. The manufacturer's instructions were followed.

The serum samples were diluted and incubated with the specific beads. After washing, biotinylated detection antibodies were added, thus forming capture bead-analyte-detection antibody sandwiches. Streptavidin-phycoerythrin (SA-PE) was subsequently added, providing fluorescent signal with intensities in proportion to the amount of bound analyte. For each bead population, the PE signal fluorescence intensity was quantified using a flow cytometer (Table 2.3).

The concentration of a particular analyte was determined based on a known standard curve using the LEGENDplex™ data analysis software.

2.2.6 Specialized Assays

2.2.7 In Vivo S^{35} Methionine Radiolabeling

Isolated mitochondria were incubated in translation buffer (Table 2.2) for 10 min at 37ºC. ^{35}S methionine was added and after 1 h/2 h incubation at 37ºC, the translation was stopped. The mitochondrial proteins were separated via spinning 10 min at 4ºC.

To separate the newly translated mitochondrial proteins, Tris Tricine Electrophoresis was performed and the proteins were detected using Western Blot and autoradiography.

2.2.8 Immunoprecipitation

After in vivo ^{35}S methionine labeling was performed to mark mitochondrial proteins in purified mitochondria, the samples were incubated 30 min in solubilization buffer (Table 2.2).

Insolubilized debris was removed by spinning (16000 g, 15 min, 4°C) and solubilized samples were added to the movicol column (M2 Affinity Matrix (Sigma), 4G), containing the specific antibodies.

Before hance the column was equilibrated, by adding washing buffer (Table 2.2) and centrifugation at 100 g, 30 sec. The samples were incubated with the beads for 1 h at 4°C under mild rotations. Afterwards, unbound material was removed by centrifugation at 200 g, 1 min and the beads were washed 10 times with 500 µl washing buffer (all centrifugation steps 100 g, 30 sec, 4°C). Glycine (0.1 M, pH 2.8) was added to the column to elute all bound proteins from the column and the sample was incubated for seven minutes at room temperature. The elution was mixed with SDS loading dye (Table 2.2) and SDS tris tricine electrophoresis was executed. The radioactive signals were analyzed using autoradiography. Afterwards, unbound proteins were detected using western blot and immunodetection protocol.

2.2.9 Pulse Chase

The Pulse Chase experiment was performed to assess the stability and turnover of freshly translated mitochondrial proteins. After executing in vivo ^{35}S methionine labeling for 1h to radioactively mark translated proteins with ^{35}S methionine, "cold methionine" was added as a non-radioactive substrate. Translation was stopped after different timepoints (0 min, 20 min, 1h) and the proteins were separated in electrophoresis using a tris tricine SDS gel. The proteins were transferred on a PDVF membrane and finally detected executing autoradiography protocol.

2.2.10 Mitochondrial Transcriptome Analysis

To purify the isolated mitochondria from extramitochondrial nucleic acids, samples were firstly treated with benzoase for 30 min, at 4°C. Centrifugation (2x, 14000 g, 10 min, 4°C) and resuspension in isolation buffer (see above) containing 2.5 mM EDTA purified the sample and stopped the benzoase activity.

A sucrose gradient was prepared by placing 3 ml of isolation buffer (see above) containing 1.7 M sucrose into a centrifuge tube and overlaying this with 6 ml of isolation buffer

containing 1 M sucrose. Mitochondria were finally resuspended in 1 M sucrose isolation buffer and carefully loaded onto the gradient. After centrifugation (25 min, 25000 rpm, 4°C), purified mitochondria were isolated from the interphase and dissolved in 2 ml Trizol.

RNA was isolated from the purified mitochondria, according to the described protocol (see 2.2.2.1).

The following steps were conducted using the cDNA-PCR Sequencing Kit from Oxford nanopore technologies. After RNA was cleaned and concentrated, cDNA was prepared using reverse transcriptase from 30 ng of the isolated RNA. A Sensequest labcycler (Table 2.3) was used for preparing the default reaction conditions (42°C, 90 min; 85°C, 5 min; 4°C, ∞).

Afterwards, bar code primers were used to label the individual cDNA samples. For this, 5ul of cDNA was used and the manufacturer's instructions were carried out. To anneal the bar code primers, DNA was amplified under following conditions: 95°C, 30 sec; 95°C, 15 sec (11 cycles); 62°C, 15 sec (11 cycles); 65°C, 50 sec per kb (11 cycles); final 65°C, 6 min; 4°C, ∞.

Exonuclease treatment was conducted in order to clean the sample (37°C, 15 min; 80°C, 15 min).

Using magnetic beats, the samples were washed in 200 µl of 70% ethanol and finally, the concentration of the samples was measured to use equal amounts of nucleic acids for sequencing. Only 100 fmol of each sample was loaded in the SpotON flow cell, which performed real time sequencing using 512 separate channels.

3 Results: Chapter One

3.1 The Role of Cox14 in Cox1 Translation and MITRAC Complex Assembly

Using CRISPR/Cas-mediated genome editing, a mouse line (henceforth referred to as COX14M19I) was designed to mimic the human mutation in mouse *Cox14* in order to gain more insight into the function of Cox14.

To investigate the effects of the Cox14 mutation on mitochondrial translation in mice, mitochondria were isolated from brain samples and subjected to *in-organello* translation assays in the presence of ^{35}S methionine. The radiolabeled translation products were assessed using SDS-PAGE and autoradiography. Only Cox1 signals in COX14M19I brain mitochondria were reduced to 6% of wild type, indicating that translation of Cox1 was drastically reduced by the Cox14 mutation (Figure 3.1 (A), Figure A.1). The translation of all other mitochondrial proteins was unaffected. This is in agreement with the current view that Cox14 acts as a Cox1-specific translational factor.

To further analyze the stability and turnover of the newly translated Cox1 protein in brain mitochondria, a "pulse chase" experiment was designed. For this purpose, levels of newly translated radiolabeled mitochondrial proteins were measured at 20 min and 1 h after their translation. Wild type Cox1 showed signals of 98% of initial signals after 20 min chase. However, signals of Cox1 in COX14M19I were reduced to 80%. After 1 h, signals of Cox1 in wild type further decreased by 17% to 83%, whereas in COX14M19I they decreased by 34% to 66% of baseline signals (Figure 3.1 (C), Figure A.**1**).

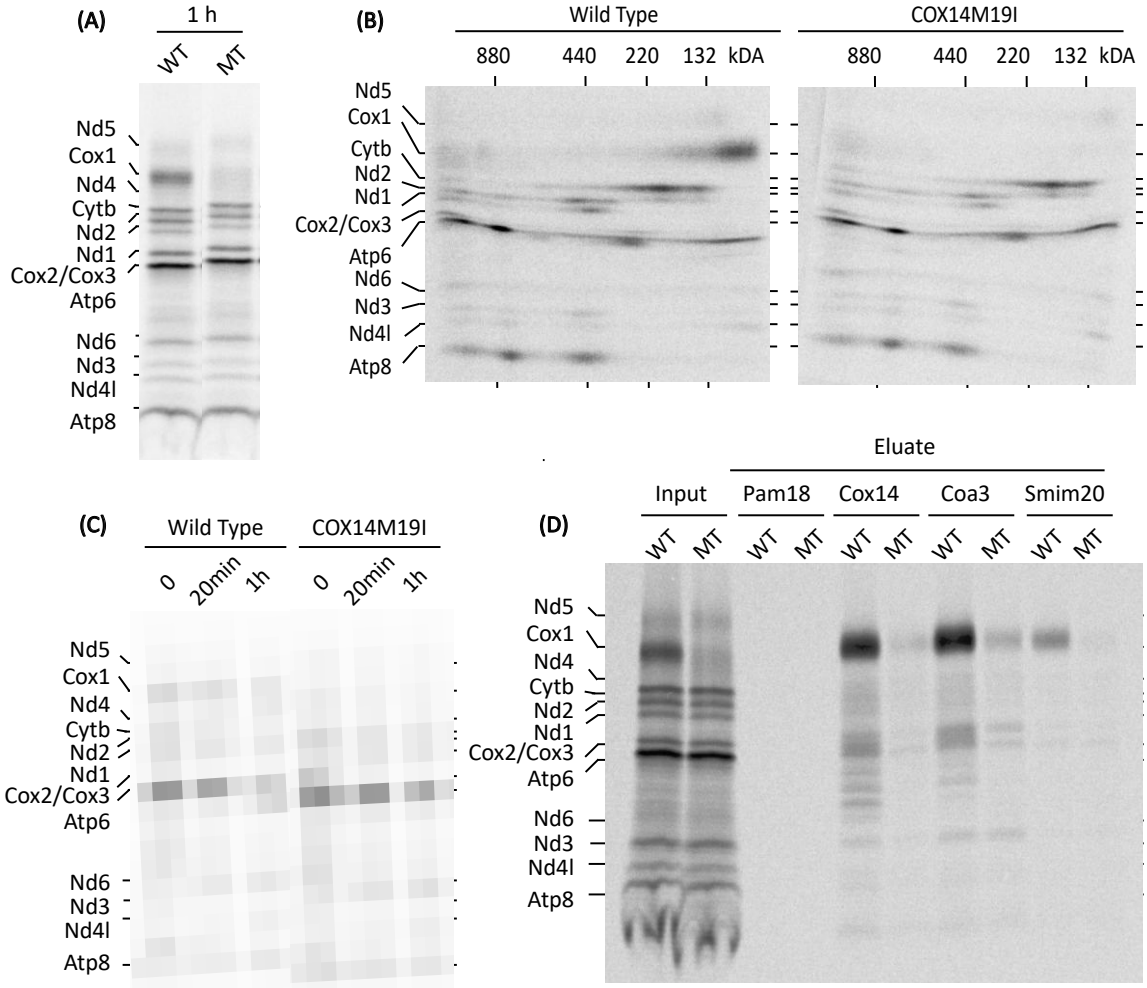

Figure 3.1: Cox14 Mutation Causes a Decrease in Cox1 Levels and MITRAC Complex Assembly.

Mitochondria were isolated from brain samples and treated with ^{35}S methionine for 1h, to radiolabel newly translated mitochondrial proteins.

(A) Translation products were assed using SDS-PAGE and autoradiography.

(B) Mitochondrial proteins were solubilized in digitonin and complexes were analyzed using 2D BN-SDS-PAGE. Autoradiography was used to detect radiolabeled proteins.

(C) After in vivo labeling was stopped, mitochondria were incubated at 37°C for 20min and 1 hour with non-radioactive methionine (chase). SDS-PAGE and autoradiography were performed to assess the stability of the newly translated mitochondrial proteins.

(D) Antibodies against Pam18, Cox14, Coa3 and Smim20 were used for immunoprecipitation to show newly translated mitochondrial proteins in association with MITRAC complex components. Autoradiography was used to identify mitochondrial proteins. MT, COX14M19I; WT, Wild Type.

Next, we wanted to assess if there were disturbances in the integration of the newly translated mitochondrial protein into respiratory complexes. Thus, different respiratory complexes were

resolved into their component subunits using two-dimensional Blue Native (BN) and subsequent SDS-PAGE analysis. In COX14M19I, there was a massive decrease in the signal at 132 kDA. This complex corresponds to Cox1 in the MITRAC complex (Mick et al. 2012; Wang et al. 2020). Signals from other complexes remained unaffected (Figure 3.1 (B)).

Since the abovementioned results indicated a disturbed assembly of the MITRAC complex, consequences of the Cox14 mutation on MITRAC subunit interactions were analyzed by immunoprecipitations in mitochondria subjected to *in organello* labeling. Antibodies against Cox14, Coa3 and Smim20 were used to bind mitochondrial proteins in association with MITRAC complex components and Pam18 was used as a negative control (Figure 3.1 (D)). Cox1 was detected in only minimal amounts in association with the assembly factors, compared to wild type.

Thus, not only Cox1 translation, but also its interaction with these assembly factors was strongly reduced (Figure 3.1 (D), Figure A.1).

3.2 Effects of the Cox14 Mutation on the OXPHOS System

3.2.1 Quantification of OXPHOS Proteins and OXPHOS Complexes Showed Tissue-specific Differences

The phenotype of mitochondrial disorders is very heterogeneous and shows different, organ-specific effects (Robinson 2000; Shoubridge 2001; Nunnari and Suomalainen 2012). Therefore, consequences of the Cox14 mutation were analyzed and compared in four different organs such as brain, liver, heart and muscle.

SDS-PAGE and immunoblotting was performed, to quantify steady state protein levels using voltage-dependent anion channel (VDAC) signals as a reference. VDAC is localized in the OMM and plays no role in the respiratory chain or in Complex IV assembly. Furthermore, it showed the same abundance in both cohorts. A significant reduction of Cox1 was observed in all tissues (Figure 3.2 (A)), with the highest reduction seen in liver and brain (below 40% of wild-type levels), followed by a reduction to 50% of wild-type levels in heart and muscle (Figure A.2). Other subunits of Complex IV, Cox5a, Cox6a and Cox4I, were also significantly

reduced in all tissues to a similar extent as Cox1. The levels of MITRAC complex components Cox14 and Smim20 were also significantly reduced in all tissues. Coa3 levels were only reduced in liver and brain, but not in muscle and heart (Figure 3.2 (A)). Signals of other OXPHOS proteins did not show significant differences.

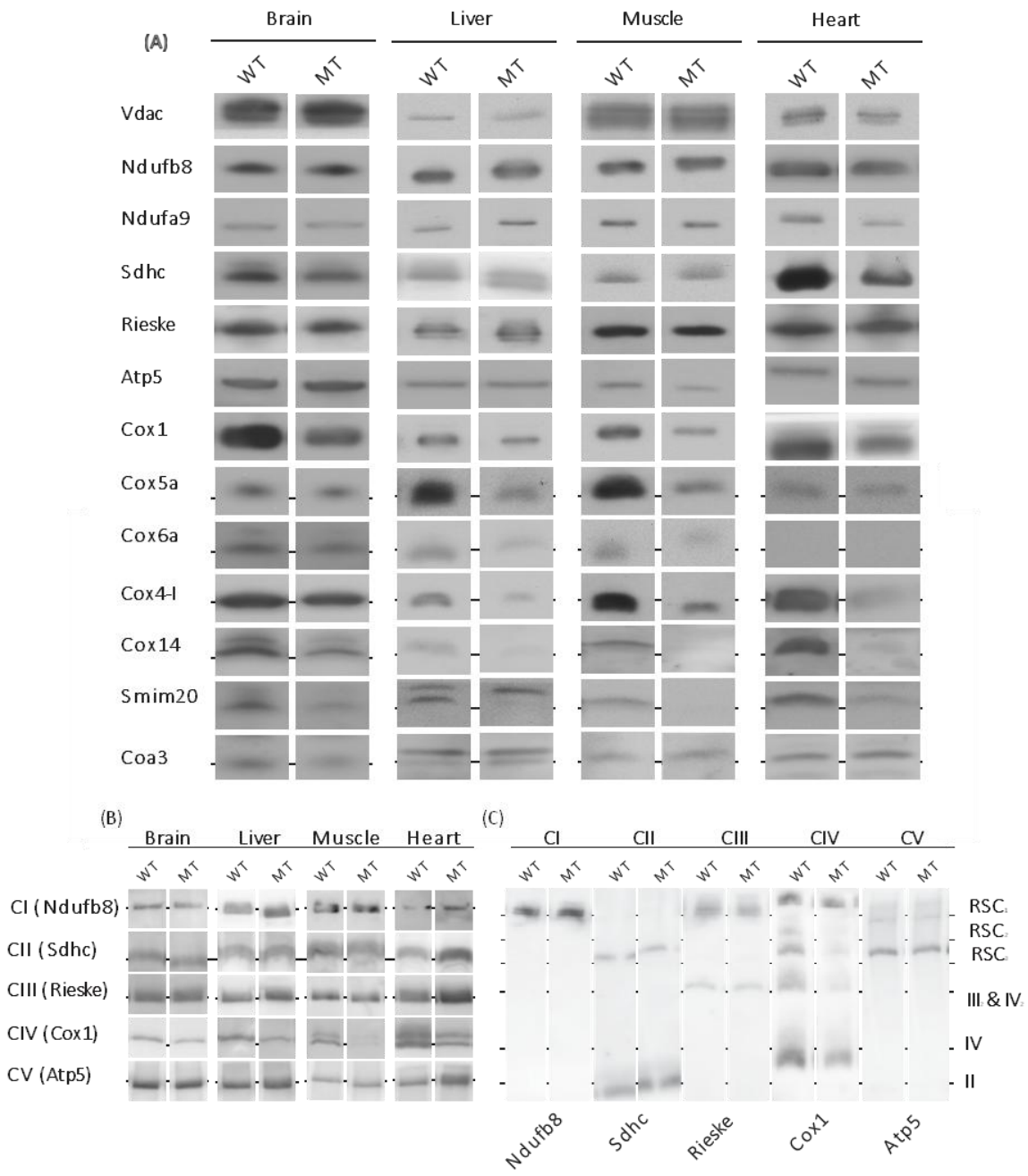

Figure 3.2: OXPHOS Complexes and Protein Levels showed tissue-dependent differences.

Mitochondria were isolated from Brain, Liver, Muscle and Heart.

(A) SDS-PAGE and immunoblotting was conducted with isolated mitochondria to address OXPHOS protein levels.

(B) Isolated Mitochondria were solubilized in DDM and the complexes were separated by BN-PAGE. Immunoblotting was used to visualize the different complexes, using Antibodies against one of the complexes subunits.

(C) Mitochondria were isolated from brain and solubilized in digitonin. BN-PAGE and immunoblotting were performed to analyze different super complexes. See Appendix Figure A.3 for details.

WT, Wild Type; MT, COX14M19I; RSC_1, Respiratory Super Complex 1; RSC_2, Respiratory Super Complex 2; RSC_3, Respiratory Super Complex 3; III_2 and IV_2, Dimeric Complex III and IV; IV_1, monomeric Complex IV; II_1, monomeric Complex II

In addition, BN-PAGE was performed to quantify amounts of respiratory chain complexes and super complex formation. Immunodetection was used to quantify the different complexes, using antibodies against one of the complexes subunits (Anti-NDUFB8 for Complex I, Anti-SDHC for Complex II, Anti-RIESKE for Complex III, Anti-COX4-I for Complex IV, Anti-ATP5 for Complex V). Signals from Complex V were used as a reference for quantification, as it showed equal amounts in all tissues.

BN-PAGE, using DDM for solubilization revealed that Complex V remained equal in wild type and COX14M19I in all tissues. Also, the levels of Complex I, II and III did not show a significant change (Figure 3.2 (B)). While Complex IV levels were significantly reduced in heart (25%), muscle (10%) and liver (65%), Complex IV amounts remained unaffected in Brain (Figure A.2). The respiratory chain complexes have been shown to form super complexes, presumably to achieve greater efficiency of the electron transport chain (Brave and Becker 2020). To study the assembly of super complexes, BN-PAGE analysis was performed with mitochondria isolated from the brain and solubilized in digitonin, leaving the super complexes intact. The assembly of Complex IV into intermediate super complexes (RSC2 and RSC3) and intermediate respiratory complexes was hampered in COX14M19I (Figure 3.2 (C), Figure A.3). The other complexes did not show differences in the formation of super complexes.

3.2.2 Tissue-specific Differences of OXPHOS Activity

Since it was shown, that Cox14 mutation affected the levels of OXPHOS proteins and complexes, the activity of the OXPHOS system was analyzed in the four different tissues.

Oxygen consumption rate (OCR) was measured under different conditions using seahorse real time respirometry. Pyruvate and succinate were used as substrates to either feed electrons into the ETC via Complex I or Complex II. Oligomycin was added to block Complex V thus measuring the coupled respiration. The protonophore CCCP was used to uncouple the respiratory chain to determine the maximal respiration rate and Potassium Cyanide (KCN) was used to block the respiratory chain by binding to the oxygen binding site of Complex IV.

Tissue-specific differences were evident in the overall activity of the OXPHOS system, measured as oxygen consumption rate (Figure 3.3 (A)). In particular, it was found that the OXPHOS activity in brain remained unaffected with either succinate or pyruvate as substrates (Figure 3.3 (A)). In contrast, COX14M19I mitochondria showed a reduced OXPHOS activity in muscle, heart and liver. In all three organs, basal and maximal respiration were reduced. In addition, Complex I and IV activity were analyzed, to specifically investigate the individual respiratory chain complexes.

Complex I and Complex IV were coated to an assay plate and the oxidation of NADH and cytochrome c, respectively, where measured colorimetrically. Whereas Complex IV in brain of COX14M19I showed very little reduction compared to the wild type, Complex IV activity in liver was greatly reduced by about 75% percent. Complex IV activity in heart and muscle was slightly decreased, by 30% and 10% compared to the wild type, respectively (Figure 3.3 (C)). In brain, liver and muscle, Complex I of COX14M19I showed no significant difference in the NADH oxidation compared to the wild type (Figure 3.3 (C)). In stark contrast, activity of Complex I in heart was strongly increased in response to the Cox14 mutation (Figure 3.3 (C)).

In summary, the liver appeared to be most affected by the deficiency, followed by muscle and heart, while the brain showed only mild alterations.

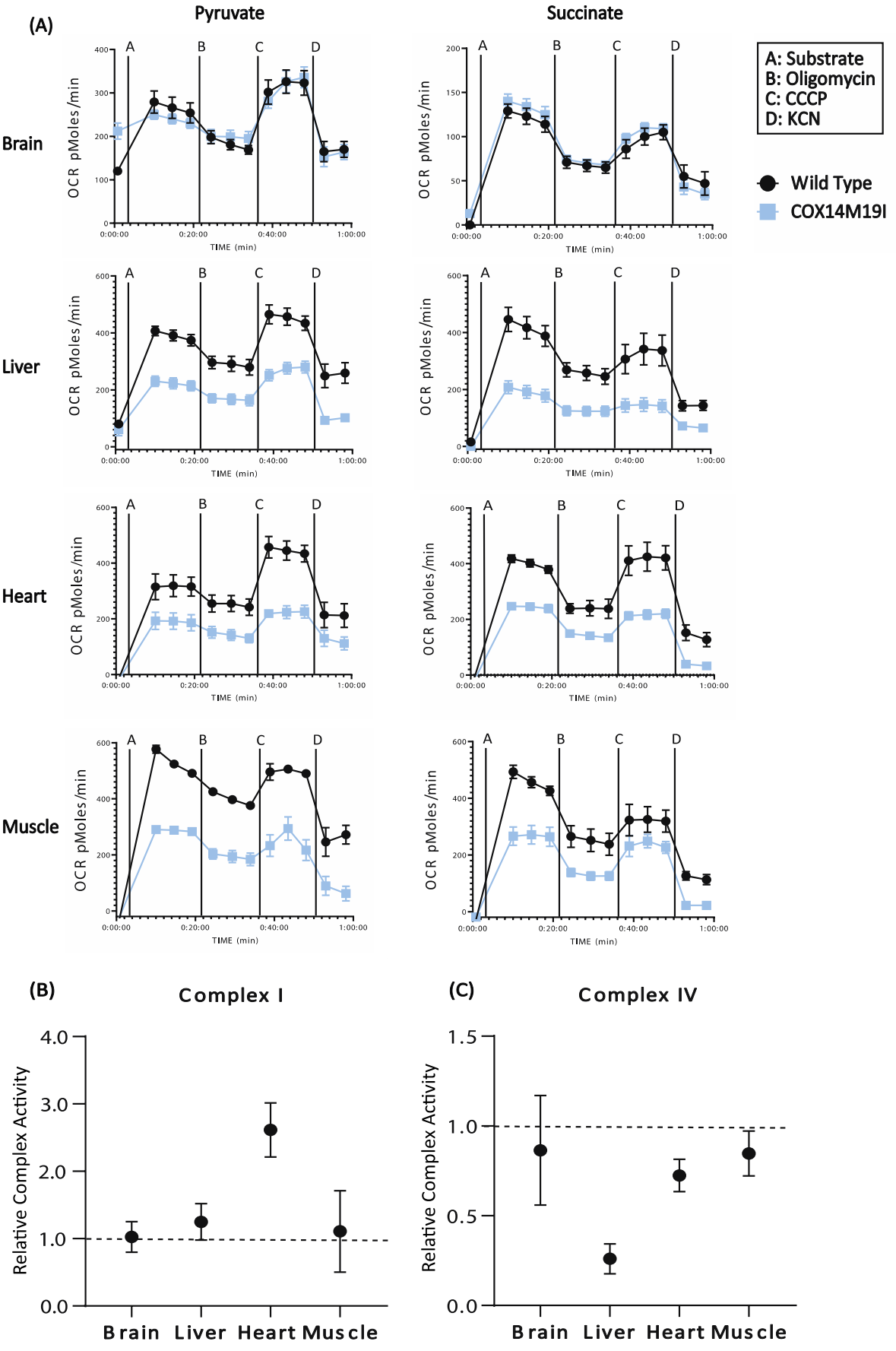
(A)
Pyruvate
Succinate
A: Substrate
B: Oligomycin
C: CCCP
D: KCN
Wild Type
COX14M19I
Brain
Liver
Heart
Muscle
OCR pMoles/min
TIME (min)
(B)
Complex I
(C)
Complex IV
Relative Complex Activity
Brain
Liver
Heart
Muscle

Figure 3.3: OXPHOS system, Complex I and Complex IV activity varied in different tissues.

(A) Mitochondria were isolated from Brain, Liver, Heart and Muscle and diluted in assay buffer. Pyruvate and Succinate were added as substrates. Subsequently, Oligomycin, carbonylcyanide-3-chlorophenylhydra-zone (CCCP) and Potassium Cyanide (KCN) were added and the Oxygen Consumption Rate (OCR) was measured at different timepoints. Shown graphs are representatives of three repetitions. Each experiment was conducted in six independent wells and the mean ± SEM is shown.

(B) Mitochondria were isolated from Brain, Liver, Heart and Muscle and adjusted to equal amounts. Complex I was bound on a specific assay plate (Abcam) and substrates were added. NADH oxidation was assessed indirectly by measuring the reduction of a colometric dye.

(C) Mitochondria were isolated from Brain, Liver, Heart and Muscle and adjusted to equal amounts. Complex IV was bound on a specific assay plate (Abcam) and substrates were added. Cytochrome c oxidation was assessed directly by measuring its colometric change due to its oxidation.

In both figures (B) and (C) the mean ± SEM of MT divided by the average of WT is shown (n = 3). The dashed line symbolizes the average of WT, set to 100%. WT, Wild Type; MT, COX14M19I.

3.3 Phenotyping of COX14M19I

3.3.1 The Mitochondrial Membrane in Hepatocytes Displayed a Disrupted, Discontinuous Structure

The structure of mitochondrial membranes ensures efficient energy conversion by the OXPHOS system. Therefore, the stability and integrity of both mitochondrial membranes and cristae formation are of paramount importance to cells. To investigate the structure of COX14M19I mitochondria, hepatocytes were isolated and transmission electron microscopy was carried out in collaboration with Stefan Jakobs (Clinic of Neurology).

Electron micrographs of mitochondria in COX14M19I hepatocytes showed structural damages (Figure 3.4). The OMM appeared discontinuous and interrupted, showing pore-like structures. In addition, the order and their regularity of the cristae structure was abolished.

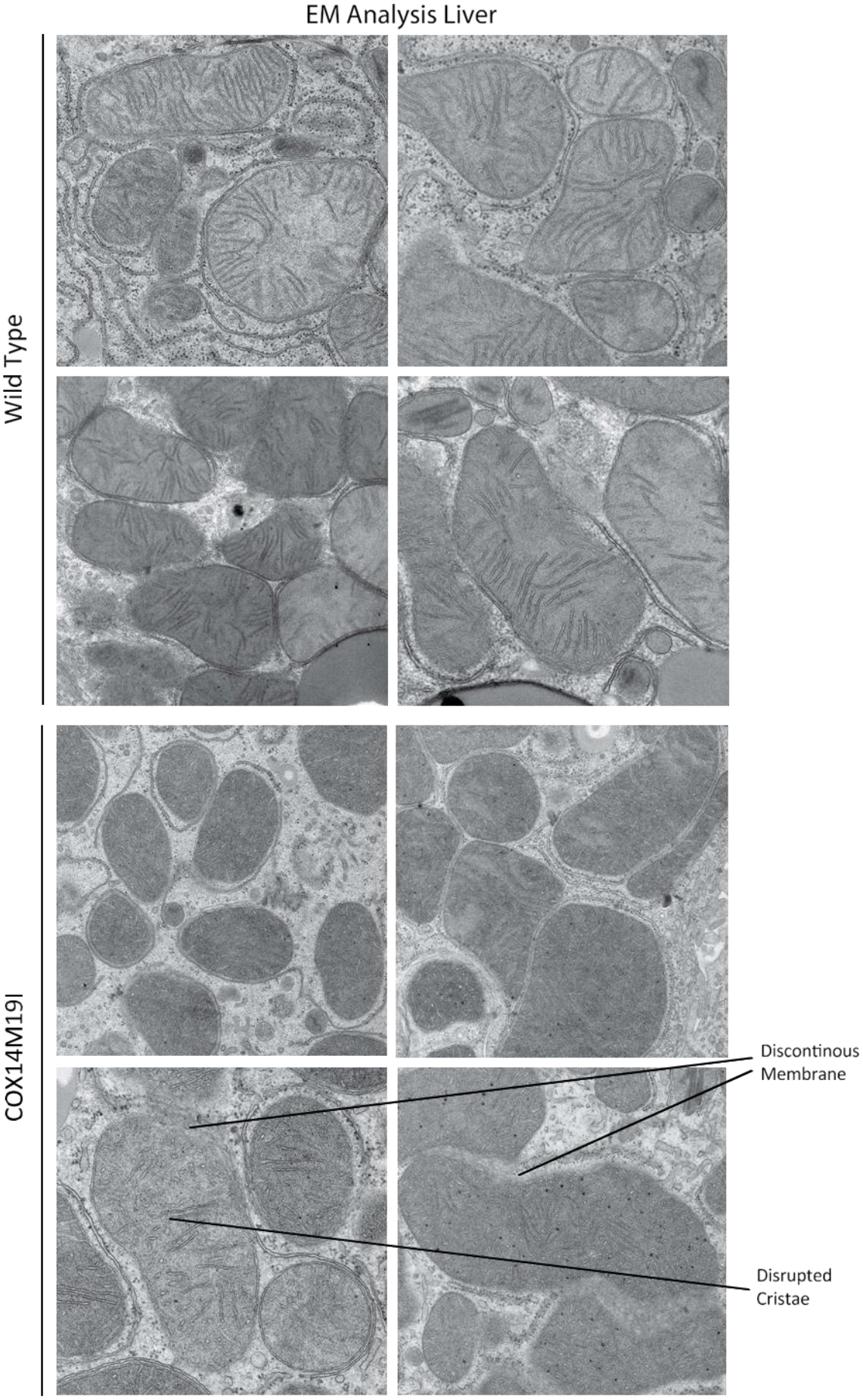
EM Analysis Liver
Wild Type
COX14M19I
Discontinous
Membrane
Disrupted
Cristae

Figure 3.4: EM Analysis showed disrupted and discontinuous mitochondrial membranes in hepatocytes.

Hepatocytes were isolated using Percoll gradient centrifugation. Electron microscopy was carried out in collaboration with Stefan Jakobs (Clinic of Neurology).

An important mechanism to remove aging or degenerated cells and thus protect the body from pathological processes is the targeted killing of diseased cells, referred to as apoptosis. Apoptosis can be triggered by extrinsic or intrinsic factors (Elmore 2007). During the apoptosis mitochondria form pores and the EM images resembled to such a process. Therefore, levels of apoptotic proteins in liver were assessed by SDS-PAGE and immunoblotting. However, no increase in apoptotic proteins was apparent in COX14M19I compared to wild type (Figure A.4). In addition, Mitofusin 1 and Dynamin-1-like protein 1 (Drp1), key factors in mitochondrial fission and fusion, showed equal levels in liver of COX14M19I and wild type (data not shown).

Thus, no indication for apoptosis was observed.

3.3.2 Transcriptome Analysis Revealed Tissue-specific Upregulation of Antiviral Immune Response Pathways

To obtain an accurate picture of cellular signaling in different organs, mRNA was isolated from four different tissues – brain, liver, heart and muscle – and RNA sequencing was performed in cooperation with the Next-Generation Sequencing (NGS) - Service facility for integrative genomics Universitätsmedizin Göttingen (UMG).

Pathway analysis revealed, that the majority of the 50 highest expressed genes in COX14M19I compared to wild type were factors involved in antiviral, interferon signaling. The antiviral immune response was upregulated in all four tissues with highest upregulation in liver (Figure 3.5). Most of these genes were especially associated with type I interferon signaling. Figures displaying data from the other organs can be found in the appendix (Figure A.5).

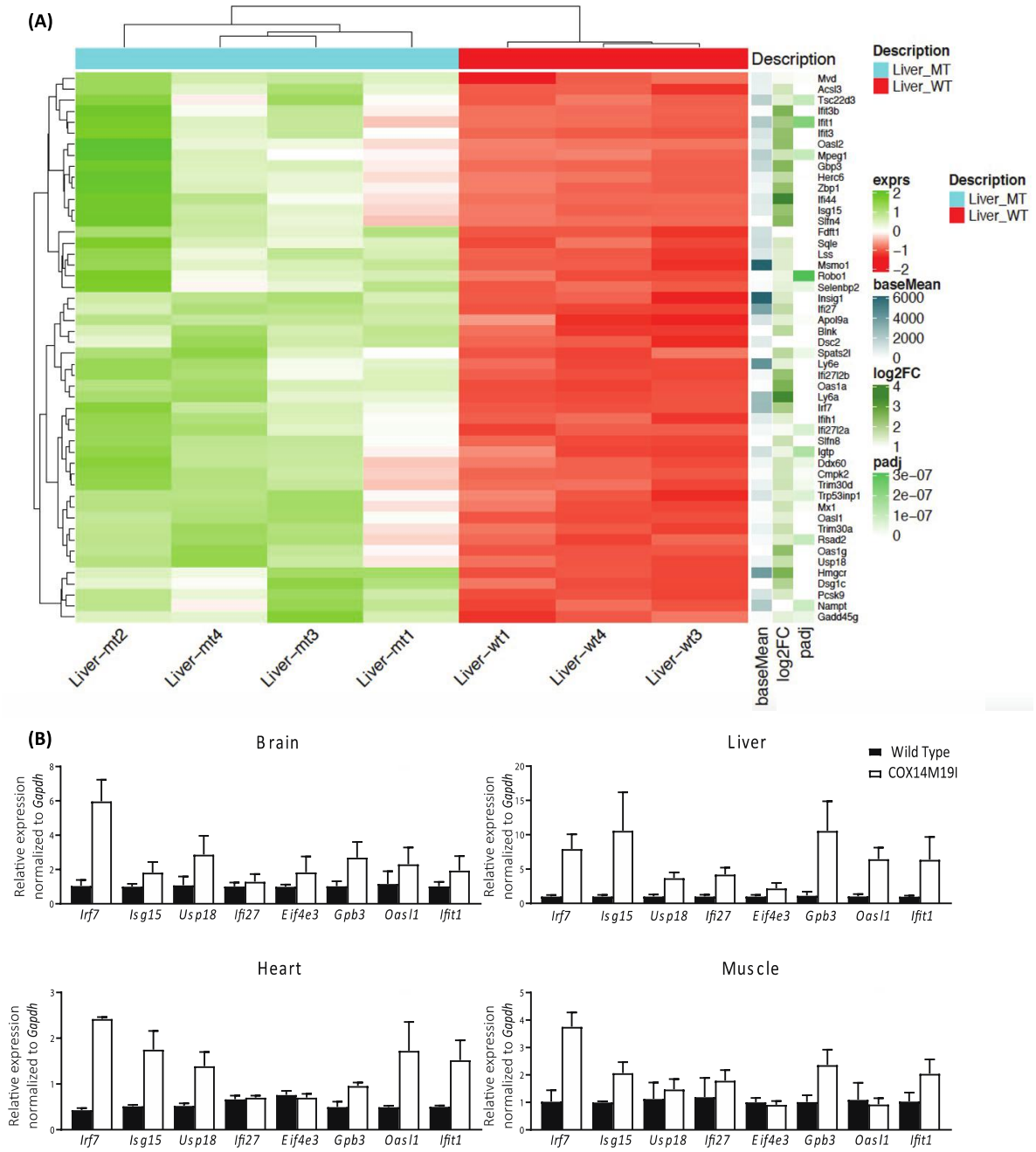

Figure 3.5: Transcriptome analysis revealed upregulation of interferon mediated antiviral immune response pathways.

(A) mRNA was isolated from liver and RNA sequencing was performed (n = 4). Differences in expression levels are shown in log2fold scale. WT, Wild Type; MT, COX14M19I.

(B) mRNA was isolated from the different tissues and specific primers were designed for selected gene sequences. A quantitative PCR was performed and amplification of Gapdh was used to calculate the relative gene expression. The mean ± SEM of the differences in gene expression are shown in fold change (n=4).

Since the magnitude of induction of interferon response associated genes varied in the four different tissues, the expression of the referring genes was compared in the different tissues by quantitative PCR. Interferon Regulatory Factor 7 (*Irf7*), a key factor in type I interferon

induction expression (Ning et al. 2011), was upregulated in COX14M19I (Figure 3.5 (B)). The quantitative PCR showed that *Irf7* was expressed on average eightfold more in liver of COX14M19I than in wild type. In the other organs - brain (sixfold increase), muscle (fourfold increase), and heart (five-and a half fold increase) - *Irf7* expression was also significantly increased. However, compared to liver, these organs showed lower expression of *Irf7*.

Type I interferons induce transcription of so-called interferon stimulated genes. Many of them (for example *Ifit1*, *Ifit3*, *Ifi44*) showed high expression in COX14M19I, especially in liver (Figure 3.5 (B)). Some of the interferon induced genes are key factors in antiviral immune mechanisms, such as 2'-5'-oligoadenylate synthetase-like protein 1 (*Oasl1*). The Oasl protein family are antiviral immune response effector proteins that cause degradation of viral genomic material (Eskildsen et al. 2002). *Oasl1* was expressed significantly higher in the COX14M19I liver (sixfold), Brain (twofold), Heart (three and a half fold). In muscle, expression of *Oasl1* was equal in wild type and COX14M19I (Figure 3.5 (B)).

In addition to inducers, also inhibitors of the interferon pathway were significantly more expressed in COX14M19I. This indicated innate regulation of the interferon response (Figure 3.5 (B)). Ubiquitin specific peptidase 18 (*Usp18*) was significantly upregulated in liver (three and a half fold), brain (two and a half fold) and heart (two and a half fold). Of special interest was also the induction of interferon type I induced gene of Interferon-stimulated gene 15 (*Isg15*), which was expressed significantly higher in liver (tenfold), brain (twofold), heart (three and a half fold) and muscle (twofold) (Figure 3.5 (B)). Isg15 is considered another key factor in antiviral immune response, having multiple functions by interaction with the protein Usp18 (Chen et al. 2011).

In summary, both, factors inducing as well as being induced by mainly interferon type I, were significantly upregulated to different extends in different tissues, with highest expression in liver.

3.3.3 Interferon signaling in COX14M19I

Antiviral signaling is mediated via interferons, which can be distinguished into type I and type II interferons (Lee and Ashkar 2018). Type I interferons include interferon alpha and beta,

which are secreted primarily by (tissue-derived) monocytes/macrophages and virus-infected cells. They mediate intracellular antiviral immune defense and are regulated by interleukin 10 (IL-10) (Ng et al. 2013). The most important type II interferon is interferon gamma, which is stimulated by interleukin 12 and primarily activates cytotoxic T cells (Gill et al. 2011; Pegram et al. 2011). Both, interferons type I and II, bind to specific extracellular interferon receptors (Lee and Ashkar 2018).

To measure serum values of interferons and other cytokines, blood was drawn from six COX14M19I mice immediately after their death and serum was collected. Serum cytokine levels were measured and compared to six wild type samples using bead adsorption flow cytometry. Increased serum concentrations were found in COX14M19I for interferons alpha and beta. In contrast, no differences were seen in interferon gamma levels, indicating an activation of type I but not type II interferon signaling (Figure 3.6 (C)).

While analysis of other cytokines, such as interleukin 1β, interleukin 12, and interleukin 6 revealed no differences (Figure A.7), the levels of RANTES (or CCL5), monocyte chemoattractant protein-1 (MCP1 or CCL2) and interleukin 10 were found to be strongly elevated in COX14M19I (Figure 3.6 (C)).

Type I interferon receptor activation by extracellular, circulating interferons is mediated intracellularly primarily by signal transducer and activator of transcription 1 (Stat1). Stat1 forms different protein structures, such as homodimers, heterodimers in interaction with Stat2 and also Irf9, referred to as the ISGF3 complex (Platanitis et al. 2019). After interferon receptor activation, the complexes translocate into the nucleus and leads to the induction of interferon-stimulated genes (ISGs), in particular factor Irf7 (Génin et al. 2003).

In the transcriptomic analysis, *Stat1*, *Irf9* and *Stat2* were shown to be slightly increased in all tissues tested of the COX14M19I mice. *Stat1* was in particular higher expressed than the others in the in liver (Figure 3.5 (A)). Since the results indicated that liver was most affected by interferon signaling, SDS-PAGE and immunoblotting was performed with liver tissue samples and Vdac signals were used to standardize samples for quantification to assess the levels of the interferon receptor signal transducing factors. Protein amounts of Stat1 and Stat2 showed significant increase in COX14M19I (Figure 3.6 (B), Figure A.6). Both, Stat1 and Stat2 showed a double banded signal, of which the upper fraction was especially enriched in COX14M19I (Figure 3.6 (B), Figure A.6). This indicated that the proteins, particularly in COX14M19I, were

present in the alpha isoform, which was shown to be specifically enriched due to interferon alpha activation.

All in all, the results suggest that a cytokine-mediated interferon type I immune response, causing the activation of Stat1 and Stat2, is present in COX14M19I.

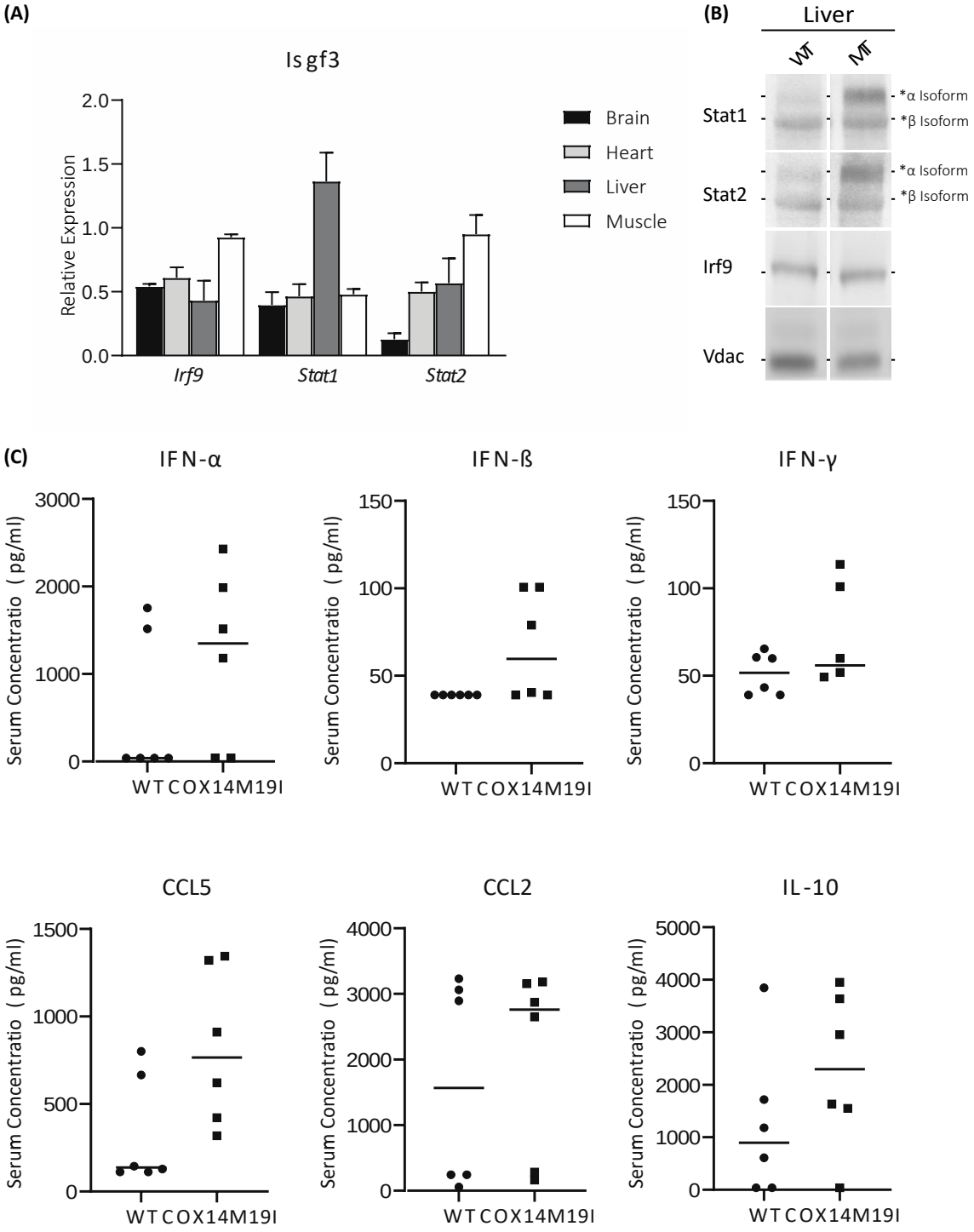

Figure 3.6: Antiviral Signaling in COX14M19I.

(A) mRNA was isolated from brain, liver, heart and muscle and RNA sequencing was performed (n = 4). Differences in expression levels are shown in log2fold scale.

(B) SDS-PAGE and immunoblotting was conducted to address the protein levels of Stat1, Stat2 and Irf9.

(C) Blood was drawn from six COX14M19I and six WTs and serum was collected. Cytokine, chemokine and interferon levels were measured by flow cytometry using LEGENDplex™ Mouse Anti-Virus Response Panel (n = 6). WT, Wild Type; MT, COX14M19I; Stat, Signal transducer and activator of transcription; Irf, Interferon regulating factor; IFN, Interferon; CCL5, CC- chemokine ligand 5; CCl2, CC- chemokine ligand 2; IL-10, Interleukin 10.

3.3.4 The Immune Response in Liver

Since the afore mentioned results indicated increased interferon type I signaling in COX14M19I, further experiments aimed to investigate the immune response in liver and determine its trigger.

After recognition of viral material, interferon type I translation is induced by recruitment of the TANK-binding kinase 1 (Tbk1) as well as the Interferon Regulating factors 3 (Irf3) and 7 (Irf7) via phosphorylation (Fitzgerald et al. 2003; Sharma et al. 2003; Wu and Chen 2014). Phosphorylation of Irf3 and Irf7 causes their transport into the nucleus, where they interact with the interferon-sensitive response element (ISRE) on the DNA (Ning et al. 2011; Sun et al. 2013; Zevini et al. 2017; Zhang et al. 2019). SDS-PAGE and immunoblotting were used to assess the abundance of phosphorylated interferon regulatory factors (IRFs) and Tbk1 in liver. Quantitative analysis of protein levels showed significantly increased protein levels of Irf7 in COX14M19I consistent with the transcriptome analysis. No changes in the phosphorylation status were observed for pIrf7 (Figure 3.7 (A), Figure A.7).

The amount of unphosphorylated Irf3 was similar in wild type and COX14M19I. In contrast, less phosphorylated Irf3 was found in COX14M19I than in wild type.

Levels of Tbk1 and phosphorylated Tbk1 did not differ in COX14M19I from wild type (Figure 3.7 (A), Figure A.7).

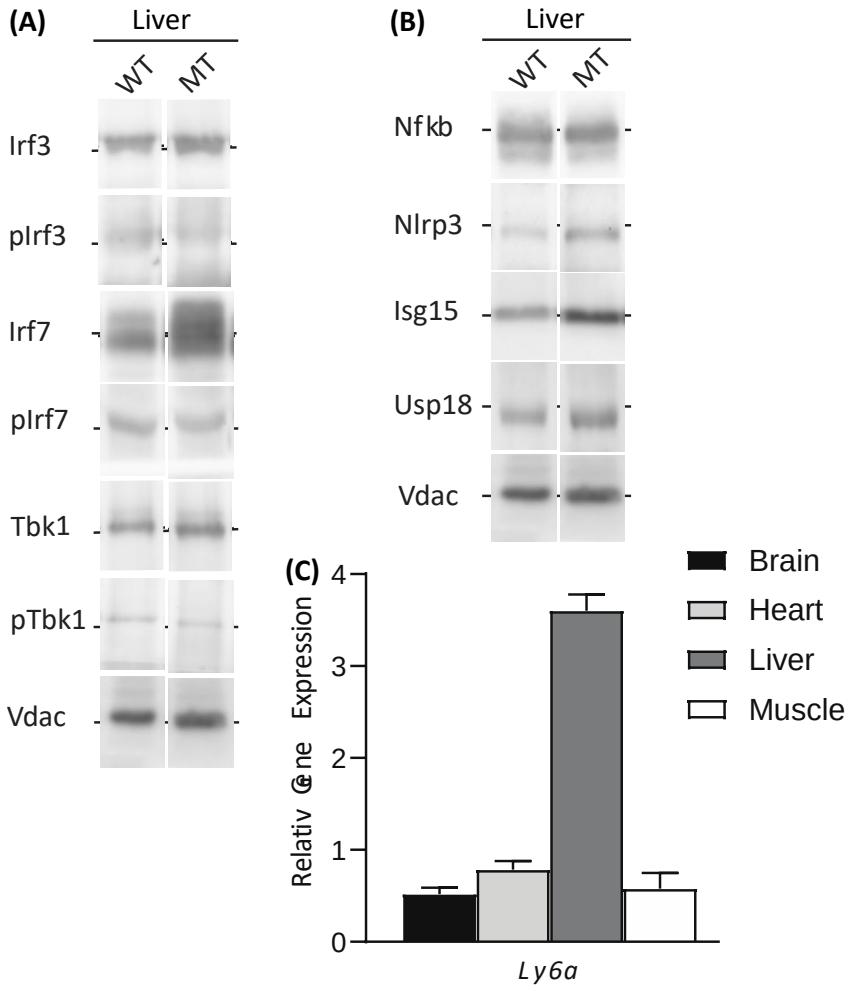

Figure 3.7: Inflammatory Response in Liver.

(A) and **(B)** SDS-PAGE and immunodetection of liver tissue lysates from COX14M19I and WT mice was carried out to address protein levels of proinflammatory factors in liver.

(C) mRNA was isolated from brain, liver, heart and muscle and RNA sequencing was performed (n = 4). Differences in expression levels are shown in log2fold scale. WT, Wild Type; MT, COX14M19I; Irf, Interferon Regulating Factor; Tbk, TANK-binding kinase; Nfkb, Nuclear factor 'kappa-light-chain-enhancer' of activated B-cells; Nlrp3, NLR family pyrin domain containing 3; Ly6a, Lymphocyte antigen 6a

To further investigate the inflammatory effects in the liver, levels of key players involved in inflammatory processes were assessed by SDS-PAGE and immunoblotting. Nuclear factor 'kappa-light-chain-enhancer' of activated B-cells (Nfkb), a central proinflammatory transcription factor, showed equal levels in Cox14M19I and wild type (Liu et al. 2017) (Figure 3.1 (B)). Also, NLR family pyrin domain containing 3 (Nlrp3), a core component of the inflammasome, did not show different signals in COX14M19I compared to wild type (Swanson et al., 2019) (Figure 3.7(B)).

Since transcriptome analysis indicated induction of immune active factors *Usp18* and *Isg15,* their protein levels were assessed by SDS-PAGE and immunoblotting, too. Both, Isg15 and Usp18 showed higher protein levels in COX14M19I (Figure 3.7 (B), Figure A.**8**). The analysis also showed transcription of *Ly6a* gene to be significantly increased in the Cox14M19I liver (Figure 3.7 (C)). Ly6a (also referred to as SCA-1) is a surface protein and was reported to be expressed especially by inflammatory tissues and in tumorigenesis (Lee et al. 2013a; Morcos et al. 2017; Upadhyay 2019).

3.4 Triggers of the Inflammatory Response

3.4.1 Mitochondrial Nucleic Acids accumulated extra mitochondrially in COX14M19I

Since the mice were kept under sterile conditions, viral infection could be excluded as a trigger of the antiviral immune response. Thus, it was important to investigate possible triggers of the immune response. Of special interest were triggers, that could be caused by mitochondrial dysfunction. Physiologically, interferons are induced after recognition of intracellular viral foreign material like cytosolic viral nucleic acids. Various studies have shown that mitochondrial nucleic acids also trigger an interferon response. This happens when mitochondrial nucleic acids get released from mitochondria. In the cytosol they are recognized by specific receptors as mitochondrial damage associated molecular patterns (mtDAMPs), thus mimicking viral genomic material (Patrushev et al. 2004; West et al. 2015; Huang et al. 2020).

Hence, mitochondria were isolated from the different tissues and the extramitochondrial fractions obtained during the isolation process were saved. These were then used for mtDNA isolations. Amounts of mitochondrial DNA were estimated by quantitative PCR. Significantly more extramitochondrial mtDNA segments were amplified in COX14M19I liver than in wild type. In contrast, brains of the mutant mice showed lesser levels of these extramitochondrial segments (Figure 3.8 (A)). No difference was observed in the heart and muscle samples.

To confirm these findings, extramitochondrial mtDNA levels were estimated by a regular PCR. After separation of the PCR products using an agarose gel, the amount of amplified mtDNA was estimated by digital image analysis (Figure A.**9**). Upon quantification, it was observed that significantly more extramitochondrial mtDNA was amplified in liver of COX14M19I than in wild type. However, in heart, brain and muscle, equal amounts of

mtDNA were detected extramitochondrially in wild-type and COX14M19I (Figure 3.8 (B)). Furthermore, DNA fragments were analyzed by DNA sequencing. Thus, the amplification of the fragments was confirmed to be from mtDNA and not from nuclear mitochondrial pseudogenes (NUMTs) (data not shown).

Moreover, levels of mtDNA in isolated liver mitochondria was also determined. A quantitative PCR was used to determine the amplification of DNA using the same four primer-pairs used in the experiments before. The amount of mtDNA fragments amplified by the different primers were significantly decreased in mitochondria of COX14M19I hepatocytes (Figure 3.8 (C)). A possible explanation could be that the mtDNA was released from the mitochondria in hepatocytes of COX14M19I.

Furthermore, mtDNA was isolated from mice serum using the QIAamp DNA isolation kit, to address the levels of circulating free mtDNA in the blood of COX14M19I. However, equal levels of mtDNA were amplified by qPCR in COX14M19I and wild type (data not shown).

In addition to mtDNA, mitochondrial RNA (mtRNA) was also reported to potentially trigger an interferon response (Dhir et al. 2018). Therefore, RNA was also isolated from the extramitochondrial fractions of liver samples and subjected to DNase I treatments to remove any DNA fragments. The levels of mtRNAs were compared between wild type and COX14M19I by quantitative PCR. Relative amounts of mtRNAs in the extramitochondrial fractions was calculated in comparison to the average wild type levels. The cytosolic ribosomal subunit RNA, 18S was used as a loading control. Significantly more mtRNA was detected extramitochondrially in COX14M19I liver. Similar to the detection of mitochondrial DNA, the mtRNA concentration in the extramitochondrial fraction of COX14M19I was increased three- to fourfold compared to wild type (Figure 3.8 (D)).

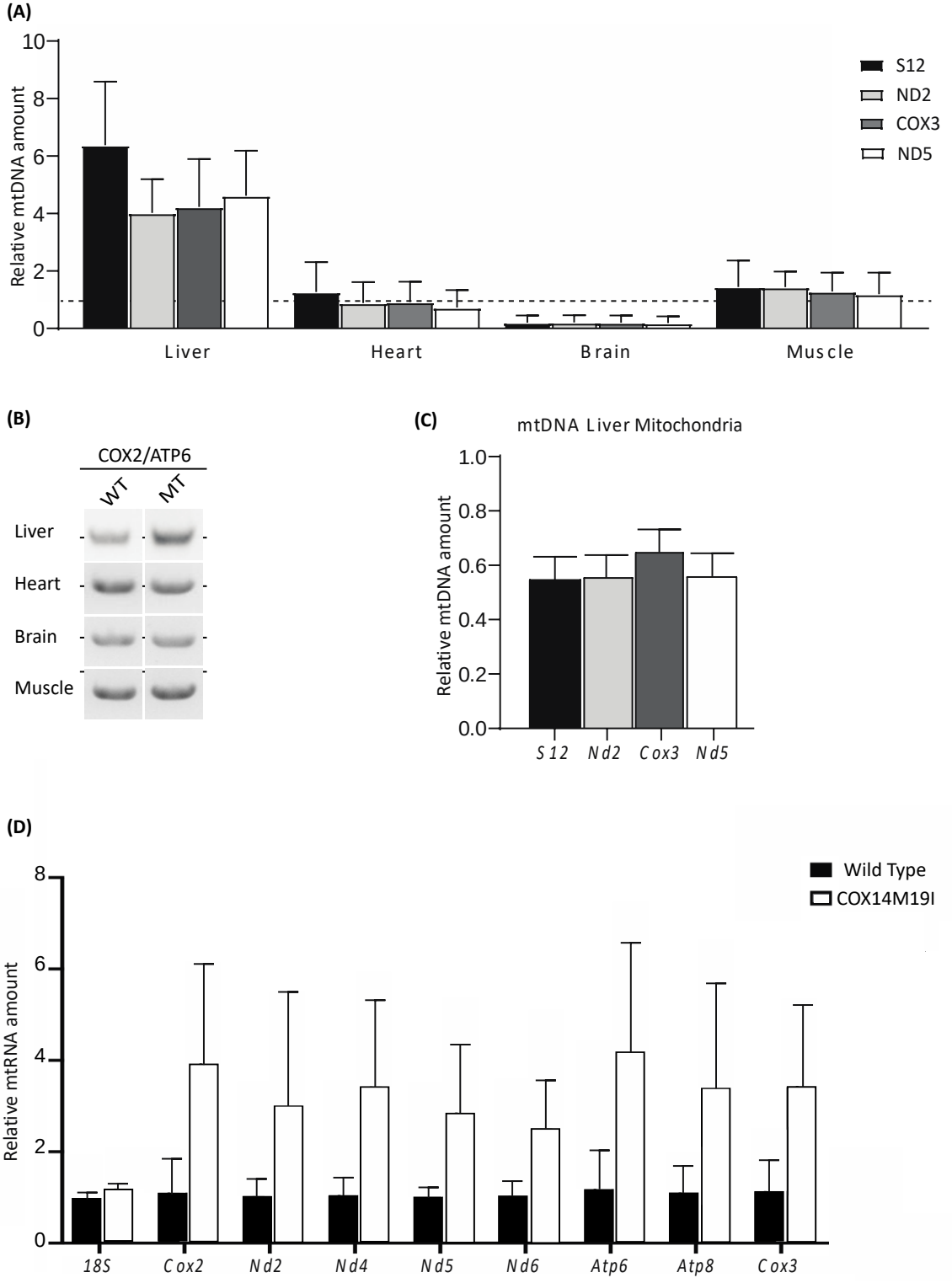

Figure 3.8: Enriched Extramitochondrial Nucleic Acids in COX14M19I Liver.

The extramitochondrial fraction was separated from mitochondria in the different tissues and nucleic acids were isolated from this extramitochondrial fraction using QIAamp DNA isolation kit and trizol purification for RNA. WT, Wild Type; MT, COX14M19I; mtDNA, mitochondrial DNA.

(A) The amount of mitochondrial DNA in the cytosol was measured by quantitative PCR. The average wild-type amplification of the plasmids was calculated and used to assess the difference from expression in COX14M19I. Shown is the mean ± SEM of the ratio of MT/average WT plasmids amplification (n=3). The dashed line symbolizes the average WT, set to 1.

(B) Amplification products from a PCR, using COX2/ATP6 primer pairs, were loaded onto a 1% agarose gel and band intensities from the mutants and the wild type samples were quantified. (n=3)

(C) MtDNA was isolated from the mitochondria of wild type and COX14M19I liver samples. A quantitative PCR was used to determine the amplification of S12, ND2, COX3 and ND5. The average plasmid amplification in wild type was used to calculate the relative expression in COX14M19I. Shown is the mean ± SEM of the ratio of MT and WT plasmids amplification (n=3).

(D) MtRNA amounts from the extramitochondrial fractions was estimated by qPCR. The average wild-type amplification of the plasmids was calculated and used to assess the differences of expression in COX14M19I. Shown is the mean ± SEM of the ratio of MT and WT plasmids amplification (n=3).

3.4.2 Analysis of possible Pattern Recognition Receptors (PRRs) in COX14M19I Liver

For the immune system to respond appropriately and specifically against a viral infection, the pathogen's load and identity must be determined first. This is mediated by pattern recognition receptors (PRRs), which recognize a variety of different properties of potential pathogens, such as foreign nucleic acids. Thus, PRRs form the interface between infection and an immune response.

It was recently shown that these PRRs could be triggered by mitochondrial nucleic acids (West and Shadel 2017). Since mitochondrial nucleic acids have been found to accumulate extramitochondrially in COX14M19I liver, further analyses aimed to identify potential PRRs in COX14M19I liver to elucidate the trigger of the interferon response.

Of particular note is the enzyme cyclic GMP-AMP synthase (cGAS), which recognizes double-stranded DNA and was reported to also recognize cytosolic mtDNA (Maekawa et al. 2019; Huang et al. 2020). In addition, Z-DNA-Binding-Protein 1 (ZBP1 or DLM1, DAI) has been reported to recognize foreign DNA and potentially mtDNA (Kuriakose and Kanneganti, 2018; T. Zhang et al., 2020). Both PRRs activate the Stimulator of interferon genes (Sting), which finally induces an interferon response via activation of interferon transcription factors Tbk1 and Irf3 (Zhang et al. 2019).

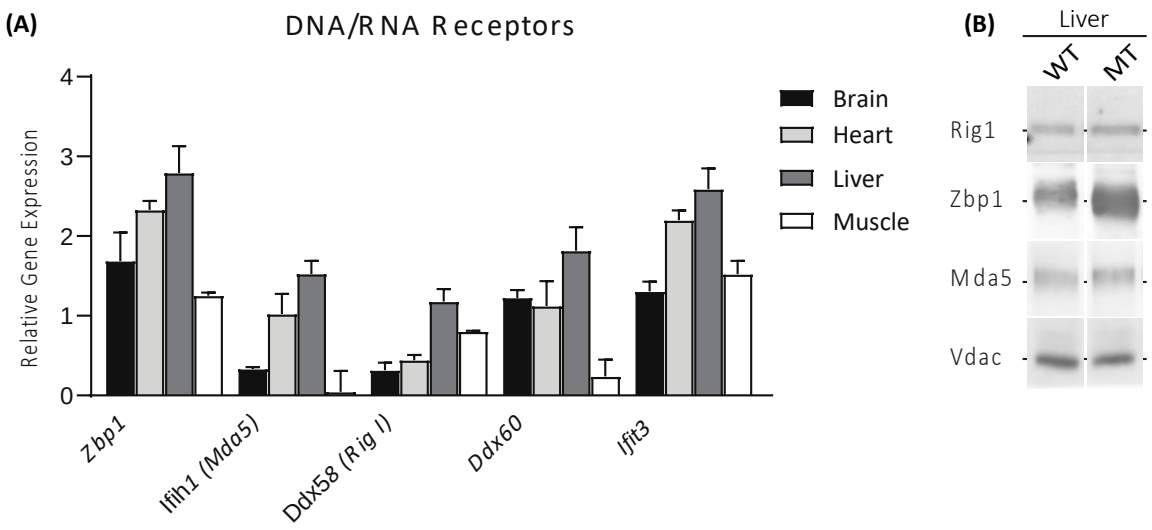

Figure 3.9: Cytosolic DNA and RNA Sensors Expression in COX14M19I.

(A) RNA was isolated from brain, liver, heart and muscle and RNA sequencing was performed. The log2fold change of the gene expression in COX14M19I is shown in comparison to the WT gene expression (n=4).

(B) SDS-PAGE and immunoblotting was conducted to address the protein levels of PRRs in liver.

WT, Wild Type; *Zpb1*, Z-DNA Binding Protein 1; *cGas*, Cyclic GMP-AMP synthase; *Ifih1*, Interferon Induced with Helicase C Domain 1; *Mda5*, Melanoma Differentiation Associated Protein 5; *Ddx58*, DExD/H-Box Helicase 58; *Rig I*, Retinoic Acid Inducible Gene I; *Ddx60*, DExD/H-Box Helicase 60; *Ifit3*, Interferon-induced protein with tetratricopeptide repeats 3.

Zbp1 as well as *Mlkl* (data not shown), a factor mediating the *Zbp1* activation pathway, were clearly induced in liver and heart of COX14M19I (Figure 3.9 (B)).

Prominent RNA recognition receptors in the cell are Melanoma Differentiation Associated Protein 5 (Mda5), which is encoded by the gene *Ifih1*, and Retinoic Acid Inducible Gene 1 (Rig I), encoded by the gene *Ddx58* (Refolo et al. 2020). This mechanism is regulated by various factors. Among others, the helicase *Ddx60*, but also factor *Ifit3*, lead in different ways to an enhancement of the described signaling pathway (Oshiumi et al. 2015; Johnson et al. 2018). Both genes of dsRNA receptors, Mda5 (*Ifih1*) and Rig I (*Ddx58*), showed slight upregulation in liver of COX14M19I (*Ifih1* 1.42 log2fold, *Ddx58* 1.11 log2fold). Moreover, stimulation factors *Ifit3* and *Ddx60* were significantly induced, especially in liver of COX14M19I (*Ifit3* 2.35 log2fold, *Ddx60* 1.63 log2fold) (Figure 3.9 (A)).

As various PRRs showed significant induction especially in liver, protein levels of the mentioned pathways were measured by SDS-PAGE and immunoblotting in liver. Quantitative

analysis of PRRs showed a significant increase of Zbp1 in COX14M19I (Figure 3.9 (B), Figure A.8 (B)). In contrast, Mda5 and Rig1 showed equal expression (Figure 3.9 (B), Figure A.8). In liver, the protein Sting could not be detected in wild type or COX14M19I by immunoblotting (data not shown).

In summary, although several PRRs and other downstream activators showed clear gene induction, only the protein levels of Zpb1 were significantly increased.

3.5 Clinical Phenotype of COX14M19I

The aim of this study is to investigate the biochemical background of OXPHOS dysfunction and to place it into a clinical context. For this purpose, we teamed up with the Czech Center for Phenogenomics to study the mice using general diagnostic functional tests to investigate the resulting phenotype, i.e., the effects of OXPHOS dysfunction on organ functionality. Eight COX14M19I mice were compared with a cohort of eight wild type mice of the same mouse line and with over 1000 animals from a C57Bl/6NCrl control group to obtain valid control values. A distinction was also made according to sex. Abnormal blood values were controlled in six animals each by the routine laboratory of the University Medical Center Göttingen (UMG).

3.5.1 Cholesterol Metabolism

The steroid cholesterol forms an important membrane component that increases the fluidity and stability of cell membranes. It is absorbed through food, but can also be synthesized by the cells themselves from acetyl CoA. Cholesterol levels are mainly regulated by the liver, which excretes cholesterol from extrahepatic tissues via transport by high density lipoproteins (HDL) through bile acids.

Analysis of blood parameters in the COX14M19I mice revealed that cholesterol and lipoprotein HDL levels in particular were elevated in mutants compared to controls (Figure 3.10 (A)). However, serum triglycerides levels were unaffected in both wild type and COX14M19I mice (Figure A.**10**). Elevated cholesterol levels appeared to be due to increased production of cholesterol, as transcriptome analysis revealed a strong induction of beta-HMG-

CoA reductase (*Hmgcr*), in liver of COX14M19I (Figure 3.10 (B)). Beta-HMG-CoA reductase is considered a key enzyme for cholesterol synthesis, which is localized predominantly in liver. In addition to *Hmgcr*, *Lanosterol Synthase* (*Lss*), *Squalene Monooxygenase* (*Sqle*), *elongation of long-chain fatty acids family member 6* (*Elovl6*), *Isopentenyl-Diphosphate Delta Isomerase 1* (*Idi1*), *Farnesyl-diphosphate farnesyltransferase 1* (*Fdft1*), *Mevalonate Diphosphate Decarboxylase* (*Mvd*), *Lathosterol oxidase* (*Sc5dl*), which are key enzymes in cholesterol synthesis pathway (Belter et al. 2011) where significantly induced especially in liver of COX14M19I (data not shown).

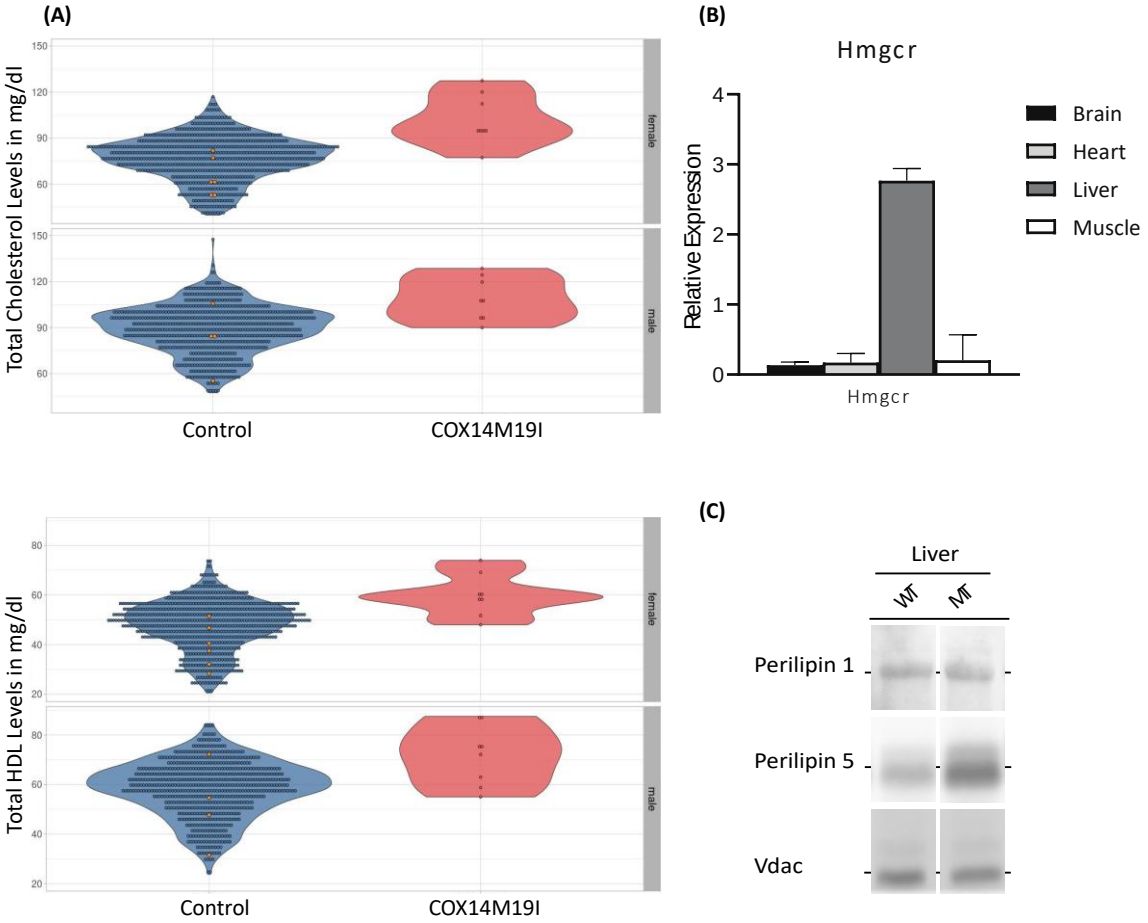

Figure 3.10: Elevated Cholesterol Levels Indicated Increased Cholesterol Metabolism in COX14M19I.

(A) Blood values from 16 (8 male + 8 female) COX14M19I mice were compared to a control cohort of 10 (6 male + 4 female) wild types and a historical population cohort of over 1000 animals of the C57Bl/6NCrl. Prior data courtesy: Czech Center for Phenogenomics (CCP), Prague.

(B) RNA was isolated from liver tissue samples and RNA Sequencing was performed. The expression of beta HMG-CoA Reductase (Hmgcr) is shown in log2fold scale, compared to wild type expression (n=4).

(C) Liver tissue lysates were separated by SDS-PAGE and immunoblotting was performed.

WT, Wild Type; MT, COX14M19I.

To further investigate the change of lipid metabolism in liver, levels of Perilipin 1 and 5 were determined by SDS-PAGE and immunoblotting. As central factors for lipid storage, they serve to form lipid droplets and thus regulate lipid metabolism depending on energy requirements. While Perilipin 1 did not show significant differences, amounts of Perilipin 5 were significantly increased in COX14M19I liver (Figure 3.10 (C)).

3.5.2 Liver in COX14M19I Developed NASH-like Phenotype

Biochemical analysis indicated that liver was most affected by OXPHOS dysfunction and that secondary effects resulted in interferon signaling as well as increased cholesterol metabolism. Histopathological analysis and control of blood levels aimed to further investigate liver function and phenotype in COX14M19I.

Analysis of serum samples showed no evidence of a protein synthesis disorder and there was no evidence of cholestasis with normal bilirubin levels (data not shown). Aminotransferases levels - Alanine Aminotransferase (ALT) and Aspartate Aminotransferase (AST) - were significantly elevated, indicating hepatocellular damage (Figure 3.11 (A)).

Histopathological analysis of six young (14 weeks) and three old (over one year) COX14M19I mice was performed in comparison with three wild types in each group. Young COX14M19I mice showed accumulation of cytoplasmic lipid droplets in hepatocytes in contrast to wild type. There were no signs of inflammatory processes or structural remodeling (Figure 3.11 (B)). This phenotype increased with age. In particular, COX14M19I livers showed clear signs of cytoplasmic fatty degeneration. This was particularly pronounced in the intermediate zones. Although wild type also showed increased accumulation of lipids with aging, in COX14M19I, the lipid areas were more pronounced and showed a more diffuse distribution (Figure 3.11 (B)). In addition to heavy lipid accumulation, old COX14M19I showed signs of inflammation with reactive lymphocyte infiltration. Although isolated lymphocyte infiltrates were also evident in the aged wild types, they were more pronounced in COX14M19I. This infiltration of lymphocytes was predominantly evident in the portal tract. This finding resembled a light form of the human disease of Non-alcoholic steatohepatitis (NASH) (Figure 3.11 (B)). There was no evidence of fibrosis, nor signs of tumorigenesis in COX14M19I.

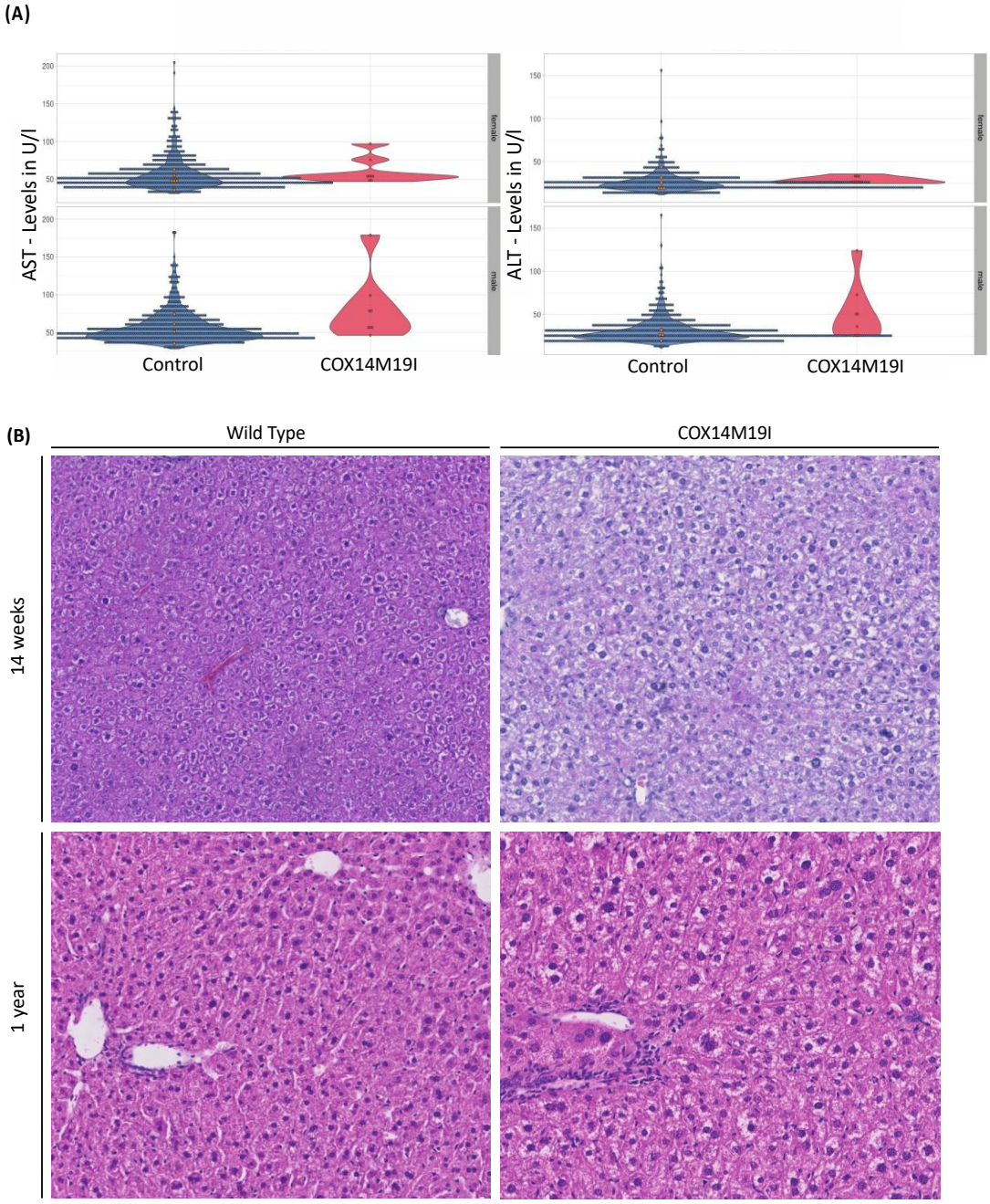

Figure 3.11: COX14M19I developed hepatic steatosis and inflammatory characteristics.

(A) Blood values from 16 (8 male + 8 female) COX14M19I mice were compared to a control cohort of 10 (6 male + 4 female) wild types and a historical population cohort of over 1000 animals of the C57Bl/6NCrl. Prior data courtesy: Czech Center for Phenogenomics (CCP), Prague.

(B) HE images of the liver were analyzed by the help of Prof. Ströbel (UMG). A group of young 14 weeks old mice (three wild types and six COX14M19I) was compared to a group of 1 year old mice (n = 3) in order to analyze the age dependent development of the phenotype.

3.5.3 Interpretations from the previous phenotyping screening data of COX14M19I mice

The present study focused particularly on pathologies in liver. In the following, a brief description of other organ systems aims to describe the impact of mitochondrial dysfunction on their functionality.

Prior to the start of this study, the Rehling laboratory had teamed up with Czech Center for Phenogenomics (CCP), Prague and subjected the COX14M19I mice to a complete phenotyping screen as per International Mouse Phenotyping Consortium guidelines. Since the phenotyping data allowed systemic interpretation of the results from this study, relevant results are briefly discussed in the following sections. Firstly, there was a general developmental abnormality evident in impaired growth and weight gain of COX14M19I in the first 15 weeks of life (Figure 3.12 (A))

Histopathologic analysis of heart revealed vacuolization and disintegrated cardiomyocytes, which is known as vacuolar degeneration (Takemura et al. 2017). This phenotype was evident in all of the eleven examined 14 weeks old COX14M19I and none of the examined wild types. Thus, pictures indicated the development of a cardiomyopathy in all examined COX14M19I (Figure 3.12 (B)). However, echocardiography showed normal pump function and electrocardiogram (ECG) indicated regular excitation propagation (data not shown). Pulmonary function diagnostics, performed by intubating the mice and connecting them to a ventilation system, revealed the picture of a restrictive lung disease. Compliance as well as inspiratory capacity were significantly decreased (Figure A.11). However, histologic analysis of young and old mice (1year) did not reveal a correlating histopathologic phenotype (data not shown).

.

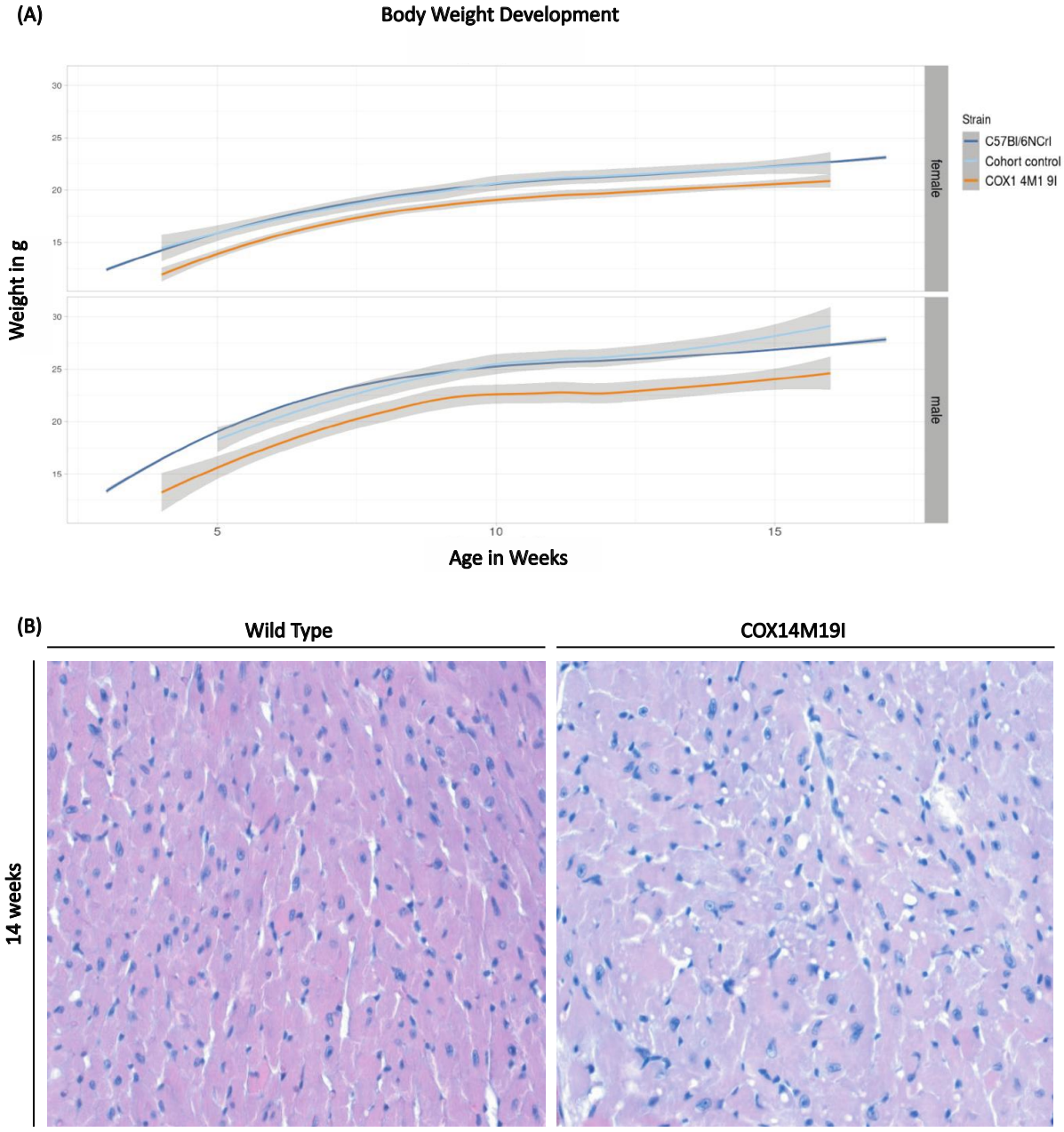

Figure 3.12: COX14M19I Phenotype.

(A) Weight from 16 COX14M19I were compared to a control cohort of 8 wild types and a population of over 1000 animals of the C57Bl/6NCrl. Prior data courtesy: Czech Center for Phenogenomics (CCP), Prague

(B) Histopathologic HE images of heart were analyzed by the help of Prof. Ströbel (UMG).

Central and peripheral nervous system functions did not appear to be affected. Neither neuromuscular function (tested by grip strength) nor central nervous processes (tested by auditory evoked potentials) showed pathological test results (data not shown).

Blood counts showed slightly elevated creatinine levels, elevated lipoproteins with elevated cholesterol, and elevated urea levels, with normal albumin levels (data not shown). Since also the kidneys of COX14M19I were significantly reduced in size, this in total could have indicated renal damage and a histopathological diagnosis was performed through the kind assistance of Dr. Hakroush (UMG). However, no structural abnormalities were detected (data not shown).

To further investigate the cellular immune response and cell distribution, the immunophenotype by FACS analysis of immune cells comparing 16 COX14M19I mice with ten wild types was performed. In addition to a normal total leukocyte count, the immunophenotype of COX14M19I showed a significant reduction in macrophages (Table A.1). Furthermore, the number of effector natural killer T (NKT)-cells was significantly decreased, whereas the number of resting NKT-cells was significantly increased (Table A.1). Furthermore, especially the CD11b negative natural killer (NK)-Cells (LY6C positive as well as LY6C negative) showed a strong, significant increase in the cell number (Table A.1). A detailed overview of the immunophenotype is added in the appendix (Table A.1).

4 Results: Chapter Two

4.1 Defective Cox1 Expression in Aging Mice Liver

In addition to studying the mutation of Cox14, this work also included a publication, studying mitochondrial adaptation processes during aging. The personal work performed included the investigation of OXPHOS complex and protein levels, mitochondrial physiological parameters, as well as the preparation and performance of the transcriptional analysis. The following section is intended to briefly summarize the conduct of the study.

4.1.1 Abstract

Mitochondrial defects are associated with aging processes and age-related diseases, including cardiovascular diseases, neurodegenerative diseases and cancer. In addition, some recent studies suggest mild mitochondrial dysfunctions appear to be associated with longer lifespans. In this context, liver tissue is considered to be largely resilient to aging and mitochondrial dysfunction. Yet, in recent years studies report dysregulation of mitochondrial function and nutrient sensing pathways in ageing livers. Therefore, we analyzed the effects of the aging process on mitochondrial gene expression in liver using wildtype C57BL/6N mice. In our analyses, we observed alteration in mitochondrial energy metabolism with age. To assess if defects in mitochondrial gene expression are linked to this decline, we applied a Nanopore sequencing based approach for mitochondrial transcriptomics. Our analyses show that a decrease of the *Cox1* transcript correlates with reduced respiratory complex IV activity in older mice livers.

4.1.2 Changes in Mitochondrial Membrane Potential During Ageing

Considering that hepatic cells are claimed to display to a certain extend resilience towards aging processes, we analyzed the correlation between different key parameters of

mitochondrial physiology and age in the livers of young and aged mice (12 week (12W) and 65 week (65W), respectively) (Figure 4.1 (A)). Livers excised from the 65W mice showed a pale appearance. During the mitochondrial isolation the older livers also displayed a higher degree of fat layer abundance. The mitochondrial respiratory chain establishes a proton gradient across the inner membrane that drives ATP production by the F_1F_o ATP Synthase.

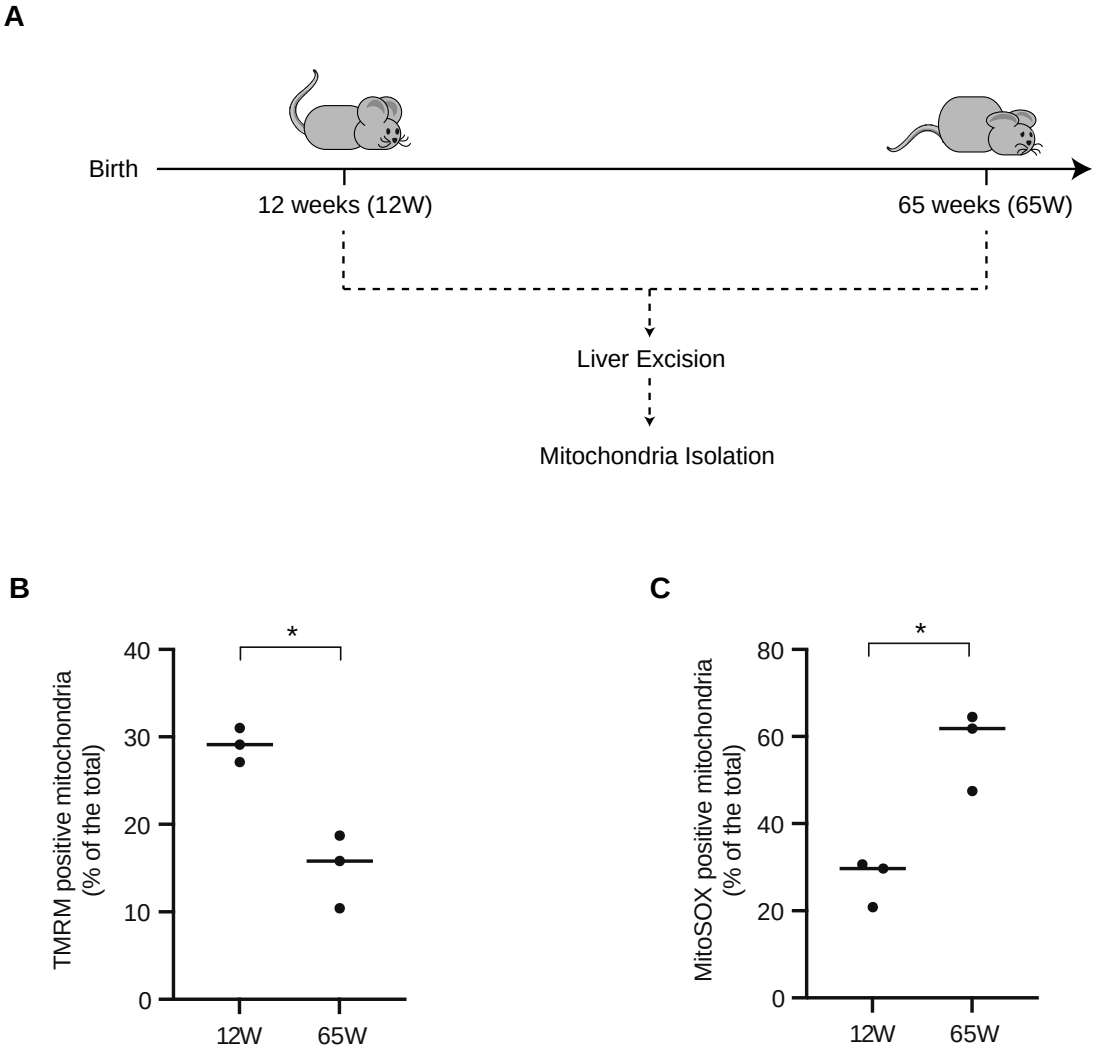

Figure 4.1: Aged mitochondria show a decrease in membrane potential and increased oxidative stress.

(A) Experimental overview of the experimental cohort of twelve-week-old female mice compared with a cohort of 65-year-old mice and the procedures conducted.

(B) Isolated mitochondria stained with TMRM to measure the mitochondrial membrane potential, **(**mean ± SEM, $p<0.05$, n=3).

(C) Isolated mitochondria stained with MitoSOX to measure the mitochondrial membrane potential (mean ± SEM**,** $p<0.05$, n=3).

To assess the mitochondrial membrane potential ($\Delta\psi$), the isolated mitochondria from both experimental cohorts were stained with the membrane potential sensitive dye TMRM (Tetramethylrhodamin-methylester-perchlorat). Applying the samples to flow cytometric analyses, we observed that the membrane potential was significantly reduced in the 65W mice as compared to that measured for the 12W old mice mitochondria (Figure 4.1 (B)). Similarly, when the isolated mitochondria were stained for superoxide production with fluorescent indicator MitoSOX, we found that superoxide levels were significantly increased in mitochondria from the 65W mice compared to that of the 12W old mice (Figure 4.1 (C)). Based on these observations, we concluded that a decrease in the mitochondrial health parameters were apparent with increasing age.

4.1.3 Mitochondrial Energy Metabolism Changes with Age

A reduction in the mitochondrial membrane potential with increased superoxide production are indicative of dysfunction of the respiratory chain and concomitantly the oxidative phosphorylation process. Therefore, we assessed mitochondrial oxygen consumption by real time respirometry to determine if a decline in oxidative phosphorylation was apparent with age. In the presence of non-limiting amounts of ADP and substrate (state 3) actively respiring mitochondria reach a maximal physiological respiration. We found that state 3 respiration was lower in 65W liver mitochondria as compared to those from 12W old mice (Figure 4.2 (A)). The addition of oligomycin and CCCP to measure the uncoupled maximal respiration showed a similar difference. When we quantified averages obtained from three measurements in each case, we observed that the rate of oxygen consumption was significantly reduced under all conditions (Figure 4.2 (B)).

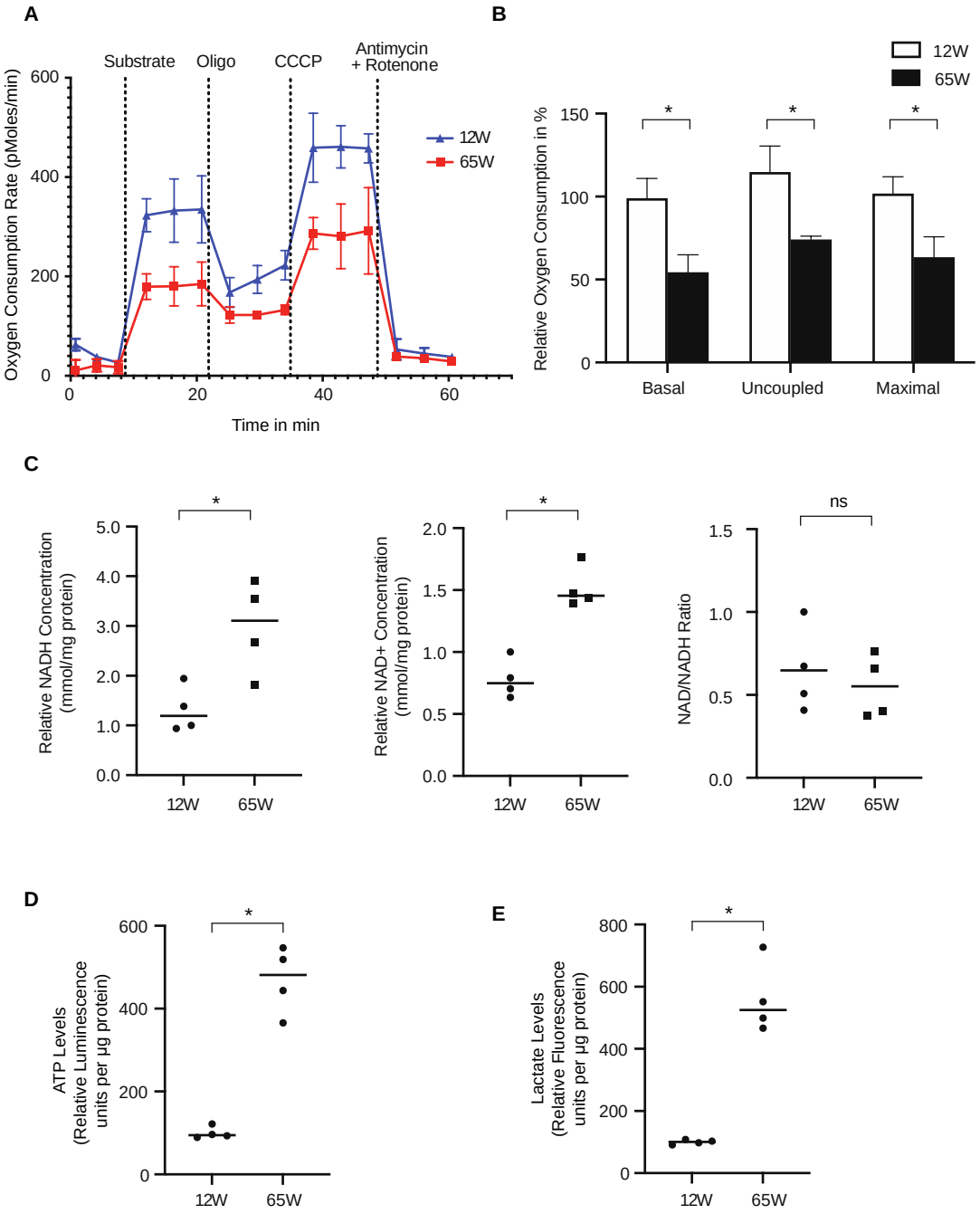

Figure 4.2: Mitochondrial metabolism changes with age.

(A) Freshly isolated mitochondria from both cohorts were subjected to Oxygen consumption rate measurement via a Seahorse Flux Analyzer to determine the respiratory capacity of the mitochondria. (mean ± SD, n=4).

(B) Basal respiration was calculated upon substrate injection; uncoupled respiration was calculated after Oligomycin injection and maximal respiration was calculated after CCCP injection. Relative oxygen consumption per condition was calculated from the average of three measurements. (mean ± SEM, * denotes $p<0.05$, n=4)

(C) Total NAD and NADH were determined from equal amounts of tissue lysate form both cohorts using a NAD/NADH colorimetric assay kit (Sigma Aldrich). NAD+ was calculated as the difference between NAD total and NADH. NAD/NADH ratio was also calculated. NAD+, NADH concentration (absorbance) and NAD/NADH ratio were normalized to the mean of the young mice samples (mean ± SEM, * denotes $p<0.05$, n=3).

(D and **E)** Equal amounts of tissue lysate per cohort were used to determine ATP and Lactate levels respectively via fluorescence assay kits (Abcam) (mean ± SEM, * denotes $p<0.05$, n=3).

Subsequently, we measured the NADH and NAD^+ levels in liver tissue lysates. Interestingly, both metabolites were increased in the 65W mitochondria (Figure 4.2 (C)). However, the NAD^+/NADH ratio was similar in both age groups. Surprisingly, quantification of the ATP levels in the experimental cohort liver lysates showed a significantly higher levels of ATP in the 65W mice samples (Figure 4.2 (D)). To assess if the increased amounts of ATP at steady state were the result of increased glycolysis, we also measured the lactate levels in the same samples and found them to be increased in the 65W mice samples (Figure 4.2 (E)). Accordingly, our results indicated that in the liver samples from older mice the activity of the respiratory chain is decreased and cells display a highly glycolytic metabolism.

4.1.4 Mitochondrial Respiratory Complex IV Activity Reduces with Age

The reduced respiration observed in the mitochondria of 65 week old mice led us to examined the amounts of mtDNA in the isolated mitochondria of the different mice. For this, we utilized equal amounts of purified mitochondria and treated the obtained DNA with RNAse to deplete mitochondrial RNA. Subsequently, we used real time PCR for a quantitative assessment of mtDNA. For complete coverage of mtDNA we used primers designed for several mitochondrial genes. These analyses showed that the mtDNA copy numbers were similar in both 12W and 65W old mice (Figure 4.3 (A)).

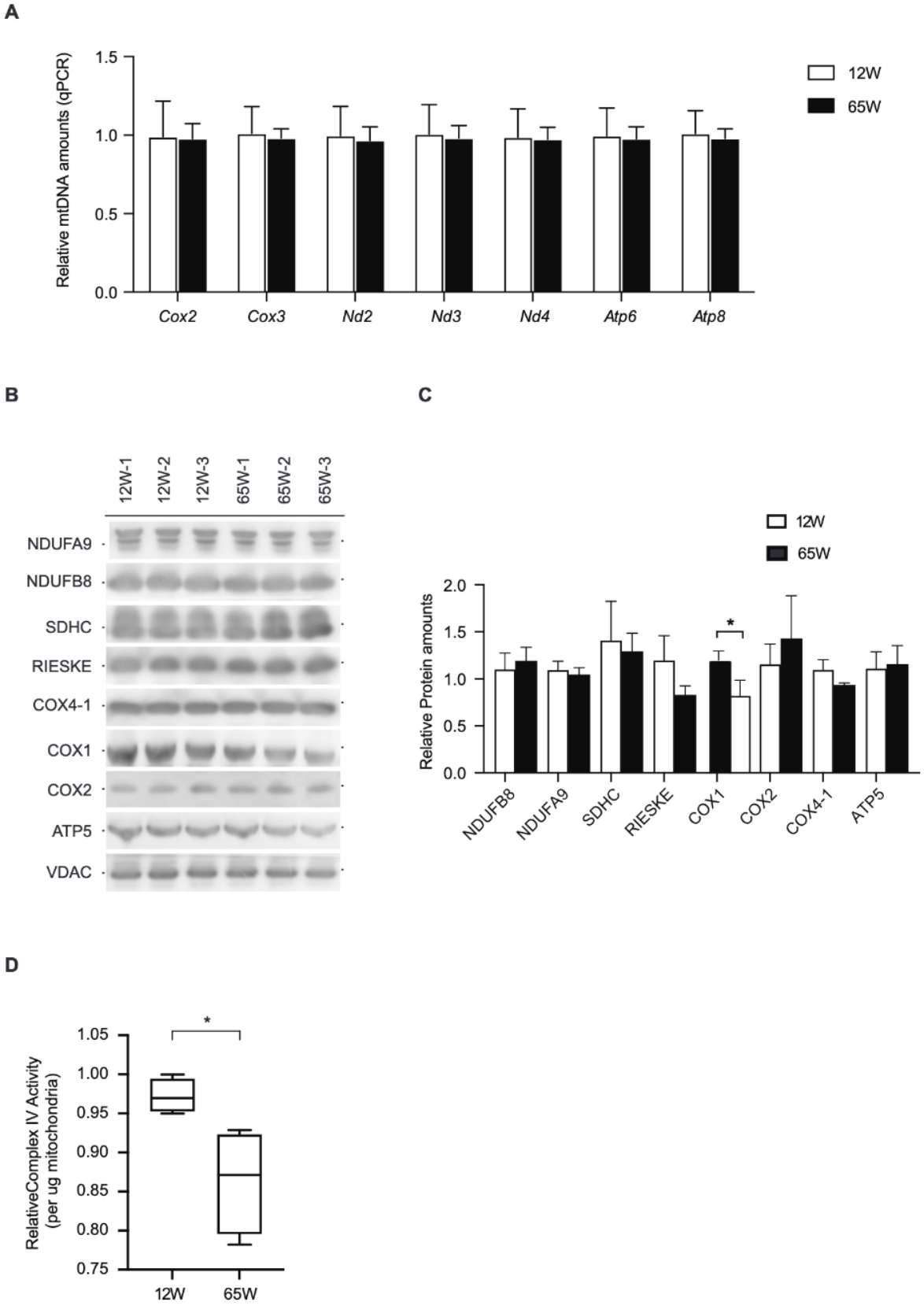

Figure 4.3: OXPHOS Complex IV decreases with age.

(A) Equal amounts of isolated mitochondria from both the cohorts subjected to mtDNA isolation and subsequent qPCR to test the different mt-genes in order to estimate the relative mtDNA amounts (mean ± SEM,

n=4).

(B) Isolated mitochondria from both the cohorts subjected to Tris Tricine-SDS-Page and immunoblotting to check for OXPHOS (n=3).

(C) Area under the curves were calculate with ImageJ and were normalized to Vdac (mean ± SEM, * denotes $p<0.05$, n=3)

(D) Complex IV activity was measured using activity assay microplate kit (Abcam). Complex IV activity was normalized to activity of a young mice samples and the mean ± SEM is shown (* denotes $p<0.05$, n=3).

Next, we analyzed the protein levels of selected subunits of the mitochondrial OXPHOS complexes. Of the mitochondrial proteins addressed, only COX1 showed a reduction in the aged experimental cohort (Figure 4.3 (B)). Quantification of the blots confirmed a statistically significant reduction only in the levels of COX1 in the 65W cohort (Figure 4.3 (C)). These findings suggested a selective effect on the cytochrome c oxidase (complex IV) of the respiratory chain. Accordingly, we assessed the activity of complex IV in the isolated mitochondrial. As expected from the steady state protein analyses, we found that the activity of complex IV was significantly reduced in the 65 week mitochondria samples, with a pronounced degree of variability compared to the 12 week samples (Figure 4.3 (D)). These findings on the activity of complex IV are in agreement with the reduced steady state levels of COX1.

4.1.5 Mitochondrial Transcriptome Profiling by Nanopore Sequencing

To address as to why COX1 levels were reduced in liver mitochondria of 65 week old mice, we decided to assess mitochondrial RNA levels. Since the isolated crude mitochondrial fraction used for our analyses also contained microsomal membranes, we further enriched mitochondria by sucrose density centrifugations. Gradient-purified mitochondria were processed for RNA isolation and subsequent DNAse digestion was performed to avoid mtDNA contamination. The purified RNA was subjected to library preparation and Nanopore sequencing (Figure 4.4 (A)). The use of PCR barcoding allowed us to pool all samples and to analyze these together. Although we used a poly dT primer annealing approach for library generation, we were able to obtain sequencing reads for mitochondrial ribosomal RNAs, *Rnr1* and *Rnr2*. A detailed analysis of the reads showed that both RNAs contain a short internal stretch of poly A (Figure 4.4 (B)). Thus, the presence of an internal A-rich sequence enables poly dT primer annealing and subsequent recovery of *Rnr1* and *Rnr2*.

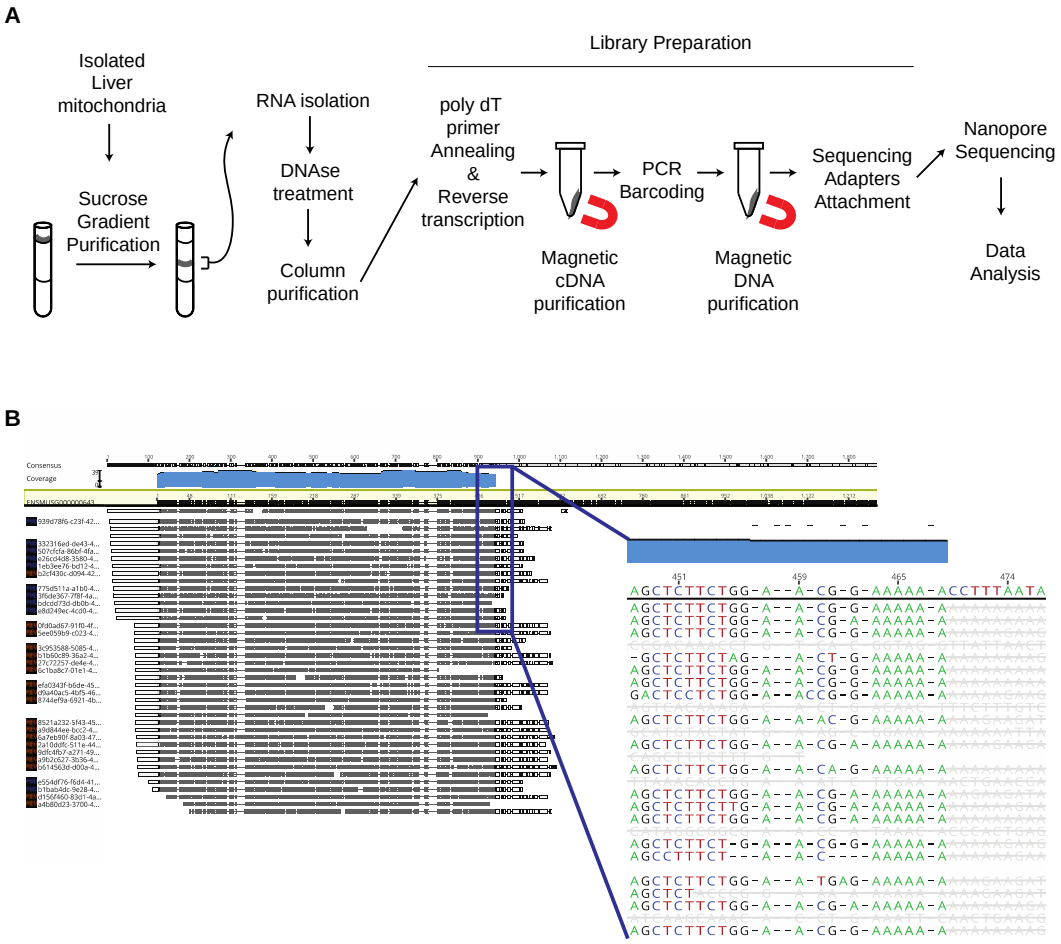

Figure 4.4: OXPHOS Complex IV decreases with age.

(A) Experimental overview of the purification of mitochondrial samples isolated from the livers of the experimental cohorts, RNA isolation, library preparation and Nanopore sequencing.

(B) Representative image of mt-Rnr2 sequencing. Bam alignment file visualization with Geneious Prime shows the reference sequence highlighted in yellow and the consensus is marked in blue. Blue box shows a magnified view of the alignment in the region where the poly dT primer anneals during the library preparation.

Subsequently, the Nanopore sequencing results were analyzed using the Epi2me Labs differential gene expression pipeline (Oxford Nanopore Technologies). Normalization of the data to *Rnr2* was carried out and results displayed in a heatmap visualization. Interestingly, these analyses revealed that the *Cox1* transcript was strongly decreased in all the 65W samples (Figure 4.5 (A)).

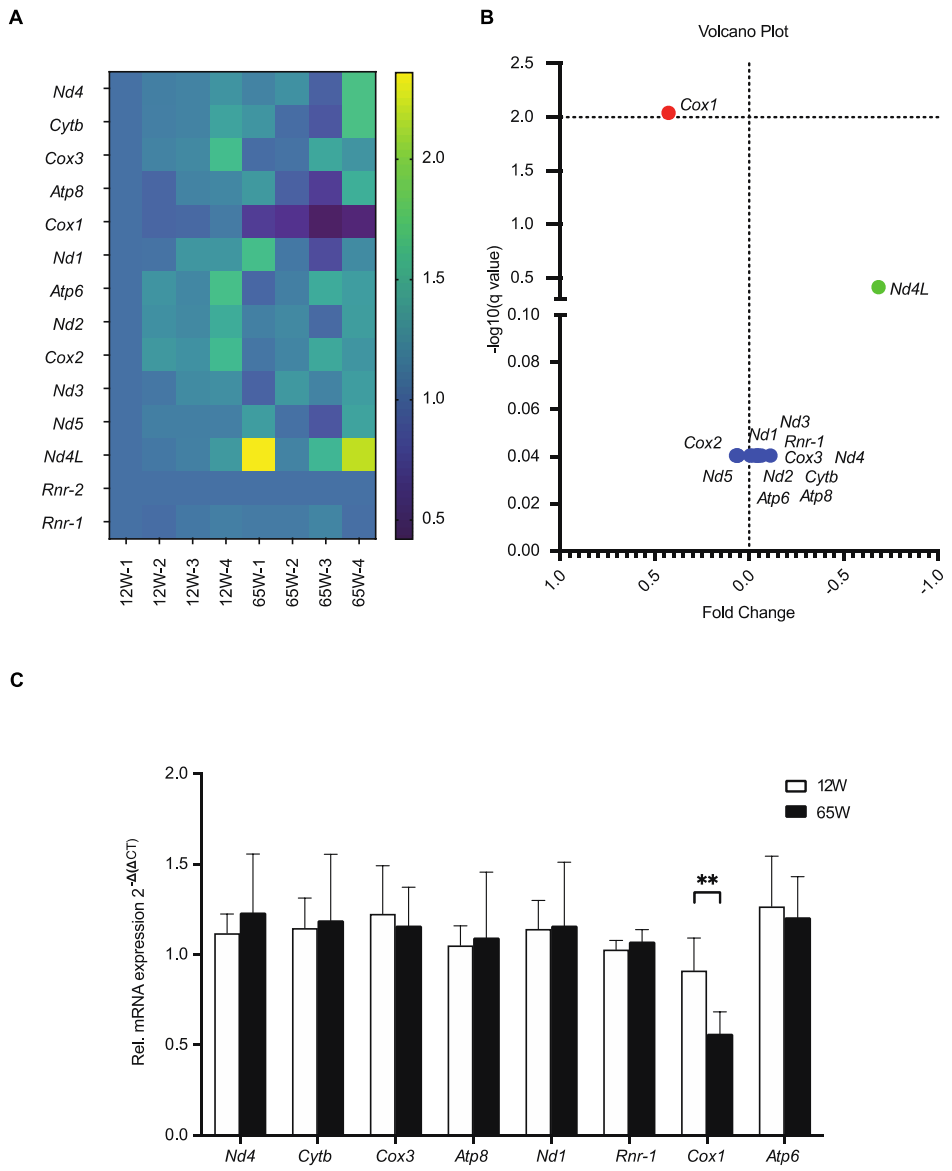

Figure 4.5: OXPHOS complex IV decreases with age .

(A) Heatmap analysis of the normalized transcript counts obtained from the differential gene expression workflow from Epi2Me Labs. Counts normalized to *mt-Rnr2*. Heatmap generated using GraphPad Prism 9 (n=4).

(B) Volcano plot analysis of **(A)** generated using GraphPad Prism 9 (mean ± SEM, n=4).

(C) Analysis of gene expression of mitochondrial transcripts in total mRNA isolated from 12W and 65W liver samples by qPCR. (means ± SEMs, * denotes $p<0.05$, n = 4)

Further statistical analysis showed that *Cox1* was the only transcript that was significantly different between mitochondria of the 65W samples and those from the 12W ones (Figure 4.5 (B)). Considering, that we had incorporated barcodes using PCR in the experimental setup in order to multiplex the analysis, we decided to further exclude a PCR bias and inaccurate

transcript number estimation. Therefore, we carried out qPCR analyses to confirmed the reduction of the *Cox1* transcript by an alternative approach. Utilizing this second strategy, we were able to confirm the reduction the *Cox1* transcript in liver mitochondria of 65W samples (Figure 4.5 (C)). In conclusion, we observed a reduction of complex IV activity due to decrease in the levels of *Cox1* mRNA and protein. This finding agrees with the observed decline in OXPHOS activity and changes of mitochondrial health parameters that we observe in the liver mitochondria from mice samples with age.

5 Discussion

5.1 The Role of Cox14 in Cox1 Translation and Complex IV Assembly

This study aimed to elucidate the role of Cox14 in Cox1 translation and the assembly process of Complex IV. The results showed that a mutation in Cox14 resulted in a drastic reduction of Cox1 translation on the one hand and MITRAC complex levels on the other. However, because associations were still found between the components of the MITRAC complex, it can be assumed that it was not the accumulation or association of the factors per se that was disrupted. The reduced MITRAC complex levels could be rather a consequence of its decreased formation in absence of assembly factors and Cox1. In addition, the decrease could originate from faster degradation due to its impaired stability.

These results in COX14M19I are consistent with the results of previous studies on its human homolog C12orf62 in human cell models, supporting the hypothesis that Cox14 may be a Cox1-specific translational factor (Mick et al. 2012; Weraarpachai et al. 2012a; Clemente et al. 2013).

5.2 The Effects of Mutation in Cox14 on the OXPHOS System

Analysis of OXPHOS proteins and complexes, as well as their activity, revealed differential, tissue-specific effects due to the Cox14 mutation. While Complex IV was most reduced in heart and muscle, there was only a small reduction in Complex IV in brain in particular. In contrast, analysis of OXPHOS proteins showed a similarly strong reduction of Complex IV subunits in all four organs examined, but with strongest decrease in liver. A possible explanation would be that in brain a slower degradation of existing complexes takes place. Hence, even if fewer proteins are newly formed, complex levels do not change much due to the longevity of the existing complexes.

However, it was shown that the half-life of mitochondrial proteins is similar in heart, muscle and brain. In contrast, mitochondrial proteins in liver show the shortest half-life time (Miwa et al. 2008; Karunadharma et al. 2015). This could explain the strong decrease of mitochondrial proteins in liver. This also hints to the presence of different compensatory mechanisms, that

cause the increased stability of OXPHOS complexes especially in brain compared to heart and muscle in COX14M19I. Additionally, the heart and muscle have been shown to have higher total concentrations of respiratory chain complexes per mitochondrion compared with liver and brain (Benard et al. 2006; Johnson et al. 2007; Phillips et al. 2012). Thus, a Complex IV biogenesis disorder could have a greater impact on tissues that possess and produce more complexes, explaining the stronger effects on Complex IV abundance in heart.

Besides OXPHOS complex levels, this study also addressed the activity of the individual Complexes I and IV as well as the overall OXPHOS activity. The differences in activity of the Complexes I and IV observed in the mutants compared to the controls, could be influenced by two factors: a. the differences in amounts of the complexes per mitochondria of the different genotypes, or b. the altered activity of the individual complexes themselves.

Complex IV, OXPHOS and Complex I activity did not decrease significantly in brain of COX14M19I.

In stark contrast, Complex IV activity appeared to affect liver the most. Despite lower Complex IV levels in heart and muscle, there was relatively little overall decrease in Complex IV activity in either organ. Similarly, in another study examining the effects of a mutation of Surf1, Complex IV activity declined the most in liver (Deepa et al. 2018). Interestingly, only the heart showed also a strongly increased Complex I activity.

This study presents a contradiction that the heart and muscle have greater reduction in Complex IV levels than the liver, but nevertheless show significantly higher enzyme activity. One possible explanation could be the ability of the mitochondria in heart and muscle, to increase their activity many times above "resting activity" under metabolic stress (Benard et al. 2006; Johnson et al. 2007; Phillips et al. 2012). In contrast to liver and brain, mitochondria in heart and muscle are exposed to highly changing metabolic conditions. For example, tissue activity, perfusion and oxygen supply can alternate drastically during exercise in heart and muscle, while overall activity of the brain and liver remain relatively constant (Heinonen et al. 2014).

OXPHOS activity could be regulated either by complex levels per se through increased or decreased translation of subunits or post-translational modifications such as phosphorylation and tissue specific metabolic stress signaling (Li et al. 2007; Yadava et al. 2008; Phillips et al. 2012). Complex I activity was strongly increased in the heart. It is tempting to speculate that the COX14M19I heart mitochondria, instead of relying on FADH from fatty acids,

increasingly rely on NADH converted by lactate for the respiratory chain. This may lead to increased Complex I activity (Wisneski et al. 1985; Balaban et al. 1986; Gertz et al. 1988; Stanley et al. 1997; Kemppainen et al. 2002). Since heart is the only organ that metabolizes lactate sufficiently, it can counteract lactic acidosis in the blood that may have resulted from the anaerobic metabolic state in the peripheral organs (Dong et al. 2021).

Furthermore, this study shows Complex IV to be present in either a monomeric form or assembled in super complexes in the brain of COX14M19I. Accumulation of the Complexes IV in large super complexes might also display a compensatory mechanism of the deficiency in order to achieve the highest possible activity of the respiratory chain, despite reduced Complex IV amounts (Schägger and Pfeiffer 2000; Greggio et al. 2017; Brave and Becker 2020).

Considering the high variation these observations need to be strengthened by more repetitions in the future.

5.3 Damage to Mitochondrial Membrane Structure in Hepatocytes

Electron microscopy revealed a structural damage in mitochondria of COX14M19I hepatocytes. Disruptive membranes, discontinuous cristae structure and pore-like membrane formations were evident as compared to WT controls. The pictures showed similarities to apoptotic cells, in which mitochondria form pores and release cytochrome c from the IMS into the cytosol (Karbowski and Youle 2003; Tinari et al. 2008). However, western blot analysis did not show differences in levels of proteins involved in apoptosis. Due to the limited wild type samples and lack of positive controls, the sensitivity of detection of apoptotic events in tissue lysates could not be strongly asserted.

Alternatively, it was shown, that mitochondria formed pores by oligomerization of VDAC, in response to oxidative stress (Kim et al. 2019). In addition, it has been reported that mitochondrial organization is a highly dynamic process, which is strongly related to membrane protein function and is influenced by several factors. For example, respiratory chain dysfunction can cause increased ROS production, which in turn disrupts mitochondrial membrane structure (Zorov et al. 2014; Moon et al. 2016). ROS was also found to trigger the opening of the mitochondrial transition pore - a pore complex in the IMM, which could be passed by small molecules with a size up to 1.5 kDA (Šileikytė and Forte 2019).

Frequently, members of the BCL2 family were reported to form pores releasing mitochondrial DNA – also in other context than apoptosis (Patrushev et al. 2004; McArthur et al. 2018). However, the triggers of this process remained unclear in present studies. Thus, the process of pore formation in response to mitochondrial dysfunction offers a lot of potential for further research.

5.4 Antiviral Signaling

Transcriptome analysis suggested an activation of a systemic antiviral immune response mediated by interferons in COX14M19I mice tissues. To examine the immune response in more detail, three key questions need to be addressed.

1. Is it a systemic or local immune response and which interferon types are involved?
2. Which cells are involved and which amongst them are responsible for interferon release?
3. What is the underlying trigger for the onset of an antiviral immune response?

Interferons can be distinguished into type I and type II interferons (Lee and Ashkar 2018). Type I interferons include interferon alpha and beta, which are secreted primarily by (tissue-derived) monocytes/macrophages and virus-infected cells (Meurs et al. 1990). The most important type II interferon is interferon gamma, which is secreted from natural killer cells (NK cells) to activate cytotoxic t cells (Lee et al. 2017).

FACS analysis showed elevated serum concentrations of interferons alpha and beta, but not gamma. Thus, a systemic type I interferon response was evident in COX14M19I. The increased concentration of IL-10 suggested regulation of the immune response (Couper et al. 2008). Interferons bind to specific extracellular interferon receptors to induce the transcription of interferon-stimulated genes (Schneider et al. 2014) (Figure 5.1). This gene induction could be detected by transcriptome analysis in all four tissues. Firstly, the induced factors showed expression typical for type I interferon receptor activation (Figure 5.1). Secondly, the fact that not only one specific tissue but all four showed this response underlined that it was a generalized immune response.

In addition, Isg15 showed strong induction in COX14M19I. As an interferon type I-induced cytokine, it causes the release of interferon gamma by binding to CD11a (LFA-1) of NK cells

in particular. This initially seems to contradict the low interferon gamma levels in COX14M19I (Farrell et al. 1979; Bogunovic et al. 2012; Swaim et al. 2017). However, CD11b- NK cells were especially dominant in COX14M19I. These were shown to be a group of tolerant NK cells that do not secrete effector cytokines (Fu et al. 2014). Thus, low interferon gamma concentrations are explained by immunoregulatory mechanisms at the level of cellular differentiation. Furthermore, strong induction of Usp18, which is known to be a direct antagonist of Isg15, also showed regulation at the protein level (Malakhov et al. 2002).

This leads to the question of which cells are responsible for the release of interferons type I. On the one hand, it could be the immune cells, especially tissue-derived macrophages, or on the other hand the parenchymal cells. Translation of interferons is induced by phosphorylation of interferon regulatory factors, particularly IRF 3 and IRF 7 (Fitzgerald et al. 2003; Sharma et al. 2003; McWhirter et al. 2004; Ning et al. 2011) (Figure 5.1). This is triggered via the central regulatory factors MAVS and STING, which in turn can be activated via PRRs (Kawai et al. 2005; Meylan et al. 2005; Seth et al. 2005; Ishikawa and Barber 2008; Bahat et al. 2021).

Western blot analysis of the liver showed increased levels of Irf7, but not phosphorylation of the IRFs. In addition, the proteins MAVS and STING were not detectable in liver by immunodetection. In fact, recent studies doubt the possibility of MAVS and especially STING dependent interferon induction in hepatocytes, since STING was only expressed by NPCs and not in hepatocytes (Thomsen et al. 2016). In contrast, in COX14M19I liver the activation of the receptor response pathway was shown, particularly by the factors Stat1 and Stat2. Significant induction of some PRRs in the liver of COX14M19I can be rationalized by considering that the PRRs are also interferon-induced genes (Schneider et al. 2014). As such, they could be induced by external stimulation of hepatocyte interferon receptors. Thus, it might be possible that in COX14M19I hepatocytes, PRRs may not be directly involved in sensing and thus triggering the interferon response. Furthermore, attempts were made to isolate and culture hepatocytes. However, it was revealed that, the high expression of interferon-induced in the mutant cells decreased to wild-type levels over time upon ex-vivo culture. Thus, it can be hypothesized that it is not the hepatocytes but the non-parenchymal cells (NPCs) or circulating immune cells that are responsible for interferon release in COX14M19I. This can be corroborated by recent study results, which showed that hepatic resident macrophages, especially Kupffer cells, are key players in hepatic inflammation processes (Liu et al. 2010; Luo et al. 2018; Yu et al. 2019; An et al. 2020).

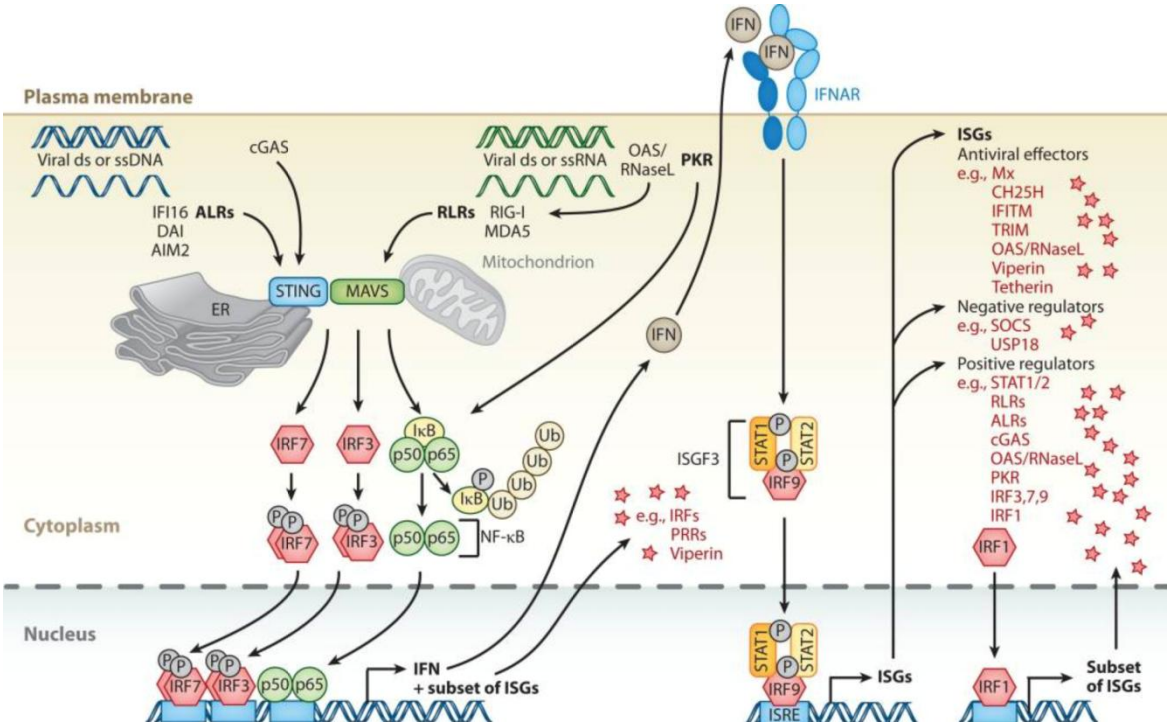

Figure 5.1: Intracellular Interferon Type I signaling.

From Schneider et al. 2014. Courtesy of Annual reviews, Order License ID 1255754-1, ISSN 1545-3278.

This leads to the most important question: What is the trigger of the immune response?

The fundamental trigger of an interferon response is the recognition of viral material by PRRs, especially foreign nucleic acids (Li and Wu 2021). More and more studies have shown, that also mitochondrial damage-associated molecular patterns (DAMPs), especially mitochondrial DNA and RNA could trigger the PRRs, since it structurally resembles foreign nucleic acids (Collins et al. 2004; Dhir et al. 2018; Kim et al. 2019; Huang et al. 2020).

The results, showing increased extramitochondrial concentrations of mitochondrial nucleic acids in COX14M19I, thus have to be discussed carefully. The lack of internal standards due to the inherent absence of DNA moieties in cytoplasmic fractions limited normalization of the results. Therefore, to minimize errors, mtDNA amounts were measured by two independent methods (qPCR and Taq-PCR based agarose gel electrophoresis). Moreover, it was confirmed by sequencing, that PCR products that are quantified in the results indeed originate from specific amplification of mitochondrial DNA.

Furthermore, it is important to note, that the isolated extramitochondrial fraction can be of either extracellular or cytosolic origin. Thus, a distinction between these two compartments cannot be made by the experimental procedures used in this study. Hence, it could be

concluded that mitochondria in COX14M19I liver do release nucleic acids, but their exact amounts cannot be quantified by the established methods.

Still, it is unclear, if these nucleic acids are the actual trigger and which PRRs could be responsible for their detection. As previously discussed, PRRs, reported to recognize mitochondrial cytosolic nucleic acids showed higher expression in COX14M19I (Li and Wu 2021), but did not appear to consequently induce the phosphorylation and activation of interferon regulatory factors. Since it was shown, that extracellular mitochondrial nucleic acids might trigger NPCs by recognition of Toll like receptors (TLRs) (Garcia-Martinez et al. 2016), it is tempting to speculate, that induction of the interferon signaling does not occur in hepatocytes. They just are the source of the DAMPs for the NPCs to be activated. Additionally, since it was also observed that mitochondrial nucleic acid concentration in the blood did not change, the release and recognition must be limited to the site of the organs.

Because the stimulation of NPCs and macrophages in COX14M19I was not examined in this study, it could be a potential avenue for future experiments. Thus, the release of mitochondrial nucleic acids and its effect on NPCs could be assessed using isolated hepatocytes. Finally, it is also important to emphasize, that other DAMPs were examined in this study. These include for example Cardiolipin, ATP, N-formyl peptides or other mitochondrial factors, that were shown to own immunostimulatory potential (Nakahira et al. 2015). Future experiments could also look at the role of these additional factors in eliciting the interferon signaling observed in the COX14M19I mice.

5.5 Lipid Metabolism

In addition to increased interferon concentrations, the blood of COX14M19I mice also showed increased cholesterol levels. The induction of several key enzymes of cholesterol biosynthesis in the liver also indicated that the production of cholesterol in COX14M19I was stimulated.

This observation contrasts with a large number of studies showing that an interferon response in particular leads to a suppression of cholesterol synthesis and thus to hypocholesterolemia (Robertson and Ghazal 2016). Moreover, it seems counterintuitive that the energy-consuming synthesis of cholesterol should be stimulated in presence of a mitochondrial dysfunction (Luo et al. 2020).

This study could not investigate the reasons for the induction of the cholesterol pathway in more detail. Cholesterol and HDL, but not Triglyceride levels were increased in COX14M19I. This may indicate the involvement of PPAR alpha, a key player in the regulation of triglyceride levels. PPAR alpha counteracts high TAG levels by increasing HDL formation and enhancing beta oxidation, among other mechanisms (Pawlak et al. 2015). Strikingly, it also appears to have anti-inflammatory functions, particularly in liver tissue (Jiao et al. 2014; Pawlak et al. 2015). Therefore, its actual impact on COX14M19I should be examined in future experiments.

Lipid- and cholesterol biosynthesis have been shown to be upregulated by the abundant availability of precursors such as acetyl-CoA, particularly in tumor cells. These undergo a metabolic switch from aerobic to anaerobic glycolysis and lactate production, commonly known as the Warburg effect (WARBURG 1956; DeBerardinis et al. 2008; Biswas et al. 2012).

Alternatively, the regulation of SREBP could be disturbed by increased oxidative stress.

A distinct observation made in this study was the upregulation of perilipin 5 in the liver of COX14M19I, a central factor in lipid droplet formation. These results are consistent with studies that suggested induction of perilipin 5 by mitochondrial dysfunction (Li et al. 2012; Lee et al. 2013b). Perilipin 5 is particularly expressed in tissues with high oxidative stress and appears to be an important antioxidant factor (Kuramoto et al., 2012; Montgomery et al., 2018; Zheng et al., 2017; P.-L. Zhou et al., 2017; Zhu, Ren, Zhang, and Zhong, 2020). By forming lipid droplets, it counteracts toxic accumulation of free fatty acids and causes the association of mitochondria to lipid droplets, referred to as peridroplet mitochondria (PDM) (Benador et al., 2018; H. Wang et al., 2011). These PDMs exhibit special characteristics, such as increased activity of respiratory capacity and respiratory chain complexes and decreased beta oxidation (Benador et al. 2018). This perilipin 5 mediated formation of lipid droplets has been frequently reported in the context of access lipid accumulation during NAFLD in human liver or cardiomyopathy (Pollak et al. 2013; Wang et al. 2013; Mass Sanchez et al. 2021). Thus, it might be hypothesized that histopathological picture in COX14M19I tissues results out of a similar mechanism.

5.6 Mitochondrial Dysfunction - A Driver of Human Diseases?

COX14M19I showed the development of several pathologies, such as NASH, cardiomyopathy, or the induction of inflammatory signaling pathways. But what conclusions could be drawn from the mouse model in order to correlate to the patient phenotype?

First, it is important to emphasize that, in general, humans are much more severely affected by mutations of the mitochondrial genome than mice. The human carrier of the mutation in C12orf62 died of lactic acidosis within a few hours of life (Weraarpachai et al. 2012a), whereas the mouse was not drastically limited in life expectancy.

However, considering COX14M19I as an example of milder mitochondrial dysfunction in various human tissues, fundamental implications can be drawn that shed new light on the role of mitochondrial dysfunction in the development of multifactorial human diseases. There could be a plethora of reasons for such a milder dysfunction. For example, the accumulation of mutations in the mitochondrial genome of individual mitochondria, which only lead to the onset of the disease when a certain proportion of mitochondria is affected - a concept described as heteroplasmy (Stewart and Chinnery 2015). Also, single nucleotide polymorphisms or an accumulative effect of severe environmental stress might be other reasons for milder mitochondrial dysfunctions in human cells (Meyer et al. 2013; Zhao et al. 2022).

Two underlying effects caused by mitochondrial dysfunction in COX14M19I have been observed:

1. The release of mitochondrial nucleic acids and, as a consequence, sterile chronic inflammation.

2. The formation and accumulation of lipid droplets via perilipin 5.

In COX14M19I, the significance of this is particularly evident in the liver, where both pathways converge in the strongest expression and, as a consequence, a NASH-like phenotype develops. Parallels to the development of NASH in humans, which arises from hepatosteatosis (NAFLD), are apparent. For example, perilipin 5 plays a crucial role in fatty liver disease, the inflammatory component of NASH also appears to be driven by the Sting/Interferon pathway and increased mtDAMP levels have been reported (Garcia-Martinez

et al. 2016; Luo et al. 2018; Yu et al. 2019; Mass Sanchez et al. 2021). More so, NASH is considered one of the major risk factors for the development of hepatocellular carcinoma (HCC) in humans (Anstee et al. 2019).

Although one-year-old COX14M19I have not yet shown evidence of tumorigenesis in the liver, several risk factors for the development of HCC are evident in COX14M19I:

First, a chronic sterile inflammatory stimulus seems to promote carcinogenesis in the liver (Yu et al. 2018). In addition, the immunophenotype showed suppression of effector NK cells. This has been reported to promote HCC progression by reducing tumor surveillance (Jin et al. 2013; Zhang et al. 2017). Other phenotypic characteristics, such as secretion of CCL2 and CCL5, but also expression of Ly6 proteins have been reported as drivers of carcinogenesis (Mohs et al. 2017; Zhuang et al. 2018; Upadhyay 2019).

Yet, in the context of NAFLD, NASH and HCC, mitochondrial dysfunction has been regarded primarily as a reason for elevated ROS levels (Dornas and Schuppan 2020). However, this and other recent studies reveal that mitochondrial dysfunction by itself can also cause lipid accumulation and sterile inflammation (Sprenger et al. 2021).

The inflammatory pathway, evident in all COX14M

19I tissues investigated, has also been described in the context of a variety of other diseases such as neurodegeneration, autoimmune or cardiovascular diseases (Role of Mitochondrial Nucleic Acid Sensing Pathways in Health and Patho-Physiology 2022). This recommends a paradigm shift to consider mitochondrial dysfunction as a key driver in the multifactorial genesis of NASH, but also in many other common human diseases. Potentially, promising new therapeutic approaches could thus be achieved by targeting mitochondrial (dys)function and blocking downstream signaling factors (Murphy und Hartley 2018).

6 Conclusion

This study investigated the role of the cytosol-translated factor Cox14 in translation of the mitochondrial protein Cox1 and assembly of Complex IV. For this purpose, a COX14M19I mouse line with mutation of *Cox14* was generated. In COX14M19I, translation of Cox1 was severely reduced. In addition, the MITRAC Complex was formed to a much lesser extent. Thus, Cox14 appears to coordinate the Complex IV assembly process by stimulating Cox1 translation and stabilizing the MITRAC Complex. Consequently, Cox14 is thought to play a key role in regulating Complex IV formation and provides an interface between the translation of cytosolic and mitochondrial complex subunits.

Because mitochondrial diseases generally have a very broad spectrum of symptoms, this study compared the effects on the OXPHOS system and the resulting phenotype in brain, liver, heart, and muscle. Decreased levels of Complex IV were found in all four tissues. Brain was least affected and the activity of the OXPHOS system remained at wild type levels. In contrast, liver was most affected by Complex IV deficiency.

Hepatocyte mitochondria exhibited damage in the mitochondrial double membrane structure. This could lead to the release of mitochondrial damage associated molecular patterns (DAMPs), especially mitochondrial RNA and DNA. In COX14M19I, increased amounts of mitochondrial nucleic acids were found extramitochondrially. Furthermore, an interferon type I-induced immune response was evident in all four tissues examined. This appeared to be due to binding of interferons to extracellular interferon receptors mediated by Stat1 and Stat2. We hypothesized that most likely tissue-derived macrophages could be activated by mitochondrial nucleic acids, especially in liver.

Also, in liver, cholesterol biosynthesis and fat storage in the form of lipid droplets via perilipin 5 were increased. This resulted in hepatosteatosis expression in young COX14M19I mice. With age, an inflammatory component was further evident and a NASH-like phenotype evolved. In addition, COX14M19I showed development of cardiomyopathy with vacuolar

degeneration. All in all, this demonstrated an important link between primary mitochondrial defects and the development of secondary, systemic diseases.

7 Appendix

7.1 Effects of the Cox14 Mutation on OXPHOS Protein Complexes

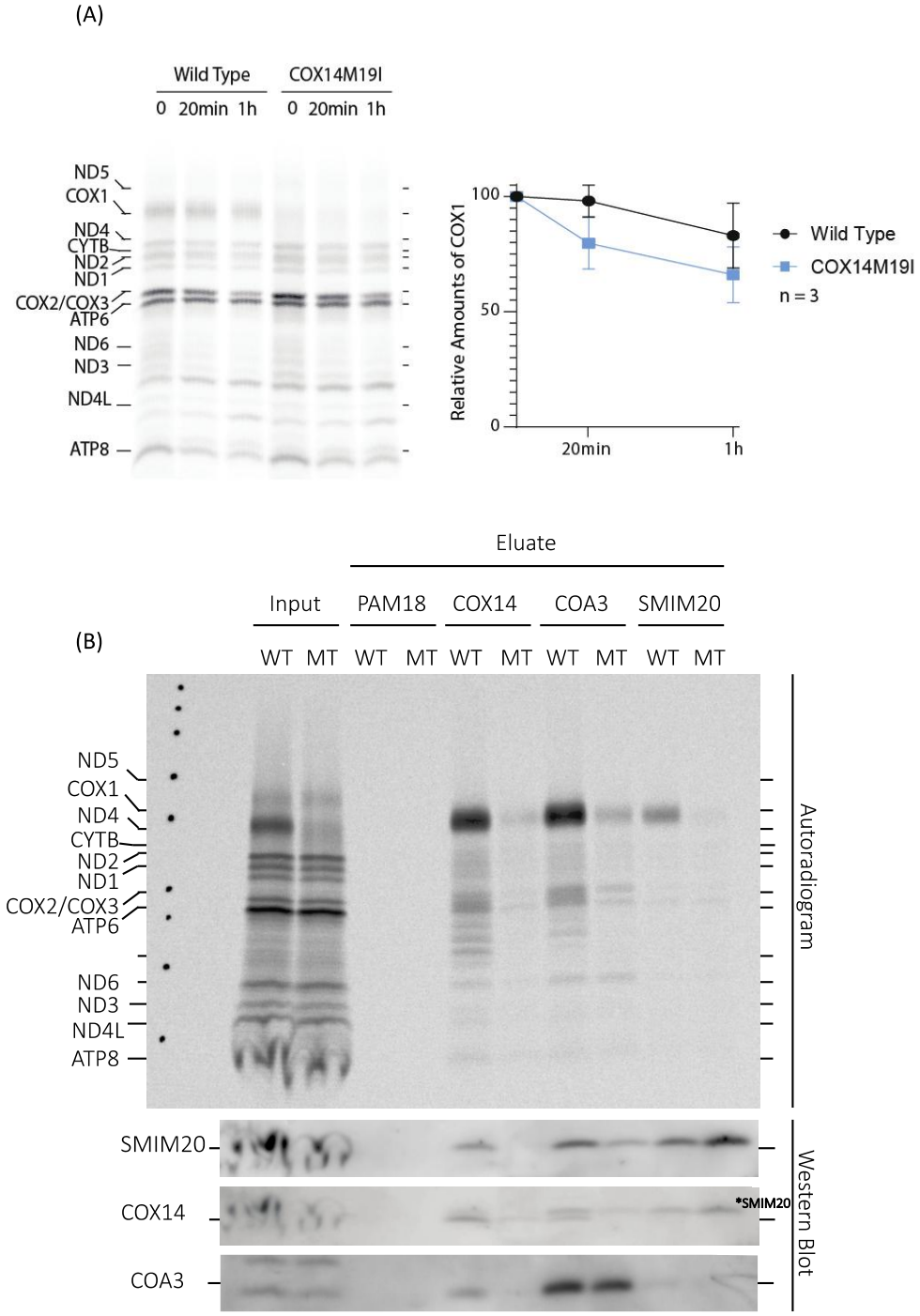

Figure A.1: Cox1 Translation and Mitrac Complex assembly.

(A) The Pulse Chase was conducted to address the freshly translated Cox1 stability. The mean ± SEM is shown (n = 3).

(B) Immunoprecipitation and Immunoblotting was used to assess the assembly of the Mitrac complex. Supplementary to Figure 3.1.

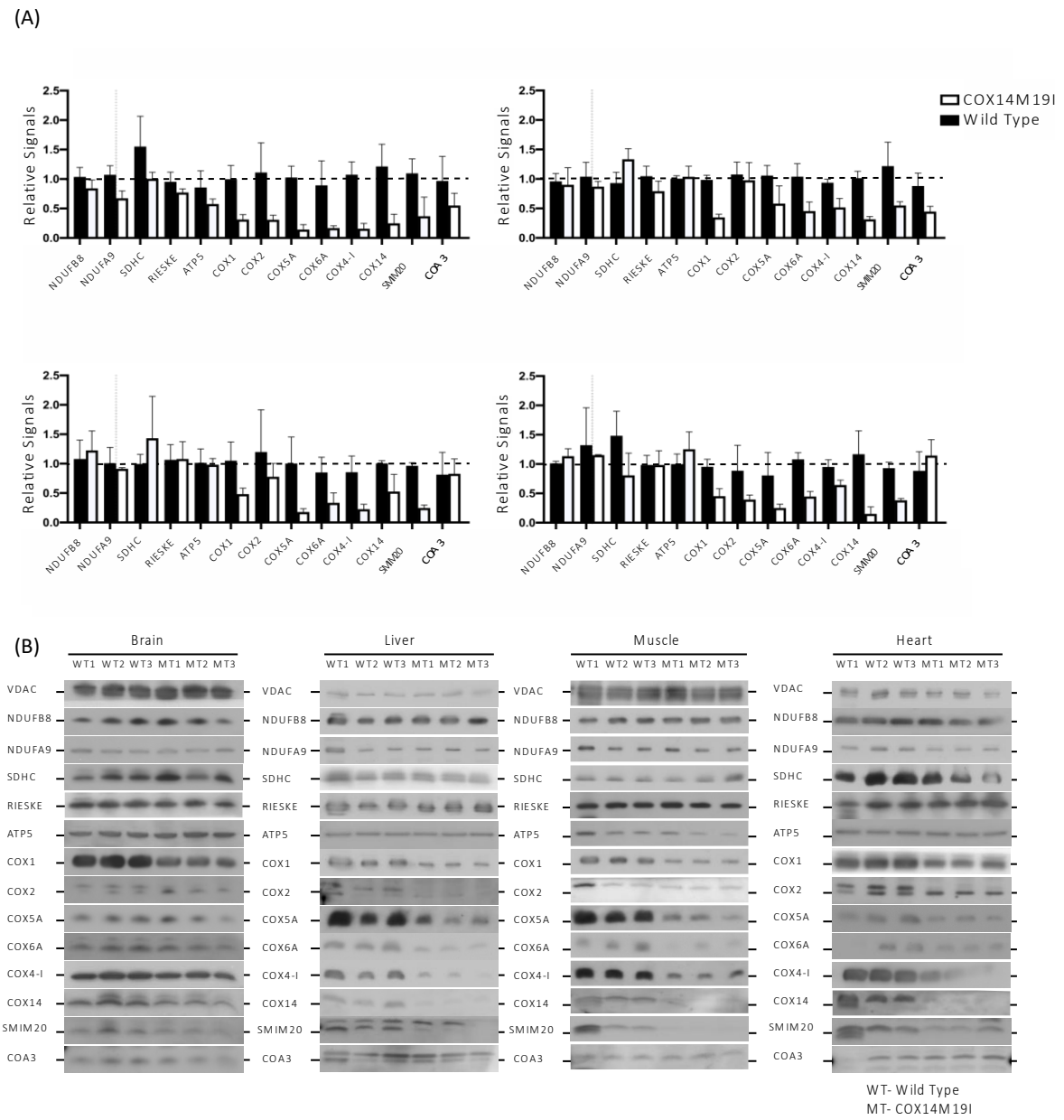

Figure A.2: OXPHOS Protein levels.

(A) Quantification of **(B)** immunoblotting. WT was set to 100% and VDAC signals were used for quantification **(B)**. The mean ± SEM is shown (n = 3). Supplementary to Figure 3.2.

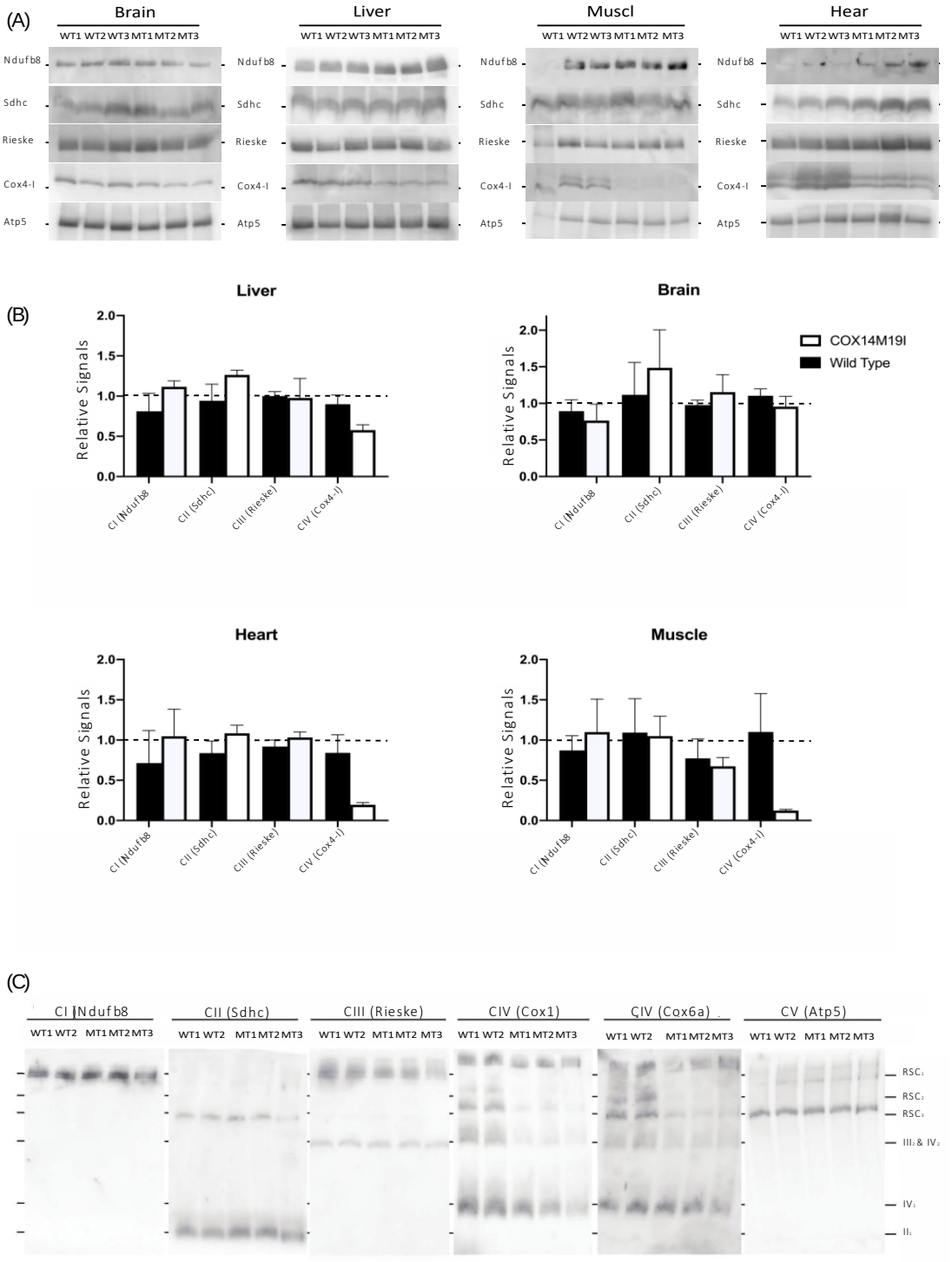

Figure A.3: OXPHOS Complex Levels.

(A) BN Page using DDM and (C) digitonin for solubilization. **(B)** Quantification of **(A)** using signals of Complex V for normalization. The mean ± SEM is shown (n = 3). Supplementary to Figure 3.2.

7.2 The Inflammatory Pathway in COX14M19I

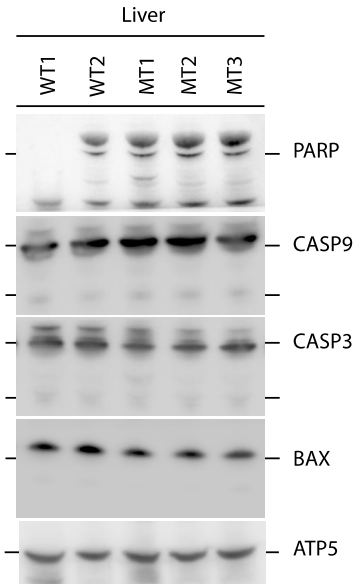

Figure A.4: Apoptotic proteins did not show significant changes in the liver.
SDS-Page and Western blot was used to analyze apoptotic proteins in liver tissue. WT, Wild Type; MT, COX14M19I.

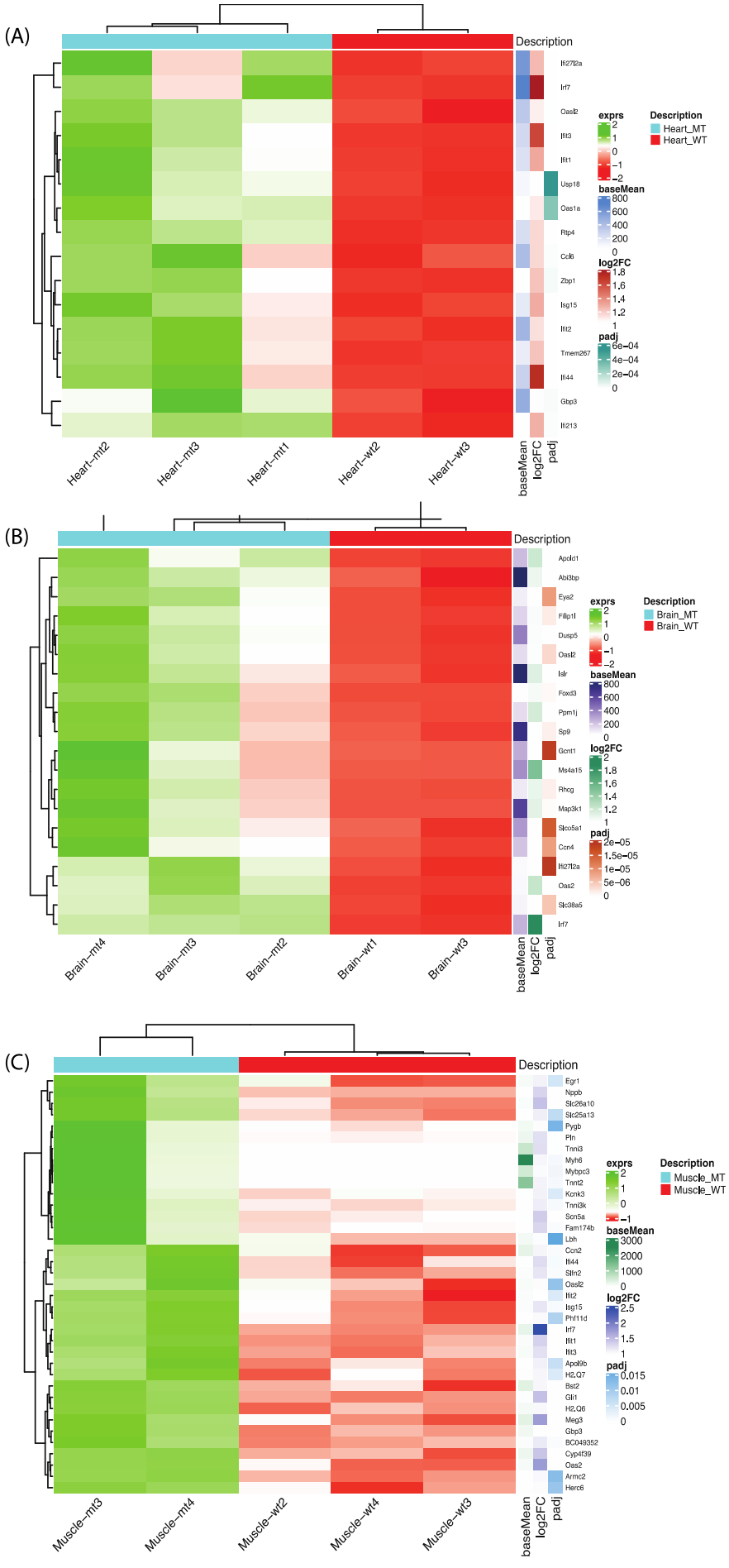
(A)
Description
Ifi27l2a
Irf7
Oasl2
Ifit3
Ifit1
Usp18
Oas1a
Rtp4
Ccl6
Zbp1
Isg15
Ifit2
Tmem267
Ifi44
Gbp3
Ifi213
exprs
Description
Heart_MT
Heart_WT
baseMean
log2FC
padj
Heart−mt2
Heart−mt3
Heart−mt1
Heart−wt2
Heart−wt3
(B)
Description
Apold1
Abi3bp
Eya2
Filip1l
Dusp5
Oasl2
Islr
Foxd3
Ppm1j
Sp9
Gcnt1
Ms4a15
Rhcg
Map3k1
Slco5a1
Ccn4
Ifi27l2a
Oas2
Slc38a5
Irf7
exprs
Description
Brain_MT
Brain_WT
baseMean
log2FC
padj
Brain−mt4
Brain−mt3
Brain−mt2
Brain−wt1
Brain−wt3
(C)
Description
Egr1
Nppb
Slc26a10
Slc25a13
Pygb
Pfn
Tnni3
Myh6
Mybpc3
Tnnt2
Kcnk3
Tnni3k
Scn5a
Fam174b
Lbh
Ccn2
Ifi44
Slfn2
Oasl2
Ifit2
Isg15
Phf11d
Irf7
Ifit1
Ifit3
Apol9b
H2.Q7
Bst2
Gli1
H2.Q6
Meg3
Gbp3
BC049352
Cyp4f39
Oas2
Armc2
Herc6
exprs
Description
Muscle_MT
Muscle_WT
baseMean
log2FC
padj
Muscle−mt3
Muscle−mt4
Muscle−wt2
Muscle−wt4
Muscle−wt3

Figure A.5: Transcriptome Analysis.

RNA sequencing was performed with isolated mRNA of brain (B), muscle (C) and heart (A) and overview of upregulated genes are shown. Supplementary to Figure 3.5

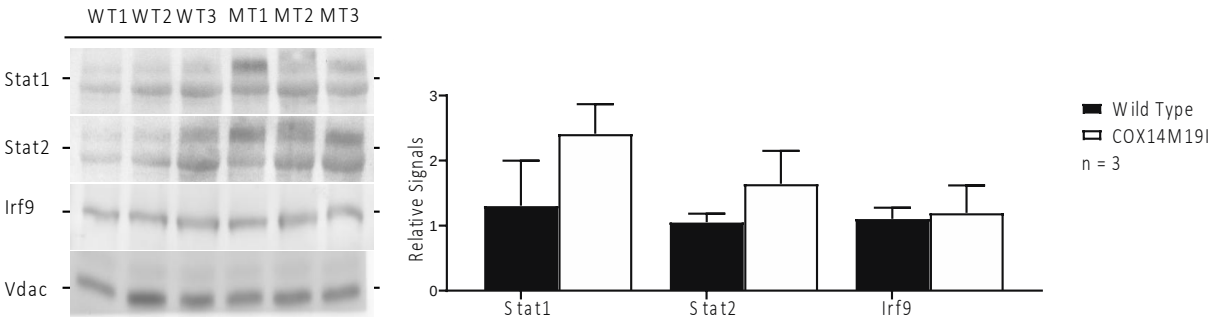

Figure A.6: ISGF3 Complex Activation.

Immunodetection of ISGF3 Complex components using Vdac for quantification. The mean ± SEM is shown (n=3). Supplementary to Figure 3.6.

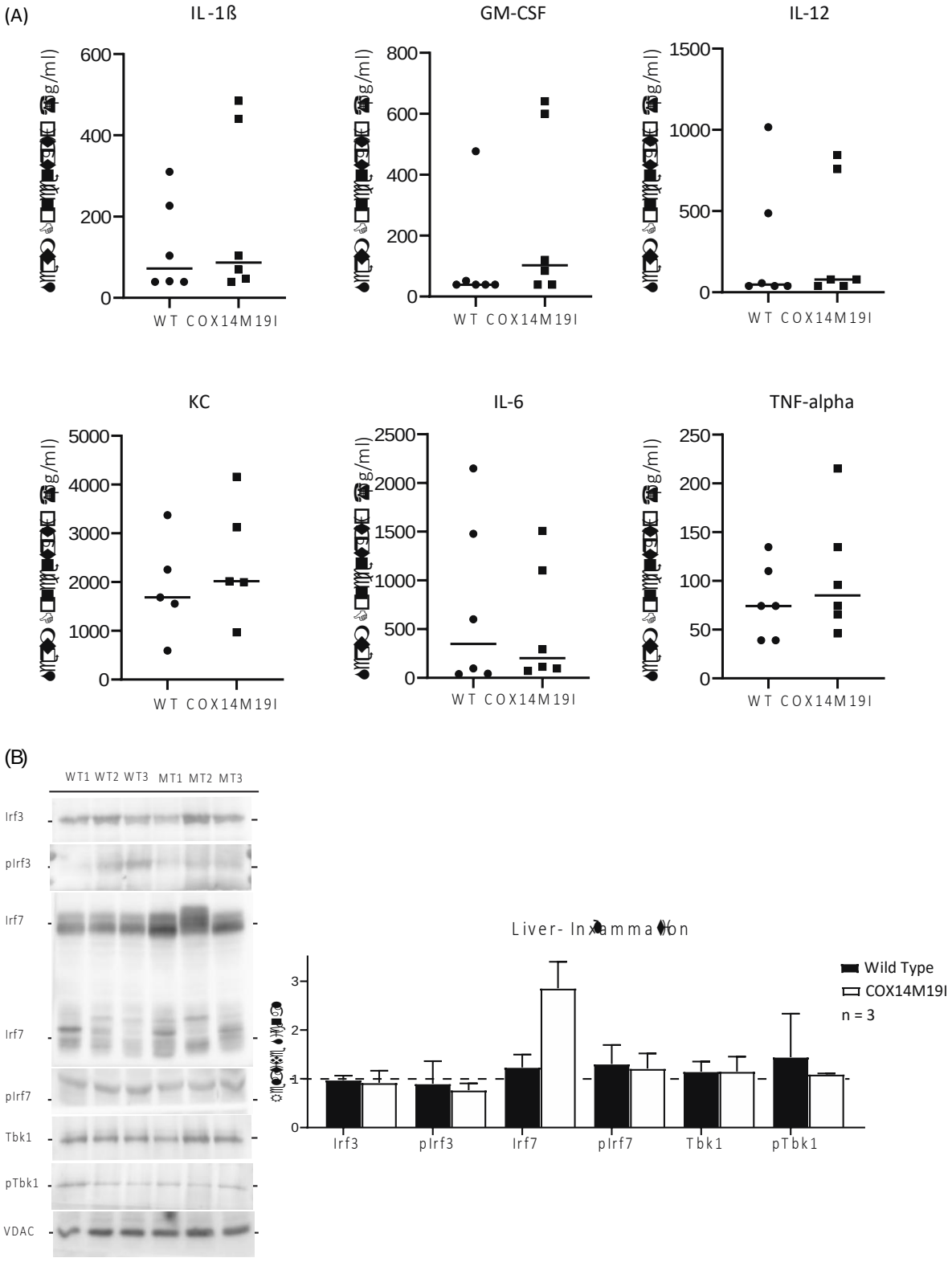

Figure A.7: Inflammatory Cytokines.

(A) Bead adsorption flow cytometry analysis was used to measure antiviral cytokine levels. **(B)** Interferon inducing factors were addressed by Immunodetection and Vdac was used for quantification. The mean ± SEM is shown (n = 3). Supplementary to Figure 3.6.

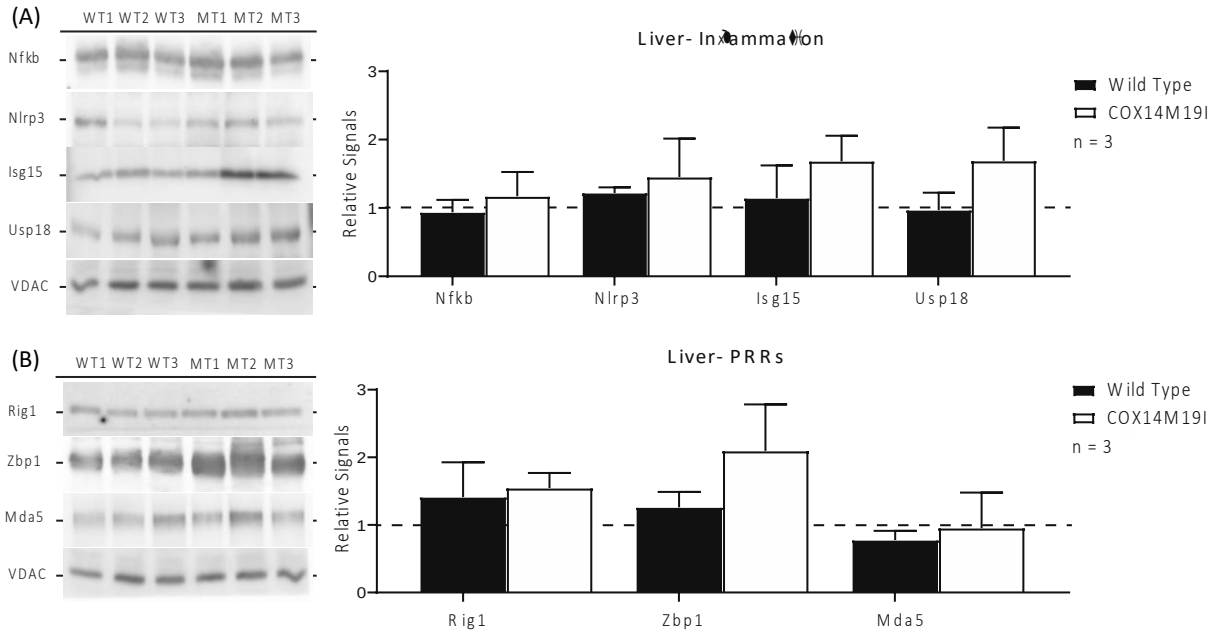

Figure A.8: Inflammatory Response in Liver.

SDS PAGE and Immunodetection was performed. Signals were normalized to VDAC. The mean ± SEM is shown (n=3). Supplementary to Figure 3.7.

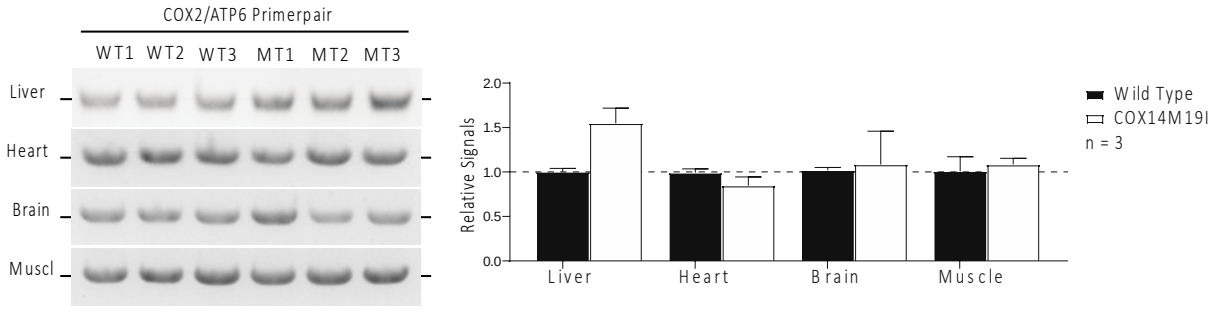

Figure A.9: Extramitochondrial mtDNA Levels.

Extramitochondrial mtDNA was amplified using PCR and measured by digital analysis. The mean ± SEM is shown (n = 3). Supplementary to Figure 3.8.

7.3 Lipid Metabolism

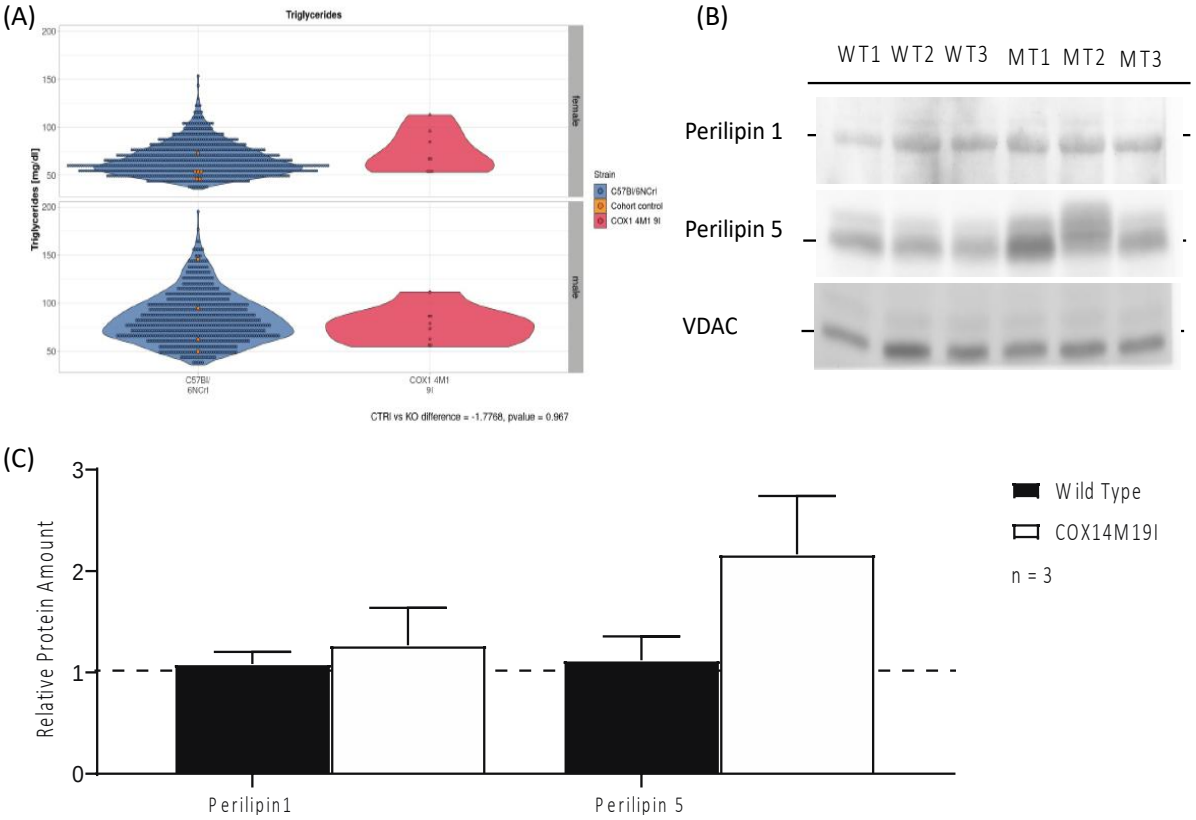

Figure A.10: Fat Metabolism.

(A) Equal Triglyceride Levels. **(B)** SDS PAGE and Immunodetection was performed and Vdac was used for quantification of Perilipin 1 and 5 Levels **(C).** The mean ± SEM is shown (n = 3). Supplementary to Figure 3.10.

7.4 Phenotype of COX14M19I

A.1.1 Immunophenotype

Table A.1: Immunophenotype

Cell Type	Cell Count
Lymphocytes	normal
B- cells	normal
Macrophages	-
T- Cells (total)	normal

CD4+ T- cells	normal
CD4+ TH- cells	normal
CD8+ T- cells	normal
Cell Type	Cell Count
Lymphocytes	normal
B- cells	normal
Macrophages	-
T- Cells (total)	normal
CD4+ T- cells	normal
CD4+ TH- cells	normal
CD8+ T- cells	normal
NKT cells	normal
CD4+ NKT cells	normal
CD4- NKT cells	normal
Effector CD4- NKT cells	-
Effector CD4+ NKT cells	-
Resting CD4- NKT cells	+
Resting CD4+ NKT cells	+
NK effector cells	normal
CD11b+ NK Cells	-
CD11b- NK Cells	+
Ly6C+ 11b- NK Cells	+
Ly6C+ 11b+ NK Cells	normal

A.1.2 Lung Phenotype

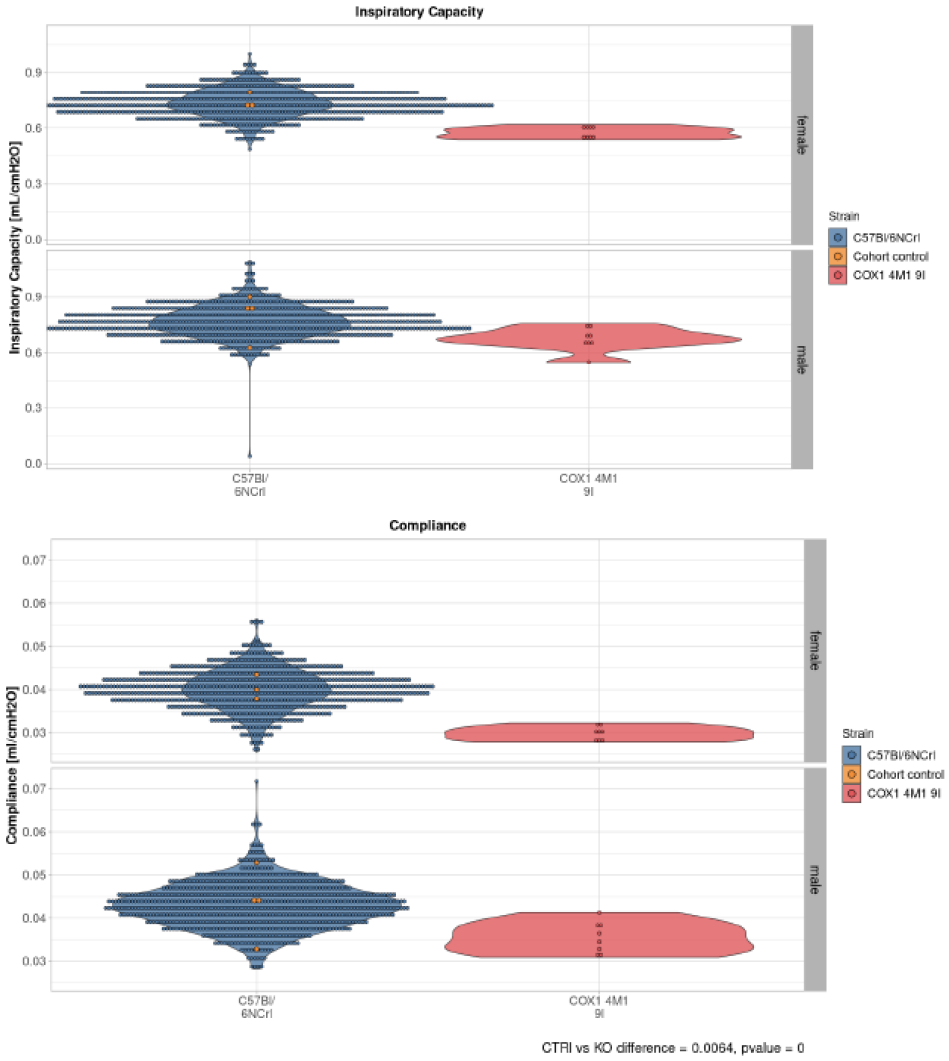

Figure A.11: Pulmonary function diagnostics showed indications of a restrictive pulmonary disease in COX14M19I.

Blood values from 16 (8 male + 8 female) COX14M19I mice were compared to a control cohort of 10 (6 male + 4 female) wild types and a historical population cohort of over 1000 animals of the C57Bl/6NCrl. Prior data courtesy: Czech Center for Phenogenomics (CCP), Prague.

8 Bibliography

An P, Wei L-L, Zhao S, Sverdlov DY, Vaid KA, Miyamoto M, Kuramitsu K, Lai M, Popov YV (2020): Hepatocyte mitochondria-derived danger signals directly activate hepatic stellate cells and drive progression of liver fibrosis. Nat Commun 11, 2362–15

Anstee QM, Reeves HL, Kotsiliti E, Govaere O, Heikenwalder M (2019): From NASH to HCC: current concepts and future challenges. Nat Rev Gastroenterol Hepatol 16, 411–428

Bahat A, MacVicar T, Langer T (2021): Metabolism and Innate Immunity Meet at the Mitochondria. Front Cell Dev Biol 9, 720490

Balaban RS, Kantor HL, Katz LA, Briggs RW (1986): Relation between work and phosphate metabolite in the in vivo paced mammalian heart. Science 232, 1121–1123

Ballmoos von C, Cook GM, Dimroth P (2008): Unique rotary ATP synthase and its biological diversity. Annu Rev Biophys 37, 43–64

Belter A, Skupinska M, Giel-Pietraszuk M, Grabarkiewicz T, Rychlewski L, Barciszewski J (2011): Squalene monooxygenase - a target for hypercholesterolemic therapy. Biol Chem 392, 1053–1075

Benador IY, Veliova M, Mahdaviani K, Petcherski A, Wikstrom JD, Assali EA, Acin-Perez R, Shum M, Oliveira MF, Cinti S, et al. (2018): Mitochondria Bound to Lipid Droplets Have Unique Bioenergetics, Composition, and Dynamics that Support Lipid Droplet Expansion. Cell Metab 27, 869–885.e6

Benard G, Faustin B, Passerieux E, Galinier A, Rocher C, Bellance N, Delage J-P, Casteilla L, Letellier T, Rossignol R (2006): Physiological diversity of mitochondrial oxidative phosphorylation. Am J Physiol Cell Physiol 291, C1172–82

Biswas S, Lunec J, Bartlett K (2012): Non-glucose metabolism in cancer cells--is it all in the fat? Cancer Metastasis Rev 31, 689–698

Bogunovic D, Byun M, Durfee LA, Abhyankar A, Sanal O, Mansouri D, Salem S, Radovanovic I, Grant AV, Adimi P, et al. (2012): Mycobacterial disease and impaired IFN-γ immunity in humans with inherited ISG15 deficiency. Science 337, 1684–1688

Boland ML, Chourasia AH, Macleod KF (2013): Mitochondrial dysfunction in cancer. Front Oncol 3, 292

Brave den F, Becker T (2020): Supercomplex formation boosts respiration. EMBO Rep 21, e51830

Chacinska A, Koehler CM, Milenkovic D, Lithgow T, Pfanner N (2009): Importing mitochondrial proteins: machineries and mechanisms. Cell 138, 628–644

Chen L, Li S, McGilvray I (2011): The ISG15/USP18 ubiquitin-like pathway (ISGylation system) in hepatitis C virus infection and resistance to interferon therapy. Int J Biochem Cell Biol 43, 1427–1431

Clemente P, Peralta S, Cruz-Bermudez A, Echevarría L, Fontanesi F, Barrientos A, Fernandez-Moreno MA, Garesse R (2013): hCOA3 stabilizes cytochrome c oxidase 1 (COX1) and promotes cytochrome c oxidase assembly in human mitochondria. J Biol Chem 288, 8321–8331

Collins LV, Hajizadeh S, Holme E, Jonsson I-M, Tarkowski A (2004): Endogenously oxidized mitochondrial DNA induces in vivo and in vitro inflammatory responses. J Leukoc Biol 75, 995–1000

Couper KN, Blount DG, Riley EM (2008): IL-10: the master regulator of immunity to infection. J Immunol 180, 5771–5777

de Duve C (2007): The origin of eukaryotes: a reappraisal. Nat Rev Genet 8, 395–403

DeBerardinis RJ, Lum JJ, Hatzivassiliou G, Thompson CB (2008): The biology of cancer: metabolic reprogramming fuels cell growth and proliferation. Cell Metab 7, 11–20

Deepa SS, Pharaoh G, Kinter M, Diaz V, Fok WC, Riddle K, Pulliam D, Hill S, Fischer KE, Soto V, et al. (2018): Lifelong reduction in complex IV induces tissue-specific metabolic effects but does not reduce lifespan or healthspan in mice. Aging Cell 17, e12769

Dennerlein S, Oeljeklaus S, Jans D, Hellwig C, Bareth B, Jakobs S, Deckers M, Warscheid B, Rehling P (2015): MITRAC7 Acts as a COX1-Specific Chaperone and Reveals a Checkpoint during Cytochrome c Oxidase Assembly. Cell Rep 12, 1644–1655

Dennerlein S, Rehling P (2015): Human mitochondrial COX1 assembly into cytochrome c oxidase at a glance. Journal of Cell Science 128, 833–837

Dhir A, Dhir S, Borowski LS, Jimenez L, Teitell M, Rötig A, Crow YJ, Rice GI, Duffy D, Tamby C, et al. (2018): Mitochondrial double-stranded RNA triggers antiviral signalling in humans. Nature 560, 238–242

Dong S, Qian L, Cheng Z, Chen C, Wang K, Hu S, Zhang X, Wu T (2021): Lactate and Myocadiac Energy Metabolism. Front Physiol 12, 715081

Dornas W, Schuppan D (2020): Mitochondrial oxidative injury: a key player in nonalcoholic fatty liver disease. Am J Physiol Gastrointest Liver Physiol 319, G400–G411

Eisner V, Picard M, Hajnóczky G (2018): Mitochondrial dynamics in adaptive and maladaptive cellular stress responses. Nat Cell Biol 20, 755–765

Elmore S (2007): Apoptosis: a review of programmed cell death. Toxicol Pathol 35, 495–516

Eskildsen S, Hartmann R, Kjeldgaard NO, Justesen J (2002): Gene structure of the murine 2„-5“-oligoadenylate synthetase family. Cell Mol Life Sci 59, 1212–1222

Farrell PJ, Broeze RJ, Lengyel P (1979): Accumulation of an mRNA and protein in interferon-treated Ehrlich ascites tumour cells. Nature 279, 523–525

Fernandez-Vizarra E, Tiranti V, Zeviani M (2009): Assembly of the oxidative phosphorylation system in humans: what we have learned by studying its defects. Biochim Biophys Acta 1793, 200–211

Fitzgerald KA, McWhirter SM, Faia KL, Rowe DC, Latz E, Golenbock DT, Coyle AJ, Liao S-M, Maniatis T (2003): IKKepsilon and TBK1 are essential components of the IRF3 signaling pathway. Nat Immunol 4, 491–496

Friedman JR, Nunnari J (2014): Mitochondrial form and function. Nature 505, 335–343

Fu B, Tian Z, Wei H (2014): Subsets of human natural killer cells and their regulatory effects. Immunology 141, 483–489

Garcia-Martinez I, Santoro N, Chen Y, Hoque R, Ouyang X, Caprio S, Shlomchik MJ, Coffman RL, Candia A, Mehal WZ (2016): Hepatocyte mitochondrial DNA drives nonalcoholic steatohepatitis by activation of TLR9. J Clin Invest 126, 859–864

Gertz EW, Wisneski JA, Stanley WC, Neese RA (1988): Myocardial substrate utilization during exercise in humans. Dual carbon-labeled carbohydrate isotope experiments. J Clin Invest 82, 2017–2025

Génin P, Morin P, Civas A (2003): Impairment of interferon-induced IRF-7 gene expression due to inhibition of ISGF3 formation by trichostatin A. J Virol 77, 7113–7119

Gill N, Chenoweth MJ, Verdu EF, Ashkar AA (2011): NK cells require type I IFN receptor for antiviral responses during genital HSV-2 infection. Cell Immunol 269, 29–37

Gray MW (1999): Evolution of organellar genomes. Curr Opin Genet Dev 9, 678–687

Greggio C, Jha P, Kulkarni SS, Lagarrigue S, Broskey NT, Boutant M, Wang X, Conde Alonso S, Ofori E, Auwerx J, et al. (2017): Enhanced Respiratory Chain Supercomplex Formation in Response to Exercise in Human Skeletal Muscle. Cell Metab 25, 301–311

Guo R, Gu J, Zong S, Wu M, Yang M (2018): Structure and mechanism of mitochondrial electron transport chain. Biomed J 41, 9–20

Gustafsson CM, Falkenberg M, Larsson N-G (2016): Maintenance and Expression of Mammalian Mitochondrial DNA. Annu Rev Biochem 85, 133–160

Hällberg BM, Larsson N-G (2014): Making proteins in the powerhouse. Cell Metab 20, 226–240

Heinonen I, Kalliokoski KK, Hannukainen JC, Duncker DJ, Nuutila P, Knuuti J (2014): Organ-specific physiological responses to acute physical exercise and long-term training in humans. Physiology (Bethesda) 29, 421–436

Hell K, Neupert W, Stuart RA (2001): Oxa1p acts as a general membrane insertion machinery for proteins encoded by mitochondrial DNA. EMBO J 20, 1281–1288

Horner R, Kluge M, Gassner J, Nösser M, Major RD, Reutzel-Selke A, Leder AK, Struecker B, Morgul MH, Pratschke J, et al. (2016): Hepatocyte Isolation After Laparoscopic Liver Resection. Tissue Eng Part C Methods 22, 839–846

Huang LS, Hong Z, Wu W, Xiong S, Zhong M, Gao X, Rehman J, Malik AB (2020): mtDNA Activates cGAS Signaling and Suppresses the YAP-Mediated Endothelial Cell Proliferation Program to Promote Inflammatory Injury. Immunity 52, 475–486.e5

Ishikawa H, Barber GN (2008): STING is an endoplasmic reticulum adaptor that facilitates innate immune signalling. Nature 455, 674–678

Jiao M, Ren F, Zhou L, Zhang L, Wen T, Wei L, Wang X, Shi H, Bai L, Zhang X, et al. (2014): Peroxisome proliferator-activated receptor α activation attenuates the inflammatory response to protect the liver from acute failure by promoting the autophagy pathway. Cell Death Dis 5, e1397–e1397

Jin J, Fu B, Mei X, Yue T, Sun R, Tian Z, Wei H (2013): CD11b(-)CD27(-) NK cells are associated with the progression of lung carcinoma. PLoS One 8, e61024

Johnson B, VanBlargan LA, Xu W, White JP, Shan C, Shi P-Y, Zhang R, Adhikari J, Gross ML, Leung DW, et al. (2018): Human IFIT3 Modulates IFIT1 RNA Binding Specificity and Protein Stability. Immunity 48, 487–499.e5

Johnson DT, Harris RA, Blair PV, Balaban RS (2007): Functional consequences of mitochondrial proteome heterogeneity. Am J Physiol Cell Physiol 292, C698–707

Karbowski M, Youle RJ (2003): Dynamics of mitochondrial morphology in healthy cells and during apoptosis. Cell Death Differ 10, 870–880

Karunadharma PP, Basisty N, Chiao YA, Dai D-F, Drake R, Levy N, Koh WJ, Emond MJ, Kruse S, Marcinek D, et al. (2015): Respiratory chain protein turnover rates in mice are highly heterogeneous but strikingly conserved across tissues, ages, and treatments. FASEB J 29, 3582–3592

Kawai T, Takahashi K, Sato S, Coban C, Kumar H, Kato H, Ishii KJ, Takeuchi O, Akira S (2005): IPS-1, an adaptor triggering RIG-I- and Mda5-mediated type I interferon induction. Nat Immunol 6, 981–988

Kemppainen J, Fujimoto T, Kalliokoski KK, Viljanen T, Nuutila P, Knuuti J (2002): Myocardial and skeletal muscle glucose uptake during exercise in humans. J Physiol 542, 403–412

Kim J, Gupta R, Blanco LP, Yang S, Shteinfer-Kuzmine A, Wang K, Zhu J, Yoon HE, Wang X, Kerkhofs M, et al. (2019): VDAC oligomers form mitochondrial pores to release mtDNA fragments and promote lupus-like disease. Science 366, 1531–1536

Larsson N-G (2010): Somatic mitochondrial DNA mutations in mammalian aging. Annu Rev Biochem 79, 683–706

Lee AJ, Ashkar AA (2018): The Dual Nature of Type I and Type II Interferons. Front Immunol 9, 2061

Lee AJ, Chen B, Chew MV, Barra NG, Shenouda MM, Nham T, van Rooijen N, Jordana M, Mossman KL, Schreiber RD, et al. (2017): Inflammatory monocytes require type I interferon receptor signaling to activate NK cells via IL-18 during a mucosal viral infection. J Exp Med 214, 1153–1167

Lee PY, Wang J-X, Parisini E, Dascher CC, Nigrovic PA (2013a): Ly6 family proteins in neutrophil biology. J Leukoc Biol 94, 585–594

Lee S-J, Zhang J, Choi AMK, Kim HP (2013b): Mitochondrial dysfunction induces formation of lipid droplets as a generalized response to stress. Oxid Med Cell Longev 2013, 327167

Li D, Wu M (2021): Pattern recognition receptors in health and diseases. Signal Transduct Target Ther 6, 291–24

Li H, Song Y, Zhang L-J, Gu Y, Li F-F, Pan S-Y, Jiang L-N, Liu F, Ye J, Li Q (2012): LSDP5 enhances triglyceride storage in hepatocytes by influencing lipolysis and fatty acid β-oxidation of lipid droplets. PLoS One 7, e36712

Li Y, D'Aurelio M, Deng J-H, Park J-S, Manfredi G, Hu P, Lu J, Bai Y (2007): An assembled complex IV maintains the stability and activity of complex I in mammalian mitochondria. J Biol Chem 282, 17557–17562

Lill R, Hoffmann B, Molik S, Pierik AJ, Rietzschel N, Stehling O, Uzarska MA, Webert H, Wilbrecht C, Mühlenhoff U (2012): The role of mitochondria in cellular iron-sulfur protein biogenesis and iron metabolism. Biochim Biophys Acta 1823, 1491–1508

Liu C, Tao Q, Sun M, Wu JZ, Yang W, Jian P, Peng J, Hu Y, Liu C, Liu P (2010): Kupffer cells are associated with apoptosis, inflammation and fibrotic effects in hepatic fibrosis in rats. Lab Invest 90, 1805–1816

Liu T, Zhang L, Joo D, Sun S-C (2017): NF-κB signaling in inflammation. Signal Transduct Target Ther 2, 1–9

Luo J, Yang H, Song B-L (2020): Mechanisms and regulation of cholesterol homeostasis. Nat Rev Mol Cell Biol 21, 225–245

Luo X, Li H, Ma L, Zhou J, Guo X, Woo S-L, Pei Y, Knight LR, Deveau M, Chen Y, et al. (2018): Expression of STING Is Increased in Liver Tissues From Patients With NAFLD and Promotes Macrophage-Mediated Hepatic Inflammation and Fibrosis in Mice. Gastroenterology 155, 1971–1984.e4

Maekawa H, Inoue T, Ouchi H, Jao T-M, Inoue R, Nishi H, Fujii R, Ishidate F, Tanaka T, Tanaka Y, et al. (2019): Mitochondrial Damage Causes Inflammation via cGAS-STING Signaling in Acute Kidney Injury. Cell Rep 29, 1261–1273.e6

Malakhov MP, Malakhova OA, Kim KI, Ritchie KJ, Zhang D-E (2002): UBP43 (USP18) specifically removes ISG15 from conjugated proteins. J Biol Chem 277, 9976–9981

Mass Sanchez PB, Krizanac M, Weiskirchen R, Asimakopoulos A (2021): Understanding the Role of Perilipin 5 in Non-Alcoholic Fatty Liver Disease and Its Role in Hepatocellular Carcinoma: A Review of Novel Insights. Int J Mol Sci 22, 5284

McArthur K, Whitehead LW, Heddleston JM, Li L, Padman BS, Oorschot V, Geoghegan ND, Chappaz S, Davidson S, San Chin H, et al. (2018): BAK/BAX macropores facilitate mitochondrial herniation and mtDNA efflux during apoptosis. Science 359, eaao6047

McWhirter SM, Fitzgerald KA, Rosains J, Rowe DC, Golenbock DT, Maniatis T (2004): IFN-regulatory factor 3-dependent gene expression is defective in Tbk1-deficient mouse embryonic fibroblasts. Proc Natl Acad Sci U S A 101, 233–238

Meurs E, Chong K, Galabru J, Thomas NS, Kerr IM, Williams BR, Hovanessian AG (1990): Molecular cloning and characterization of the human double-stranded RNA-activated protein kinase induced by interferon. Cell 62, 379–390

Meyer JN, Leung MCK, Rooney JP, Sendoel A, Hengartner MO, Kisby GE, Bess AS (2013): Mitochondria as a target of environmental toxicants. Toxicol Sci 134, 1–17

Meylan E, Curran J, Hofmann K, Moradpour D, Binder M, Bartenschlager R, Tschopp J (2005): Cardif is an adaptor protein in the RIG-I antiviral pathway and is targeted by hepatitis C virus. Nature 437, 1167–1172

Mick DU, Dennerlein S, Wiese H, Reinhold R, Pacheu-Grau D, Lorenzi I, Sasarman F, Weraarpachai W, Shoubridge EA, Warscheid B, Rehling P (2012): MITRAC links mitochondrial protein translocation to respiratory-chain assembly and translational regulation. Cell 151, 1528–1541

Miwa S, Lawless C, Zglinicki von T (2008): Mitochondrial turnover in liver is fast in vivo and is accelerated by dietary restriction: application of a simple dynamic model. Aging Cell 7, 920–923

Mohs A, Kuttkat N, Reißing J, Zimmermann HW, Sonntag R, Proudfoot A, Youssef SA, de Bruin A, Cubero FJ, Trautwein C (2017): Functional role of CCL5/RANTES for HCC progression during chronic liver disease. J Hepatol 66, 743–753

Moon J-S, Nakahira K, Chung K-P, DeNicola GM, Koo MJ, Pabón MA, Rooney KT, Yoon J-H, Ryter SW, Stout-Delgado H, Choi AMK (2016): NOX4-dependent fatty acid oxidation promotes NLRP3 inflammasome activation in macrophages. Nat Med 22, 1002–1012

Morcos MNF, Schoedel KB, Hoppe A, Behrendt R, Basak O, Clevers HC, Roers A, Gerbaulet A (2017): SCA-1 Expression Level Identifies Quiescent Hematopoietic Stem and Progenitor Cells. Stem Cell Reports 8, 1472–1478

Murphy MP, Hartley RC (2018): Mitochondria as a therapeutic target for common pathologies. Nat Rev Drug Discov 17, 865–886

Nakahira K, Hisata S, Choi AMK (2015): The Roles of Mitochondrial Damage-Associated Molecular Patterns in Diseases. Antioxid Redox Signal 23, 1329–1350

Ng MYW, Wai T, Simonsen A (2021): Quality control of the mitochondrion. Dev Cell 56, 881–905

Ng THS, Britton GJ, Hill EV, Verhagen J, Burton BR, Wraith DC (2013): Regulation of adaptive immunity; the role of interleukin-10. Front Immunol 4, 129

Ning S, Pagano JS, Barber GN (2011): IRF7: activation, regulation, modification and function. Genes Immun 12, 399–414

Niyazov DM, Kahler SG, Frye RE (2016): Primary Mitochondrial Disease and Secondary Mitochondrial Dysfunction: Importance of Distinction for Diagnosis and Treatment. Mol Syndromol 7, 122–137

Nunnari J, Suomalainen A (2012): Mitochondria: in sickness and in health. Cell 148, 1145–1159

Ong S-B, Hall AR, Hausenloy DJ (2013): Mitochondrial dynamics in cardiovascular health and disease. Antioxid Redox Signal 19, 400–414

Oshiumi H, Miyashita M, Okamoto M, Morioka Y, Okabe M, Matsumoto M, Seya T (2015): DDX60 Is Involved in RIG-I-Dependent and Independent Antiviral Responses, and Its Function Is Attenuated by Virus-Induced EGFR Activation. Cell Rep 11, 1193–1207

Ostergaard E, Weraarpachai W, Ravn K, Born AP, Jønson L, Duno M, Wibrand F, Shoubridge EA, Vissing J (2015): Mutations in COA3 cause isolated complex IV deficiency associated with neuropathy, exercise intolerance, obesity, and short stature. J Med Genet 52, 203–207

Ott M, Herrmann JM (2010): Co-translational membrane insertion of mitochondrially encoded proteins. Biochim Biophys Acta 1803, 767–775

Patrushev M, Kasymov V, Patrusheva V, Ushakova T, Gogvadze V, Gaziev A (2004): Mitochondrial permeability transition triggers the release of mtDNA fragments. Cell Mol Life Sci 61, 3100–3103

Pawlak M, Lefebvre P, Staels B (2015): Molecular mechanism of PPARα action and its impact on lipid metabolism, inflammation and fibrosis in non-alcoholic fatty liver disease. J Hepatol 62, 720–733

Pegram HJ, Andrews DM, Smyth MJ, Darcy PK, Kershaw MH (2011): Activating and inhibitory receptors of natural killer cells. Immunol Cell Biol 89, 216–224

Phillips D, Covian R, Aponte AM, Glancy B, Taylor JF, Chess D, Balaban RS (2012): Regulation of oxidative phosphorylation complex activity: effects of tissue-specific metabolic stress within an allometric series and acute changes in workload. Am J Physiol Regul Integr Comp Physiol 302, R1034–48

Platanitis E, Demiroz D, Schneller A, Fischer K, Capelle C, Hartl M, Gossenreiter T, Müller M, Novatchkova M, Decker T (2019): A molecular switch from STAT2-IRF9 to ISGF3 underlies interferon-induced gene transcription. Nat Commun 10, 2921–17

Pollak NM, Schweiger M, Jaeger D, Kolb D, Kumari M, Schreiber R, Kolleritsch S, Markolin P, Grabner GF, Heier C, et al. (2013): Cardiac-specific overexpression of perilipin 5 provokes severe cardiac steatosis via the formation of a lipolytic barrier. J Lipid Res 54, 1092–1102

Refolo G, Vescovo T, Piacentini M, Fimia GM, Ciccosanti F (2020): Mitochondrial Interactome: A Focus on Antiviral Signaling Pathways. Front Cell Dev Biol 8, 8

Richter-Dennerlein R, Oeljeklaus S, Lorenzi I, Ronsör C, Bareth B, Schendzielorz AB, Wang C, Warscheid B, Rehling P, Dennerlein S (2016): Mitochondrial Protein Synthesis Adapts to Influx of Nuclear-Encoded Protein. Cell 167, 471–483.e10

Robertson KA, Ghazal P (2016): Interferon Control of the Sterol Metabolic Network: Bidirectional Molecular Circuitry-Mediating Host Protection. Front Immunol 7, 634

Robinson BH (2000): Human cytochrome oxidase deficiency. Pediatr Res 48, 581–585

Role of Mitochondrial Nucleic Acid Sensing Pathways in Health and Patho-Physiology (2022): Role of Mitochondrial Nucleic Acid Sensing Pathways in Health and Patho-Physiology. 1–23

Schaefer AM, McFarland R, Blakely EL, He L, Whittaker RG, Taylor RW, Chinnery PF, Turnbull DM (2008): Prevalence of mitochondrial DNA disease in adults. Ann Neurol 63, 35–39

Schägger H, Pfeiffer K (2000): Supercomplexes in the respiratory chains of yeast and mammalian mitochondria. EMBO J 19, 1777–1783

Schneider WM, Chevillotte MD, Rice CM (2014): Interferon-stimulated genes: a complex web of host defenses. Annu Rev Immunol 32, 513–545

Seth RB, Sun L, Ea C-K, Chen ZJ (2005): Identification and characterization of MAVS, a mitochondrial antiviral signaling protein that activates NF-kappaB and IRF 3. Cell 122, 669–682

Sharma S, tenOever BR, Grandvaux N, Zhou G-P, Lin R, Hiscott J (2003): Triggering the interferon antiviral response through an IKK-related pathway. Science 300, 1148–1151

Shoubridge EA (2001): Cytochrome c oxidase deficiency. Am J Med Genet 106, 46–52

Soto IC, Fontanesi F, Liu J, Barrientos A (2012): Biogenesis and assembly of eukaryotic cytochrome c oxidase catalytic core. Biochim Biophys Acta 1817, 883–897

Sprenger H-G, MacVicar T, Bahat A, Fiedler KU, Hermans S, Ehrentraut D, Ried K, Milenkovic D, Bonekamp N, Larsson N-G, et al. (2021): Cellular pyrimidine imbalance triggers mitochondrial DNA-dependent innate immunity. Nat Metab 3, 636–650

Stanley WC, Lopaschuk GD, Hall JL, McCormack JG (1997): Regulation of myocardial carbohydrate metabolism under normal and ischaemic conditions. Potential for pharmacological interventions. Cardiovasc Res 33, 243–257

Stewart JB, Chinnery PF (2015): The dynamics of mitochondrial DNA heteroplasmy: implications for human health and disease. Nat Rev Genet 16, 530–542

Sun L, Wu J, Du F, Chen X, Chen ZJ (2013): Cyclic GMP-AMP synthase is a cytosolic DNA sensor that activates the type I interferon pathway. Science 339, 786–791

Swaim CD, Scott AF, Canadeo LA, Huibregtse JM (2017): Extracellular ISG15 Signals Cytokine Secretion through the LFA-1 Integrin Receptor. Mol Cell 68, 581–590.e5

Szklarczyk R, Wanschers BF, Cuypers TD, Esseling JJ, Riemersma M, van den Brand MA, Gloerich J, Lasonder E, van den Heuvel LP, Nijtmans LG, Huynen MA (2012): Iterative orthology prediction uncovers new mitochondrial proteins and identifies C12orf62 as the human ortholog of COX14, a protein involved in the assembly of cytochrome c oxidase. Genome Biol 13, R12–14

Šileikytė J, Forte M (2019): The Mitochondrial Permeability Transition in Mitochondrial Disorders. Oxid Med Cell Longev 2019, 3403075

Taanman JW (1999): The mitochondrial genome: structure, transcription, translation and replication. Biochim Biophys Acta 1410, 103–123

Takemura G, Kanamori H, Okada H, Tsujimoto A, Miyazaki N, Takada C, Hotta Y, Takatsu Y, Fujiwara T, Fujiwara H (2017): Ultrastructural aspects of vacuolar degeneration of cardiomyocytes in human endomyocardial biopsies. Cardiovasc Pathol 30, 64–71

Temperley RJ, Wydro M, Lightowlers RN, Chrzanowska-Lightowlers ZM (2010): Human mitochondrial mRNAs--like members of all families, similar but different. Biochim Biophys Acta 1797, 1081–1085

Thompson K, Mai N, Oláhová M, Scialó F, Formosa LE, Stroud DA, Garrett M, Lax NZ, Robertson FM, Jou C, et al. (2018): OXA1L mutations cause mitochondrial encephalopathy and a combined oxidative phosphorylation defect. EMBO Mol Med 10, e9060

Thomsen MK, Nandakumar R, Stadler D, Malo A, Valls RM, Wang F, Reinert LS, Dagnaes-Hansen F, Hollensen AK, Mikkelsen JG, et al. (2016): Lack of immunological DNA sensing in hepatocytes facilitates hepatitis B virus infection. Hepatology 64, 746–759

Timón-Gómez A, Nývltová E, Abriata LA, Vila AJ, Hosler J, Barrientos A (2018): Mitochondrial cytochrome c oxidase biogenesis: Recent developments. Semin Cell Dev Biol 76, 163–178

Tinari A, Giammarioli AM, Manganelli V, Ciarlo L, Malorni W (2008): Analyzing morphological and ultrastructural features in cell death. Methods Enzymol 442, 1–26

Upadhyay G (2019): Emerging Role of Lymphocyte Antigen-6 Family of Genes in Cancer and Immune Cells. Front Immunol 10, 819

Vidoni S, Harbour ME, Guerrero-Castillo S, Signes A, Ding S, Fearnley IM, Taylor RW, Tiranti V, Arnold S, Fernandez-Vizarra E, Zeviani M (2017): MR-1S Interacts with PET100 and PET117 in Module-Based Assembly of Human Cytochrome c Oxidase. Cell Rep 18, 1727–1738

Vogel F, Bornhövd C, Neupert W, Reichert AS (2006): Dynamic subcompartmentalization of the mitochondrial inner membrane. J Cell Biol 175, 237–247

Vu TH, Hirano M, DiMauro S (2002): Mitochondrial diseases. Neurol Clin 20, 809–39– vii–viii

Wang C, Richter-Dennerlein R, Pacheu-Grau D, Liu F, Zhu Y, Dennerlein S, Rehling P (2020): MITRAC15/COA1 promotes mitochondrial translation in a ND2 ribosome-nascent chain complex. EMBO Rep 21, e48833

Wang H, Sreenivasan U, Gong D-W, O'Connell KA, Dabkowski ER, Hecker PA, Ionica N, Konig M, Mahurkar A, Sun Y, et al. (2013): Cardiomyocyte-specific perilipin 5 overexpression leads to myocardial steatosis and modest cardiac dysfunction. J Lipid Res 54, 953–965

WARBURG O (1956): On the origin of cancer cells. Science 123, 309–314

Weraarpachai W, Sasarman F, Nishimura T, Antonicka H, Auré K, Rötig A, Lombès A, Shoubridge EA (2012a): Mutations in C12orf62, a factor that couples COX I synthesis with cytochrome c oxidase assembly, cause fatal neonatal lactic acidosis. Am J Hum Genet 90, 142–151

Weraarpachai W, Sasarman F, Nishimura T, Antonicka H, Auré K, Rötig A, Lombès A, Shoubridge EA (2012b): Mutations in C12orf62, a factor that couples COX I synthesis with cytochrome c oxidase assembly, cause fatal neonatal lactic acidosis. Am J Hum Genet 90, 142–151

West AP, Khoury-Hanold W, Staron M, Tal MC, Pineda CM, Lang SM, Bestwick M, Duguay BA, Raimundo N, MacDuff DA, et al. (2015): Mitochondrial DNA stress primes the antiviral innate immune response. Nature 520, 553–557

West AP, Shadel GS (2017): Mitochondrial DNA in innate immune responses and inflammatory pathology. Nat Rev Immunol 17, 363–375

Winge DR (2012): Sealing the mitochondrial respirasome. Mol Cell Biol 32, 2647–2652

Wisneski JA, Gertz EW, Neese RA, Gruenke LD, Morris DL, Craig JC (1985): Metabolic fate of extracted glucose in normal human myocardium. J Clin Invest 76, 1819–1827

Wu J, Chen ZJ (2014): Innate immune sensing and signaling of cytosolic nucleic acids. Annu Rev Immunol 32, 461–488

Yadava N, Potluri P, Scheffler IE (2008): Investigations of the potential effects of phosphorylation of the MWFE and ESSS subunits on complex I activity and assembly. Int J Biochem Cell Biol 40, 447–460

Yoon Y, Galloway CA, Jhun BS, Yu T (2011): Mitochondrial dynamics in diabetes. Antioxid Redox Signal 14, 439–457

Yu L-X, Ling Y, Wang H-Y (2018): Role of nonresolving inflammation in hepatocellular carcinoma development and progression. NPJ Precis Oncol 2, 6–10

Yu Y, Liu Y, An W, Song J, Zhang Y, Zhao X (2019): STING-mediated inflammation in Kupffer cells contributes to progression of nonalcoholic steatohepatitis. J Clin Invest 129, 546–555

Zevini A, Olagnier D, Hiscott J (2017): Crosstalk between Cytoplasmic RIG-I and STING Sensing Pathways. Trends Immunol 38, 194–205

Zhang C, Shang G, Gui X, Zhang X, Bai X-C, Chen ZJ (2019): Structural basis of STING binding with and phosphorylation by TBK1. Nature 567, 394–398

Zhang Q-F, Yin W-W, Xia Y, Yi Y-Y, He Q-F, Wang X, Ren H, Zhang D-Z (2017): Liver-infiltrating CD11b-CD27- NK subsets account for NK-cell dysfunction in patients with hepatocellular carcinoma and are associated with tumor progression. Cell Mol Immunol 14, 819–829

Zhao Y, Peng C, Lai R, Zhang J, Zhang X, Guo Z (2022): The SNPs of mitochondrial DNA displacement loop region and mitochondrial DNA copy number associated with risk of polymyositis and dermatomyositis. Sci Rep 12, 5903–7

Zhuang H, Cao G, Kou C, Liu T (2018): CCL2/CCR2 axis induces hepatocellular carcinoma invasion and epithelial-mesenchymal transition in vitro through activation of the Hedgehog pathway. Oncol Rep 39, 21–30

Zong S, Wu M, Gu J, Liu T, Guo R, Yang M (2018): Structure of the intact 14-subunit human cytochrome c oxidase. Cell Res 28, 1026–1034

Zorov DB, Juhaszova M, Sollott SJ (2014): Mitochondrial reactive oxygen species (ROS) and ROS-induced ROS release. Physiol Rev 94, 909–950

Acknowledgements

First of all, I would like to thank Prof. Peter Rehling, who is a true role model for any supervisor. His outstanding teaching of biochemistry motivated me to start this thesis in the first place. Without his enormous personal commitment and knowledge horizon, my work would not have been possible. With his humor and positive attitude, he always managed to motivate me in this challenging project. I am glad to have the opportunity to write my thesis even as a medical student in a pre-clinical field.

I would also like to thank Prof. Katschinski for taking the time to deal with me and the work in such a way.

Greatest thanks go to Dr. Hakroush and Prof. Ströbel for advice in histopathology and Stefan Jakobs helping with electron microscopy.

I have to thank Abhishek no less. No matter what time of day and no matter what topic - he always tried to help me. With an irrepressible patience he taught me all the techniques I needed and guided me through the project. Due to his great structured, systematic and accurate way of working he was a perfect teacher for me. I always enjoyed working with him, because besides all his experience he always had a good sense of fun.

Also great thanks to Arpita, who helped me as much in the implementation of the project.

Thanks to the help of Abhishek and Arpita, this project could be continued despite the Corona crisis.

Curriculum vitae

My name is Steffen Witte and I was born in Hannover on January 13, 1998, the youngest of four siblings. I started school here in 2003 at the age of five at the Wasserkamp elementary school. In 2007 I changed to the grammar school Schillerschule Hannover. I graduated from high school in 2015 at the age of 17 with a grade of 1.1 and was awarded the Karl von Frisch Prize for the best performance in biology and the Prize of the Society of German Chemists in chemistry.

I started playing soccer at the age of five and eventually transferred to Hannover 96's youth academy in 2011. Immediately after transferring, I became captain and was also called up to the Lower Saxony selection team as captain. From then on, I also regularly participated in the training camps of the youth national team. At the age of 15, I switched to VFL Wolfsburg, where I played as captain up to the U19 level. Here I played in the youth Bundesliga for the German championship as well as the youth Champions League and traveled with soccer to Qatar, England, China, Bulgaria and Russia, among other places. After a seven-month injury break, I moved back to Hannover 96, where I won the U19 DFB Cup and was called up to the professional team. After another serious injury, I started studying medicine in Göttingen. During the time of my injury, I also acquired the trainer B license.

After graduating from high school, I started a voluntary scientific year (FWJ) at the Hannover Medical School (MHH) besides soccer, where I was able to work for 16 months on research projects to develop markers for autoimmune diseases.

Since the beginning of my studies, I have been supported by a scholarship from the "Deutsche Studienstiftung".

Parallel to my studies, I coached a youth team of Göttingen 05, which I accompanied for two seasons (2017 and 2018). At the age of 21, I took over as head coach of the club's first men's team, which I coached in the Landesliga for two years. In September 2019, I completed an internship with English second-division club FC Barnsley as well as with the A-youth of FC Schalke 04.

In April 2019, I passed the first "Staatsexamen" after the fourth semester with a grade of 2.0.

In March 2020, I started my medical doctoral thesis on the topic "Fundamentals of mitochondrial diseases" in the Department of Cell Biochemistry under the supervision of Prof Dr. Rehling. Due to the Corona crisis and exams, I had to interrupt the work twice for 4

weeks each in March and July 2020. I paused clinical courses for one semester and worked for about a year and a half on the experimental part of the work. In 2022, I founded the non-profit associations Arusha FC and Sporthilfe Tansania e.V. in a charity project. For my commitment to the sustainable development of sports in Tanzania, I was awarded the Creativity Prize of the University of Göttingen, as well as the Prize for student engagement of the "Deutsche Studienstiftung". Parallel to my preparations for my second state exam beginning in June 2022, I was assistant coach of the U23 of Hannover 96, with whom we were in second place in the "Regionalliga" at the winter break. I quit the coaching job after successfully passing the exam in November 2022 due to the start of the practical year.